Numerical study of flow instability and pattern evolution induced by Marangoni convection in a shallow rectangular cavity with various boundary conditions

Jiangao ZHANG

MARCH 2022

Numerical study of flow instability and pattern evolution induced by Marangoni convection in a shallow rectangular cavity with various boundary conditions

A dissertation submitted to

THE GRADUATE SCHOOL OF ENGINEERING SCIENCE

OSAKA UNIVERSITY

in partial fulfillment of the requirements for the degree of

DOCTOR OF PHILOSOPHY IN ENGINEERING

BY

Jiangao ZHANG

MARCH 2022

ABSTRACT

Marangoni convection has attracted continuous attention due to its existence in many natural and industrial processes such as oceanography, droplets, material fabrication, and crystal growth. Numerous fruitful research findings on Marangoni convection have been reported in recent years. However, the simple boundary conditions are adopted in most previous studies, while different boundary conditions also exist in many practical problems, and the associated unclear phenomena need to be revealed as well. Therefore, this thesis focuses on the various boundary conditions occurring in the practical processes, with the aim to investigate the effect of such conditions on the flow instabilities and pattern evolutions induced by Marangoni convection in a shallow rectangular cavity. In addition, not only pure solutal Marangoni convection but also thermal-solutal Marangoni convection with such boundary conditions are further analyzed.

A theoretical model of pure Marangoni convection considering a linear solutal boundary condition is established, and solutal Marangoni convection with the moderate and high Schmidt numbers ($Sc = 10$ and 100) is studied systematically. The results reveal that the concentration fluctuations usually first appear inside the liquid layer due to the sudden change in flow direction. The evolution sequences of flow instabilities are related to the Schmidt number. Furthermore, compared with the previous studies used a constant solutal boundary condition, it is found that the computed fluid fluctuation with considerably less disturbance energy is observed and the concentration distribution is much more uniform on the bottom surface.

Numerical simulations have been carried out on the thermal-solutal Marangoni convection subjected to mutual perpendicular temperature and concentration gradients. The relative contributions of thermal and solutal Marangoni effects on flow destabilization and pattern evolution are analyzed. On the one hand, the fluctuations of temperature and concentration are observed on the free surface in the forms of hydrothermal wave and hydrosolutal wave. On the other hand, two different propagation directions of wave patterns coexist on the free surface when the overall contributions of thermal and solutal effects are in the same order. Moreover, the effect of rectangular and cylindrical configurations on the characteristics of Marangoni oscillatory flow is qualitatively examined. Last but not least, based on the previous discovery, the effect of thermal radiation on thermal-solutal Marangoni convection is investigated. The critical Marangoni number at which the flow destabilizes highly depends on thermal radiation and exhibits different variation tendencies on the stages of heat loss and gain. Such a study would be beneficial for the industrial processes such as material welding, glass production, and crystal growth, for better design and high-quality production.

CONTENTS

LIST OF FIGURES

LIST OF TABLES

CHAPTER 1

INTRODUCTION

1.1 Background

Marangoni convection usually takes place in a liquid layer due to the spatial variation of surface tension. When the surface tension variation is caused by the temperature gradient, the flow in the liquid is called thermal Marangoni convection, as shown in Figure 1.1. Analogous to the thermal Marangoni effect, when it is caused by the concentration gradient, the flow is called solutal Marangoni convection. In the presence of both temperature and concentration gradients, the combined flow is called thermal-solutal Marangoni convection.

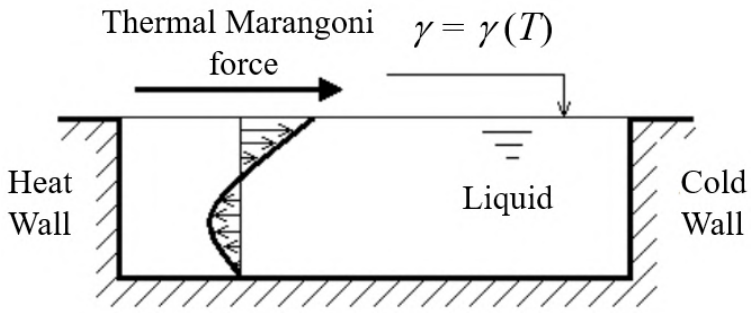

Figure 1.1 Sketch of thermal Marangoni convection.

Marangoni convection has attracted much attention for its rich dynamical behaviors and the complex flow pattern transitions. The investigations on the formation and the evolution of these complex flow patterns not only can provide insight into the occurrence mechanism of some natural phenomena including the evaporation of droplet [1] and the formation of tear of wine [2, 3], but also allow for a further understanding of the theoretical foundations in many industrial processes, such as the thin-film coating [4–6], solidification of castings and ingots [7, 8], and crystal growth [9–12]. The development of a better understanding for Marangoni convection is urgently required.

1.2 Related researches and status

Being known for over one hundred years, numerous fruitful researches on Marangoni convection have been carried out by the means of theoretical analysis, experimental observations and numerical simulations. They not only determined the critical parameters of flow pattern transition, but also analyzed the law of flow bifurcation and the influencing factors of the flow structure. Due to the improvement and progress of space experiment conditions, especially in the past forty years, the investigations on Marangoni convection have set off a new climax.

1.2.1 Study on pure thermal Marangoni convection

Numerous studies have been carried out on pure thermal Marangoni convection due to its wide existence in natural and industrial processes. In an earlier study of Smith and Davis [13], a linear stability analysis of thermal Marangoni convection in an infinitely shallow liquid layer subject to a horizontal temperature gradient was carried out. The study revealed two types of thermal convection instabilities in the liquid, namely, stationary longitudinal rolls and oblique hydrothermal wave (HTW), depending on the Prandtl number (Pr) of the working liquid and the basic flow pattern. They also determined the corresponding critical Marangoni number. In subsequent experimental studies, stationary longitudinal rolls and HTW were also observed [14–17].

Additionally, Smith [18], Davis [19], Yan *et al.* [20] and Shi *et al.* [21] provided an explanation in detail for the instability mechanism of the hydrothermal wave, as shown in Figure 1.2. As for return flow, the free surface perturbation may induce the local hot spot, and surface fluid accordingly flows from that spot toward the surroundings due to the smaller thermal Marangoni force. Meanwhile, as a result of mass conservation, the upward flow occurs beneath the hot spot, as shown in Figure 1.2(a). Since the flow velocity in the layer is smaller than that of free surface fluid, the upflow brings fluid with a lower velocity towards the surface, creating a upstream velocity perturbation opposite to the direction of basic-state surface flow, as shown in Figure 1.2(b). The upward flow shown in Figure 1.2(a) and (b) brings cooler fluid to the perturbation spot and make the temperature difference between that spot and surrounding fluid smaller, consequently, the ther-

mal Marangoni effect disappears. Owing to the inertial force, the upward flow continue to bring the lower velocity fluid to the perturbation spot, thus maximize the upstream velocity perturbation, as depicted in Figure 1.2(c). During the basic-state mode, fluid flows from the hot sidewall to cold sidewall, due to the effect of upstream velocity perturbation, the flow near the disturbance spot lags behind that of the surrounding fluid, thus the temperature of spot further decreases. Driven by the thermal Marangoni force, the fluid flows from the surroundings to the perturbation spot, and the upstream velocity perturbation is weakened. Also, the downflow beneath the cold spot appears because of the mass conservation, as shown in Figure 1.2(d). Eventually, the upstream perturbation is eliminated and the temperature of the spot attains a minimum shown in Figure 1.2(e). It is noteworthy that, with the increase of cold spot temperature, the perturbation of this spot would undergo the reverse process of Figure 1.2(a)-(e), and a new hot spot accordingly forms shown in Figure 1.2(a). The above mentioned perturbation evolution process is the instability mechanism of the hydrothermal wave, when the temperature difference on the free surface is small, a few perturbation spots maybe appear on the free surface, but the perturbation transition process cannot be sustained, and the perturbation eventually disappears; when the imposed temperature difference is large enough, the disturbance energy could maintain the dynamic equilibrium of perturbation transition, thus flow destabilizes.

Li *et al.* [22, 23] carried out three-dimensional numerical simulations of thermal Marangoni convection and Marangoni-buoyancy convection of silicon melt and 0.65 cSt silicone oil in an annular liquid pool. They indicated that indicated that the basic flow first bifurcates to the three-dimensional steady flow, and then transits to the three-dimensional oscillatory flow as the temperature difference increases. In addition, the simulation results were basically consistent with the experimental results of Azami *et al.* [24] and Schwabe [25]. Burguete *et al.* [26, 27] investigated experimentally natural and thermal Marangoni convection in a rectangular pool and found that Marangoni convection was dominant in a shallow pool, while the contribution of buoyancy was more notable in a deeper pool. Ueno *et al.* [28, 29] examined the whole transition of flow regimes from steady to turbulent, and the characteristics of the hydrothermal wave. Also, the flow structure

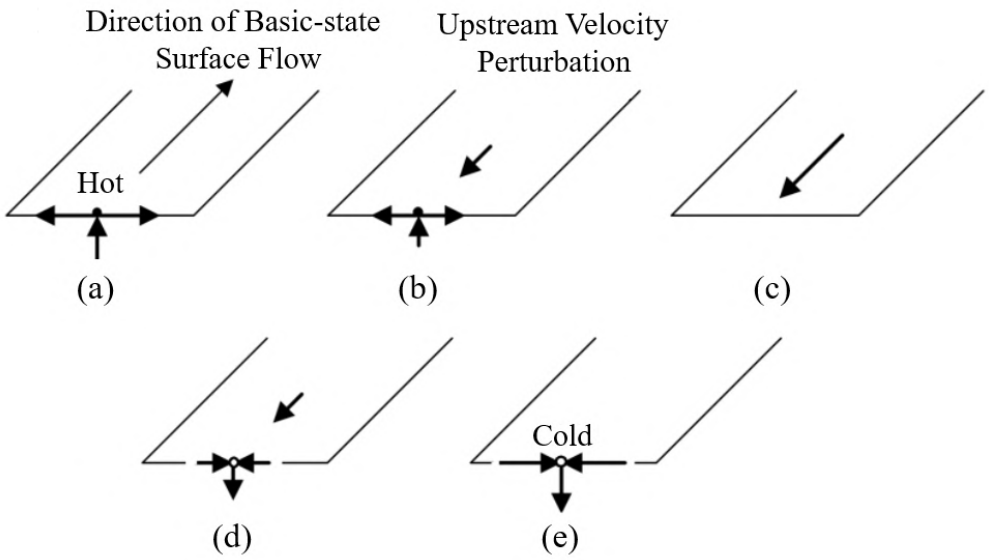

Figure 1.2 Sketch of the mechanism for hydrothermal wave.

was analyzed in detail after the flow destabilized through the observation of the suspended particle motion. Xu and Zebib [30] carried out a numerical simulation study to examine the flow characteristics and stability of thermal Marangoni convection. They pointed out the damping effect of the sidewalls on oscillations.

The fluid properties and aspect ratios of configuration have an important impact on the thermal Marangoni convection. Schwabe *et al.* [31, 32] carried out microgravity experiments and numerical simulations to investigate the flow characteristics and the stability of thermal Marangoni convection in a cylindrical annulus under various aspect ratios. It was verified that the axisymmetric flow disappears and becomes an oscillatory flow subjected to the multi-roll structure when the imposed temperature gradient exceeded a critical value. Furthermore, the aspect ratio has a significant effect on the critical Marangoni number, and the number of azimuthal waves and multicells generally increases with the increase of aspect ratio. Liu *et al.* [33] investigated the effect of aspect ratio on the instabilities of thermal Marangoni flow by using the linear stability analysis method. Their results found that the bifurcation is oscillatory in the cases of small aspect ratios, while the stationary bifurcation mode arises in the cases of large aspect ratios. Different instability mechanisms corresponding to the different bifurcation modes were also revealed. Zhang *et al.* [34]

performed the numerical simulations to investigate the critical condition of flow destabilization on thermal Marangoni flow at two different aspect ratios. It found that the flow loss stability easily at a smaller aspect ratio, and more wave number would be observed in the oscillatory flow. Liu *et al.* [35] focused on the effect of Prandtl number ($0.001 \leq Pr \leq 6.7$) on the thermal Marangoni flow in an annular pool by means of the linear stability analysis, and five types of instabilities were observed. Also, the relationships among the Prandtl number, the wave number, and the associated instability mechanism were systematically discussed. Peng *et al.* [36] observed various flow pattern transitions in a pool with different depths (1–11 mm), and three types of three-dimensional flow patterns are observed. In the shallow thin pool ($d = 1$ mm), the hydrothermal wave characterized by curved spokes is dominant. In the deep pools ($d \geq 5$ mm) the three-dimensional stationary flow appears and this flow pattern corresponds to the Rayleigh-Benard instability, which consists of pairs of counter-rotating longitudinal rolls. When 2 mm $\leq d \leq 4$ mm, the hydrothermal wave and three-dimensional oscillatory flow coexist in the pool and travel along the same azimuthal direction with the same angular velocity.

1.2.2 Study on pure soultal Marangoni convection

Most studies have focused on thermal Marangoni convection. However, as known, the solutal Marangoni convection developing in various systems, such as in solidification and casting of alloys [37] and crystal growth [38], has significant effects on these processes. To the best of our knowledge, in literature there are only a small number of studies taking the effects of solutal Marangoni convection into account. For instance, Witkowski and Walker [39] studied the primary instability of an axisymmetric steady flow driven by the solutal Marangoni effect in a liquid bridge at various Schmidt numbers ($0.5 \leq Sc \leq 20$), and found that the first transition of instability is always a Hopf bifurcation at the critical solutal Marangoni number. The corresponding comparisons for the flow structure and instability mechanism between pure thermal and pure solutal Marangoni convections were also discussed. Their results showed that the concentration distribution was different from that of the temperature field, but the instability mechanism was similar. Chen *et*

al. [40] conducted a numerical simulation of pure solutal Marangoni convection with a horizontal concentration gradient, and investigated the flow pattern transition and instability mechanism. Hydrosolutal wave (HSW), which is analogical to the hydrothermal wave, would be observed when the imposed concentration gradient was sufficiently large. And it was revealed that the corresponding instability should be attributed to the occurrence of phase lag between the concentration and the velocity fluctuations. In addition, the aspect ratio has a significant influence on the flow pattern transition.

As mentioned above, most studies considering solutal Marangoni convection adopted a constant concentration value for the boundary wall. However, in order to provide more accurate predictions through numerical simulation for applications such as painting and drying [41, 42], more appropriate boundary conditions must be used. Curak *et al.* [43] experimentally observed that the high and low concentration areas always exist in the liquid layer, and only solutal Marangoni convection has a predominant influence while the thermal Marangoni effect was neglected due to a small temperature difference in the whole system. In response to this, in order to take into account the existence of high and low concentration regions, a simplified linear boundary condition instead of a constant boundary value is needed to be applied to investigate the effect of boundary conditions on pure solutal Marangoni convection.

1.2.3 Study on thermal-solutal Marangoni convection

Thermal-solutal Marangoni flow, which is much more complex due to the coupling effects of thermal and solutal Marangoni flows, needs to be taken into consideration since it occurs in some processes such as painting [44] and crystal growth [45, 46].

Bergman [47] investigated thermal-solutal Marangoni convection in a rectangular cavity for a case where the thermal and solutal Marangoni effects were in opposite directions with equal strengths. The results verified that the flow would occur and lose its stability when the Marangoni number exceeds a specific critical value, even though the overall Marangoni effect was zero. The mechanism of flow pattern transition was however not described in detail. Arafune *et al.* [48–50]

carried out experiments and numerical simulations to analyze the relative contributions of thermal and solutal Marangoni convections in an In–Ga–Sb system. It was predicted that solutal Marangoni convection may weaken or enhance thermal Marangoni convection in the liquid, the typical surface velocity of solutal Marangoni convection was about 3–5 times higher than that of thermal Marangoni convection. Meanwhile, it was predicted that the coupling effect of thermal and solutal Marangoni convections would affect the uniformity of crystal growth. Okano *et al.* [51, 52] performed the numerical simulation on the oscillatory behavior of the melt during the melting of GaSb/InSb/GaSb alloy in the horizontal Bridgman configuration. They also pointed out that the thermal-solutal Marangoni effect should be responsible for the oscillatory flow, which may lead to growth striations and finally lower the quality of the crystal. Sheremet and Pop [53] investigated the thermal and solutal Marangoni effects on steady natural convection in a porous cavity filled with a nanofluid. They stated that the strong Marangoni effect would result in reduction of the heat transfer rate, with insignificant changes in flow patterns and heat transfer at small Marangoni numbers. Chen *et al.* [54] performed the linear stability analysis and numerical simulation to examine the flow characteristics and stability of the thermal-solutal Marangoni flow in a two dimensional rectangular cavity subjected to horizontal temperature and concentration gradients. They found that the first transition of instability was always a Hopf bifurcation, which leaded the quiescent fluid directly into the oscillatory flow. Also, the influences of Lewis number and Prandtl number on the critical Marangoni number and flow pattern transition had been investigated systematically. It was found that steady and oscillatory flow regimes can coexist simultaneously, at certain values of these parameters.

Marangoni ratio, which means the relative contributions of thermal and solutal Marangoni effects in the whole system, is also a key factor in the characteristics of thermal-solutal Marangoni convection. Zhan *et al.* [55] numerically analysed three-dimensional thermal-solutal Marangoni convection in a cubic cavity where the Marangoni ratio is varied from -2 to 1. Their results showed that the heat and mass transfer rate and the evolution of flow structures were significantly influenced by the Marangoni ratio. A symmetry-breaking pitchfork bifurcation and a transition from

the oscillatory flows to chaotic pattern were observed at the higher Marangoni ratio values, and, most interestingly, a backward transition from the chaotic state to a steady state was observed when the Marangoni ratio was equal to -0.5. Yu *et al.* [56, 57] numerically investigated thermal-solutal Marangoni convection in an annular pool where the Marangoni ratio (the ratio of solutal Marangoni effect to thermal Marangoni effect) is varied from -2 to 0.2. They pointed out that the formation mechanisms of hydrothermal wave and hydrosolutal wave are similar, and the evolution sequence of wave pattern is highly depended on the Marangoni ratio. Agampodi Mendis *et al.* [58] investigated the influence of aspect ratio on the thermal-solutal Marangoni instabilities of the liquid bridge by the means of the dynamic mode decomposition method. The spatio-temporal coherent structures were examined and the relationships among the critical Marangoni number, the wave number, and the associated aspect ratio were discussed. In addition to Marangoni ratio, Zhou *et al.* [59, 60] recently focused on the dynamic deformation of free surface in a rectangular cavity subjected to opposing thermal and solutal Marangoni effects. They found that the free surface bulges outward near the left and right sidewalls and bulges inward at the centre when the Marangoni ratio was -1. It was also predicted that the deformation of free surface increases with the increase of the thermal Marangoni number.

It must be pointed out that most of the studies mentioned above considered only the cases of mutually parallel thermal and concentration gradients in a rectangular cavity. To the best of our knowledge, the case of mutually perpendicular gradients has not been considered yet. It would be an interesting phenomenon to investigate since it occurs in some processes such as painting and drying.

1.2.4 Effect of interfacial heat transfer on Marangoni convection

Some research findings on Marangoni convection with an assumption of adiabatic free surface have been reported [61–64]. However, the interfacial heat transfer is inevitable in industrial processes and has a significant effect on the quality of final products, especially in material welding [65, 66] and crystal growth [67–69]. Therefore, many studies considering heat transfer have

emerged in the past few years.

Li *et al.* [70] studied the thermal Marangoni flow in an annular pool with/without considering thermal radiation on the free surface. They reported that the critical Marangoni number and the flow structure depended on the free surface condition, and thermal radiation needed to be taken into account for accurate predictions in crystal growth. Zhang *et al.* [34, 71] performed a series of three-dimensional numerical simulations to investigate the influence of liquid heat dissipation on the stability of thermal Marangoni convection, and analysed the associated instability mechanism. Alloui *et al.* [72] examined analytically and numerically the combined buoyancy–Marangoni convection for a power-law fluid in a shallow rectangular cavity considering heat dissipation on the free surface. Also, the effects of the thermal Rayleigh number, the Marangoni number, and the power-law index n associated with the power-law fluid on flow stability and heat transfer were discussed in detail. Jing *et al.* [73, 74] performed three-dimensional numerical simulations of thermal Marangoni flow in the $LiNbO_3$ melt in an open crucible, and radiative heat loss from the melt surface to the ambient was considered. Their results showed that a thin thermal boundary layer develops near the free surface when thermal radiation was considered. In addition, it was verified that the spoke patterns were resulting from the thermal Marangoni instability due to the reverse temperature gradient in the thin thermal boundary layer. Vinnichenko *et al.* [75] examined the effect of local radiative heating on the characteristics of horizontal convection in a rectangular tank filled with ethanol. They found that, compared with buoyancy-driven convection, the thermal Marangoni convection plays a predominant role in the thin thermal boundary layer and enhances heat transport to the whole free surface. Gelfgat *et al.* [76] investigated numerically the effect of different types of radiative heating boundary conditions on the flow instabilities of the cylindrical full-zone by the linear stability analysis method. It was shown that the radiative heat transfer greatly affected the onset of the thermal Marangoni flow, and the primary bifurcation from initially axisymmetric flows, depending simply on the total amount of heat flux provided. Kamotani *et al.* [77, 78] carried out experiments and numerical simulations to analyze the influence of ambient temperature on the thermal Marangoni instabilities of the liquid bridge. It was shown that, with

transition from heat loss to heat gain, the critical Marangoni number exhibits different variation tendencies. The three dimensional disturbance with respect to the heat loss was easier to gestate and develop compared to the case of heat gain. Jin *et al.* [79] focused on the effect of radiative heat transfer on the Marangoni flow in the liquid bridge. It was verified that thermal radiation greatly affects not only the flow structure but also the characteristics of the concentration patterns. In addition, the flow instabilities were also related to the radiative heat transfer. Yano *et al.* [80–82] examined the relative contributions of convective and radiative heat transfer under the whole interfacial heat transfer. They pointed out that thermal radiation also plays an important role in the fluid flow and temperature fields even at room temperature, while their study was focused only on a time-independent static system.

Obviously, most these studies that focused on the interfacial heat transfer considered only the case of thermal Marangoni flow. The more complex thermal-solutal Marangoni convection occurring in many practical processes has not been taken into account. Thus, it is necessary to carry out 3D numerical simulations to investigate the effect of heat transfer on thermal-solutal Marangoni convection.

1.3 Thesis outline

This thesis aims to further understand the effect of Marangoni flow considering various boundary conditions on the flow instabilities and flow pattern transitions. The chapter outlines of the present thesis are stated as follows.

In Chapter 2, the employed numerical methods including governing equations and numerical schemes for calculating the Marangoni convection in a shallow rectangular cavity are introduced. In addition, the validations of the numerical method and grid independence are conducted to confirm the calculation reliability of the present work.

In Chapter 3, a series of numerical simulations are performed to investigate the pure Marangoni convection with a linear solutal boundary condition. For the working fluid, two Schmidt number values (moderate and high) ($Sc = 10$ and 100) are chosen to examine the effect of fluid prop-

erties. In addition, the computed flow characteristics and concentration distribution are analyzed and compared with those of previous studies used a constant solutal boundary condition. This work presented herein provides a better understanding of the effect of a concentration boundary condition on Marangoni flow.

In Chapter 4, numerical simulations are carried out to study thermal-solutal Marangoni convection in a shallow rectangular cavity under the effect of mutually perpendicular thermal and concentration gradients, with the aim to shed further light on the flow bifurcation and flow pattern evolution. Also, the relative contribution of thermal and solutal Marangoni effects on the wave patterns induced by temperature and concentration fluctuations is systematically investigated. Furthermore, the effect of rectangular and cylindrical configurations on the characteristic of Marangoni oscillatory flow is qualitatively studied.

In Chapter 5, based on the study of Chapter 4, the case of interfacial heat transfer instead of an assumption of adiabatic free surface is applied, the effect of radiative heat transfer on the free surface is investigated. Wherein, the comparison among three kinds of the heat conditions, namely, heat loss, heat gain, and adiabatic case, has been conducted to obtain the distinction of flow characteristics and flow pattern transitions in the cavity. The results of present study would be beneficial for making predictions in industrial processes such as crystal growth, glass production, and welding.

In Chapter 6, the results obtained in this thesis are summarized and concluded, and perspectives for future works are described as an extension of this work.

CHAPTER 2
NUMERICAL METHODOLOGIES

In many industrial processes, Marangoni convection has a significant influence on the qualities of final products. In this chapter, the author mentions not only the pure solutal Marangoni convection but also the thermal-solutal Marangoni convection. The governing equations for calculating the Marangoni flow and relevant assumptions are introduced. All the governing equations associated with the present numerical simulation were solved using an open source software, OpenFOAM.

2.1 Pure solutal Marangoni flow

In most studies to date, the investigation on the Marangoni convection consists of three kinds of geometries; namely, sphere, cylindrical and rectangular configurations. For the sphere case, many researches focus on bubble migration, which has little relationship with the fluid mechanics. For the cylindrical case such as the crystal growth in the floating zone method, due to the requirement of microgravity condition, the large-scale experiment is hard to conduct on the earth. Thus few experimental results could be used to validate the numerical simulation. In the case of the rectangular configuration, many experiments had been conducted on the earth. And the comparison between experiment and simulation was also examined. In addition, compared with the cylindrical case, the rectangular case is suitable for a large range of practical processes such as painting and dying, crystal growth, and glass production, to cite a few. Therefore, a rectangular model would be chosen in the present study. Furthermore, in order to clarify clearly the Marangoni effect, buoyancy force is neglected in the whole system, a shallow rectangular cavity (aspect ratio, which means the ratio of length to its depth, is equal to 0.1) is adopted eventually.

When only solutal Marangoni effect is considered, the fluid motion in a three-dimensional rectangular cavity with a free surface at the top as shown in Figure 2.1 is considered in the Cartesian coordinate system. The length, width, and depth of the cavity are L, L and $0.1L$, respectively. The

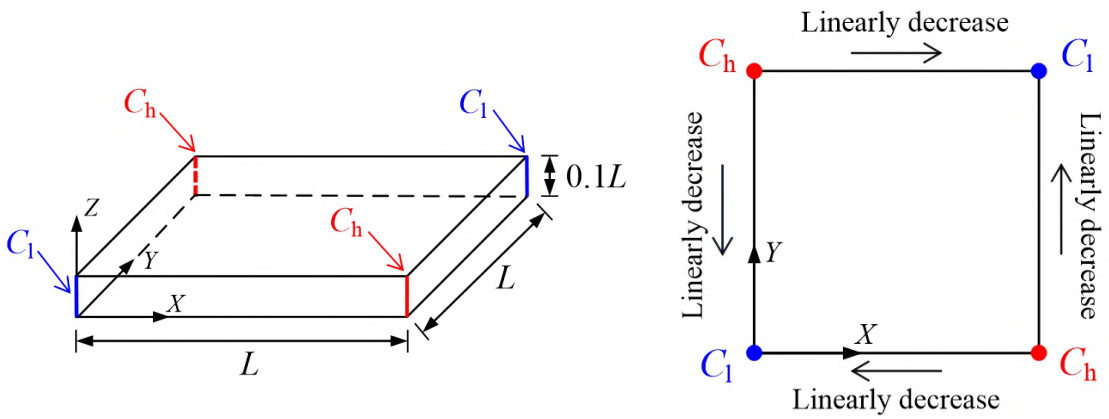

(a) bird view (b) top view

Figure 2.1 Numerical simulation domain and the prescribed boundary conditions.

fluid motion in a three-dimensional rectangular cavity with a free surface at the top as shown in Figure 2.1 is considered in the Cartesian coordinate system. The length, width, and depth of the cavity are L, L and $0.1L$, respectively. High and low concentration values, C_h and C_l are specified at the four boundary corners, and the linear solutal boundary condition is applied as shown in Fig. 1(b). The Marangoni convection along the free surface is driven by the surface tension gradient due to the imposed concentration difference.

In the simulation model we make the following assumptions: (i) the free surface does not deform under the effect of fluid flow; (ii) the fluid is incompressible and Newtonian, and the physical properties are constant except that for surface tension; (iii) the no-slip boundary condition on flow velocity is applied along boundaries except for the top free surface, and the solutal Marangoni force is taken into consideration along the free surface.

The governing equations of the fluid flow in the cavity are written in dimensionless forms. Being L as the characteristic scale for length, the coordinates (x, y, z) are defined as $(X, Y, Z)/L$. In addition, L^2/ν and ν/L are used as the characteristic time and velocity, respectively, the dimensionless governing equations are the conservation of mass, momentum, and mass transfer:

$$\nabla \cdot \boldsymbol{V} = 0 \tag{2.1}$$

$$\frac{\partial \boldsymbol{V}}{\partial \tau} + \boldsymbol{V} \cdot \nabla \boldsymbol{V} = -\nabla P + \nabla^2 \boldsymbol{V} \tag{2.2}$$

$$\frac{\partial \Phi}{\partial \tau} + \boldsymbol{V} \cdot \nabla \Phi = \frac{1}{Sc} \nabla^2 \Phi \tag{2.3}$$

where $\boldsymbol{V} = (V_x, V_y, V_z)$ is the dimensionless velocity vector, the dimensionless concentration is defined as $\Phi = (C - C_{\mathrm{l}})/(C_{\mathrm{h}} - C_{\mathrm{l}})$, τ and P are respectively the dimensionless time and pressure. $Sc = \nu/D$ is the Schmidt number, where ν is the kinematic viscosity and D is the diffusion coefficient of the fluid. In this study, the computations have been performed for the fluid with $Sc = 10$ and 100, respectively.

The boundary conditions are as follows:

$$\Phi = y \quad (x = 0) \tag{2.4}$$

$$\Phi = 1 - y \quad (x = 1) \tag{2.5}$$

$$\Phi = x \quad (y = 0) \tag{2.6}$$

$$\Phi = 1 - x \quad (y = 1) \tag{2.7}$$

$$\frac{\partial \Phi}{\partial z} = 0 \quad (z = 0) \tag{2.8}$$

and for the free surface ($z = 0.1$),

$$\frac{\partial V_x}{\partial z} = -Ma_{\mathrm{C}} \frac{\partial \Phi}{\partial x}, \quad \frac{\partial V_y}{\partial z} = -Ma_{\mathrm{C}} \frac{\partial \Phi}{\partial y}, \quad V_z = 0, \quad \frac{\partial \Phi}{\partial z} = 0 \tag{2.9}$$

Wherein, the solutal Marangoni numbers are defined as:

$$Ma_{\mathrm{C}} = \sigma_{\mathrm{C}} \frac{(C_{\mathrm{h}} - C_{\mathrm{l}})L}{\mu \nu} \tag{2.10}$$

The initial conditions are expressed as follows ($\tau = 0$):

$$V_x = V_y = V_z = 0 \tag{2.11}$$

$$\Phi = x + y \quad (x + y \leq 1) \tag{2.12}$$

$$\Phi = 1 - x - y \quad (x + y > 1) \tag{2.13}$$

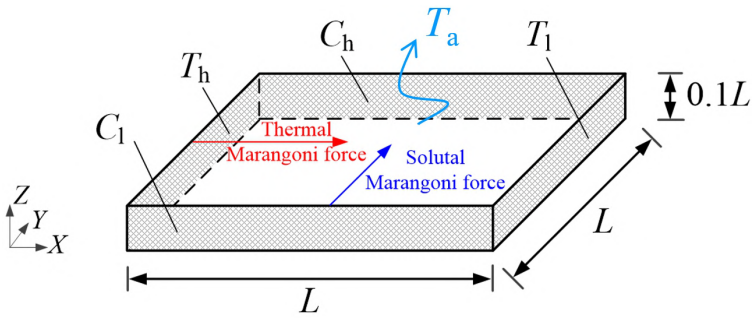

Figure 2.2 Numerical simulation domain and the prescribed boundary conditions. The red and blue arrows respectively indicate the directions of thermal and solutal Marangoni flows

2.2 Thermal-solutal Marangoni flow

When coupling effect of thermal and solutal Marangoni flows is considered, the simulation model is a rectangular cavity filled with fluid as shown in Figure 2.2. The top boundary is the free surface while the other boundaries are the cavity walls. A high and low temperature values, T_h and T_l, are set at the left ($X = 0$) and right ($X = L$) boundaries, and the concentration values of C_h and C_l are prescribed at the back ($Y = L$) and front ($Y = 0$) boundaries. Marangoni flows along the free surface are driven by the surface tension gradient due to the prescribed temperature gradient in the X-direction and the concentration gradient in the Y-direction. The directions of these flows are also shown in the figure.

Regarding the dimensionless governing equations of the fluid flow in the cavity, in addition to the conservation of mass, momentum, and mass transfer shown in the previous section, energy equation is also applied:

$$\frac{\partial \Theta}{\partial \tau} + \boldsymbol{V} \cdot \nabla \Theta = \frac{1}{Pr} \nabla^2 \Theta \tag{2.14}$$

where the dimensionless temperature and concentrations are defined as $\Theta = (T - T_l)/(T_h - T_l)$ and $\Phi = (C - C_l)/(C_h - C_l)$, τ and P are the dimensionless time and pressure. $Pr = \nu/\alpha$ is the Prandtl number, and $Sc = \nu/D$ is the Schmidt number, where α and D are the thermal diffusivity and the diffusion coefficient of working fluid ($Pr = 0.01$, $Sc = 1$), respectively.

No-slip boundary condition is applied except for top surface, and the other boundary conditions are follows:

$$\Theta = 1, \quad \frac{\partial \Phi}{\partial x} = 0 \quad (x = 0) \tag{2.15}$$

$$\Theta = 0, \quad \frac{\partial \Phi}{\partial x} = 0 \quad (x = 1) \tag{2.16}$$

$$\frac{\partial \Theta}{\partial y} = 0, \quad \Phi = 0 \quad (y = 0) \tag{2.17}$$

$$\frac{\partial \Theta}{\partial y} = 0, \quad \Phi = 1 \quad (y = 1) \tag{2.18}$$

$$\frac{\partial \Theta}{\partial y} = 0, \quad \frac{\partial \Phi}{\partial x} = 0 \quad (z = 0) \tag{2.19}$$

and on the free surface with an adiabatic assumption ($z = 0.1$):

$$\frac{\partial V_x}{\partial z} = -Ma_{\mathrm{T}} \frac{\partial \Theta}{\partial x} - Ma_{\mathrm{C}} \frac{\partial \Phi}{\partial x} \tag{2.20}$$

$$\frac{\partial V_y}{\partial z} = -Ma_{\mathrm{T}} \frac{\partial \Theta}{\partial y} - Ma_{\mathrm{C}} \frac{\partial \Phi}{\partial y} \tag{2.21}$$

$$V_z = 0 \tag{2.22}$$

$$\frac{\partial \Theta}{\partial z} = 0, \quad \frac{\partial \Phi}{\partial z} = 0 \tag{2.23}$$

When thermal radiation would be considered between the upper free surface and the ambient environment, T_{a} is the ambient temperature shown in Figure 2.2. the heat transfer through the free surface can be expressed as,

$$\frac{\partial \Theta}{\partial z} = -R_{\mathrm{ad}}(\Theta - \Theta_{\mathrm{a}}) = Q_{\mathrm{r}} \tag{2.24}$$

where Q_{r} is the heat flux on the whole free surface, $\Theta_{\mathrm{a}} = (T_{\mathrm{a}} - T_{\mathrm{l}})/(T_{\mathrm{h}} - T_{\mathrm{l}})$ is the dimensionless ambient temperature.$R_{\mathrm{ad}} = \varepsilon \sigma_{\mathrm{SB}} L(T^2 + T_{\mathrm{a}}^2)(T - T_{\mathrm{a}})/k$ is defined as the radiation number, where ε, σ_{SB} and k are respectively the emissivity, Stefan-Boltzmann constant and thermal conductivity.

The initial conditions are expressed as follows ($\tau = 0$):

$$V_x = V_y = V_z = 0 \tag{2.25}$$

$$\Theta = 1 - x \tag{2.26}$$

$$\Phi = y \tag{2.27}$$

The thermal and solutal Marangoni numbers are defined as:

$$Ma_{\mathrm{T}} = -\sigma_{\mathrm{T}}\frac{(T_{\mathrm{h}}-T_{\mathrm{l}})L}{\mu\nu} \tag{2.28}$$

$$Ma_{\mathrm{C}} = \sigma_{\mathrm{C}}\frac{(C_{\mathrm{h}}-C_{\mathrm{l}})L}{\mu\nu} \tag{2.29}$$

where $\sigma_{\mathrm{T}} = \partial\sigma/\partial T(<0)$ and $\sigma_{\mathrm{C}} = \partial\sigma/\partial C(>0)$ are the surface tension coefficients of the temperature and concentration fields, respectively.

Furthermore, the relative magnitude between the thermal and solutal Marangoni effects is described by the Marangoni ratio Ma_σ, which is defined by:

$$Ma_\sigma = \frac{Ma_{\mathrm{T}}}{Ma_{\mathrm{C}}} = -\frac{\sigma_{\mathrm{T}}(T_{\mathrm{h}}-T_{\mathrm{l}})}{\sigma_{\mathrm{C}}(C_{\mathrm{h}}-C_{\mathrm{l}})} \tag{2.30}$$

The directions of Marangoni flows are shown in Figure 2.2.

2.3 Numerical method and validation

The finite volume method is applied to discretize the associated governing equations and boundary conditions. They are solved by the pressure-implicit split-operator (PISO) algorithm [83]. The computation is carried out using the open source software OpenFOAM. The Euler scheme, QUICK scheme, and Gauss linear scheme are adopted respectively to the terms involving time derivative, divergence, and Laplacian in the governing equations. The residual of sparse matrix solvers is below the solver tolerance 1.0×10^{10} to make the simulation accurate enough. To validate the present numerical method, we conducted simulations of the thermal-solutal Marangoni convection in a cubic cavity that was investigated by Zhan *et al.* [55]. Figure 2.3 showed the the results of streamlines, temperature and concentration fields, which is consistent with the prediction of the Ref. [55] at the same computational condition. In addition, Table 2.1 shows the comparison results of average heat and mass fluxes at the left vertical wall ($x=0$) with that of Ref. [55]. The average heat and mass fluxes are given by Nusselt number Nu and Sherwood number Sh as

$$Nu = \int_0^1\int_0^1 \left|\frac{\partial\Theta}{\partial x}\right| dydz \tag{2.31}$$

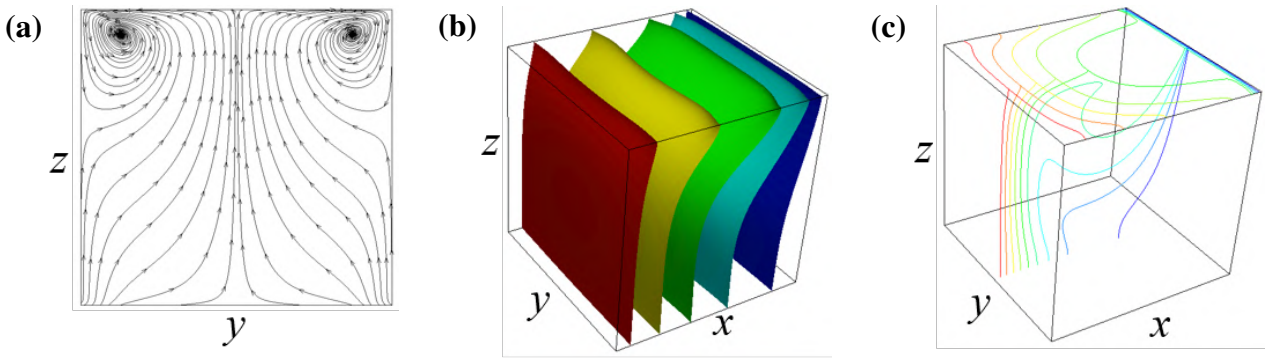

Figure 2.3 Streamlines on the mid-y-z plane (a), iso-sofurfaces of the temperature field (b) and contour slices of concentration field at the same computational condition with the Ref. [55] that $Ma_{\mathrm{T}} = 120$, $Ma_{\mathrm{C}} = -60$.

$$Sh = \int_0^1 \int_0^1 \left| \frac{\partial \Phi}{\partial x} \right| dydz \tag{2.32}$$

As shown in Table 2.1, the maximum deviation of Nu and Sh is less than 0.8%. Therefore, the present numerical method is appropriate for carrying out the intended simulations for the thermal-solutal Marangoni flow in a rectangular cavity. In addition, the calculation method used in this work was successfully adopted to investigate the thermal-solutal Marangoni convection in a liquid bridge considering with/without the radiative heat transfer on the free surface, reported in our previous work [79, 84, 85]. Therefore, we concluded that the numerical method adopted is high-accurate and appropriate for the present work.

Table 2.1 Comparison of average Nusselt number (Nu) and Sherwood number (Sh) at $Ma_{\mathrm{C}}/Ma_{\mathrm{T}} = -0.5$, $Pr = 5$ and $Sc = 50$

Ma_{T}		10	60	120	200	340
Nu	Present	1.010	1.1691	1.331	1.4976	1.7290
	Ref. [55]	1.013	1.1686	1.3306	1.4959	1.7164
Relative deviation, %		0.3	0.04	0.03	0.11	0.73
Sh	Present	1.509	2.7215	3.236	3.601	4.0764
	Ref. [55]	1.5089	2.7180	3.230	3.587	4.0665
Relative deviation, %		0.007	0.13	0.19	0.39	0.24

2.4 Grid independence validation

Figure 2.4 shows a sample computational grid. The thin boundary layers are resolved by the dense nonuniform grids near all the boundaries. Meanwhile, in order to verify the grid dependency, simulation results with four different grids are compared in the case of pure solutal Marangoni convection. Table 2.2 shows the dimensionless frequency, F, and the oscillation amplitude, A_{C}, of concentration at a sampling point, P $(x, y, z) = (0.5, 0.5, 0.1)$, on the free surface at different Schmidt number values. The maximum deviations of F and A_{C} are less than 2% between two fine grids, so the grids of $140 \times 140 \times 30$ and $160 \times 160 \times 35$ are chosen for the high-accuracy simulation in the cases of $Sc = 10$ and 100, respectively.

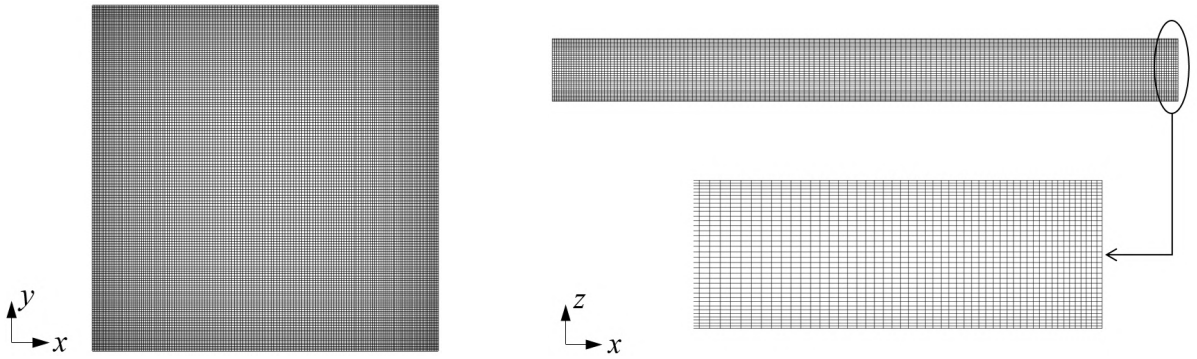

(a) top view (b) section view

Figure 2.4 A sample computational grid with a top view (a) and a section view (b) at Sc = 100.

Table 2.2 Comparison of frequency and oscillation amplitude of concentration at point P in the case of pure solutal Marangoni convection. N_x, N_y, N_z are the numbers of grids in x, y, and z directions, respectively.

Case	$N_x \times N_y \times N_z$	F	A_{C}
$Sc = 10$,	$100 \times 100 \times 30$	69.96	0.00260
$Ma = 2 \times 10^4$	$120 \times 120 \times 30$	72.39	0.00302
	$140 \times 140 \times 30$	72.59	0.00315
	$160 \times 160 \times 35$	72.96	0.00320
$Sc = 100$,	$120 \times 120 \times 35$	10.40	0.000088
$Ma = 2.5 \times 10^3$	$140 \times 140 \times 35$	10.33	0.000116
	$160 \times 160 \times 35$	10.29	0.000128
	$180 \times 180 \times 40$	10.25	0.000126

Table 2.3 Comparison of frequency and oscillation amplitude of concentration at point P in the case of an adiabatic free surface assumption on thermal-solutal Marangoni convection. N_x, N_y, N_z is the number of grids in x, y, z direction, respectively.

Case	$N_x \times N_y \times N_z$	F	A_c
Case I	$60 \times 60 \times 30$	219.845	0.0214
Case II	$80 \times 80 \times 30$	265.343	0.0137
Case III	$100 \times 100 \times 30$	263.579	0.0116
Case IV	$120 \times 120 \times 30$	262.891	0.0107
Case V	$140 \times 140 \times 40$	262.065	0.0102

In the case of an adiabatic free surface assumption on thermal-solutal Marangoni convection, simulations with five different grids are compared.Table 2.3 shows the dimensionless frequency, F, and the oscillation amplitude, A_{C}, of concentration at a sampling point P on the free surface. The maximum deviation of F and A_{C} are less than 5% between two fine grids (case IV and V), so the grid of $120 \times 120 \times 30$ is chosen for the present simulation.

Table 2.4 Comparison of frequency and oscillation amplitudes of temperature and concentration at point P in the case of thermal radiation on thermal-solutal Marangoni convection. N_x, N_y, N_z are the numbers of grids in x, y, z direction, respectively.

Case	$N_x \times N_y \times N_z$	F	A_{T}	A_{C}
Case I	$80 \times 80 \times 30$	228.0584	0.00040	0.0137
Case II	$100 \times 100 \times 30$	223.9163	0.000383	0.0020
Case III	$120 \times 120 \times 30$	223.8846	0.0003833	0.002005
Case IV	$140 \times 140 \times 35$	222.7830	0.000380	0.002003

In the case of thermal radiation on thermal-solutal Marangoni convection, simulations with four different grids are compared. Table 2.4 shows the dimensionless frequency, F, and the oscillation amplitudes, A_{T} and A_{C}, of temperature and concentration at a sampling point P on the free surface at $Ma_{\mathrm{T}} = 3 \times 10^4$ and $\Theta_a = -0.5$. The maximum deviation of F, A_{T}, and A_{C} are less than 4% between two fine grids, so the grid of $120 \times 120 \times 30$ is chosen for the present simulation.

CHAPTER 3
PURE MARANGONI CONVECTION WITH A LINEAR SOLUTAL BOUNDARY CONDITION

To the best of our knowledge, most studies considering solutal Marangoni convection adopted a constant concentration value for the boundary wall. However, in order to provide more accurate predictions through numerical simulation for applications such as painting and drying [41, 42], more appropriate boundary conditions must be used. Curak *et al.* [43] experimentally observed that the high and low concentration areas always exist in the liquid layer, and only solutal Marangoni convection has a predominant influence while the thermal Marangoni effect was neglected due to a small temperature difference in the whole system. In response to this, in this chapter a simplified linear boundary condition is applied instead of a constant boundary value, in order to take into account of the existence of high and low concentration regions. To extend the existing knowledge and gain more insight into the subject, a series of three-dimensional numerical simulations are performed on pure solutal Marangoni convection in a shallow rectangular cavity at moderate and high Schmidt number values ($Sc = 10$ and 100), with the aim of shedding further light on the related flow characteristics and flow pattern transitions in the cavity.

3.1 Basic flow pattern

When the Marangoni number is relatively small, the solutal Marangoni convection is steady, which is called the "basic flow" hereafter. Figure 3.1 shows the streamlines and the iso-concentration lines of a typical basic flow at $Sc = 10$. It can be noted that the streamlines along the boundaries are totally symmetric along the diagonals due to the applied linear boundary condition. The fluid in the cavity near the free surface flows from the high concentration region (A) to the low concentration region (C) with a certain curvature, and then returns back near the bottom due to mass balance, as shown in the simulation domain in Figure 3.1(a). The Schmidt numbers ($Sc = 10$ and 100) used for the working fluid in the present study are much larger than unity. It means that the relative

contribution of the advective mechanism is more dominant than that of diffusion. Thus, the mass transfer in the cavity is basically by fluid flow and is very sensitive to the flow region. This leads to the drastically distorted iso-concentration lines on the free surface, as shown in Figure 3.1(b).

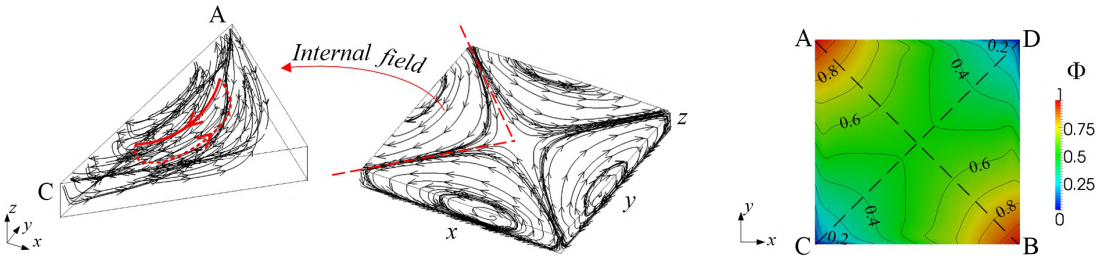

(a) streamlines of internal field (left) and boundaries (right) (b) iso-concentration lines

Figure 3.1 Typical snapshots of the streamlines (a) and concentration field (b) of the basic flow at $Sc = 10$. The contour value of concentration is from 0.1 to 0.9 with steps of 0.1.

Figure 3.2 presents the computed streamlines and iso-concentration lines in detail along the A-B and C-D planes at different Schmidt number and solutal Marangoni number values. The positions of the A-B and C-D planes are shown in Figure 3.1(b). Because of the lower mass diffusivity of the case, the concentration boundary layer appears near the corners at $Sc = 100$, which is in good agreement with those obtained by Chen *et al.* [40], while it is not obvious at $Sc = 10$. For a moderate Schmidt number, as the Marangoni number increases, i.e., at $Ma_{\mathrm{C}} = 5 \times 10^3$, two small secondary vortices appear near points A and B as shown in Figure 3.2(b), resulting from the enhancement of the solutal Marangoni effect. In the case of high Schmidt number ($Sc = 100$), it is evident from Figure 3.2(c) and Figure 3.2(d) that all vortices are much closer to the free surface, and more secondary vortices develop at the A–B plane at the same Ma_{C} level. A similar phenomenon of secondary vortices was also observed in previous studies in the case of pure thermal Marangoni convection [35, 86]. These small vortices are embedding into the basic flow and would appreciably affect the concentration field, as depicted in the concentration distribution of Figure 3.2.

The variations of the magnitude of flow velocity and the concentration along the diagonals AB and CD on the free surface are plotted in Figure 3.3. The diagonals AB and CD are presented

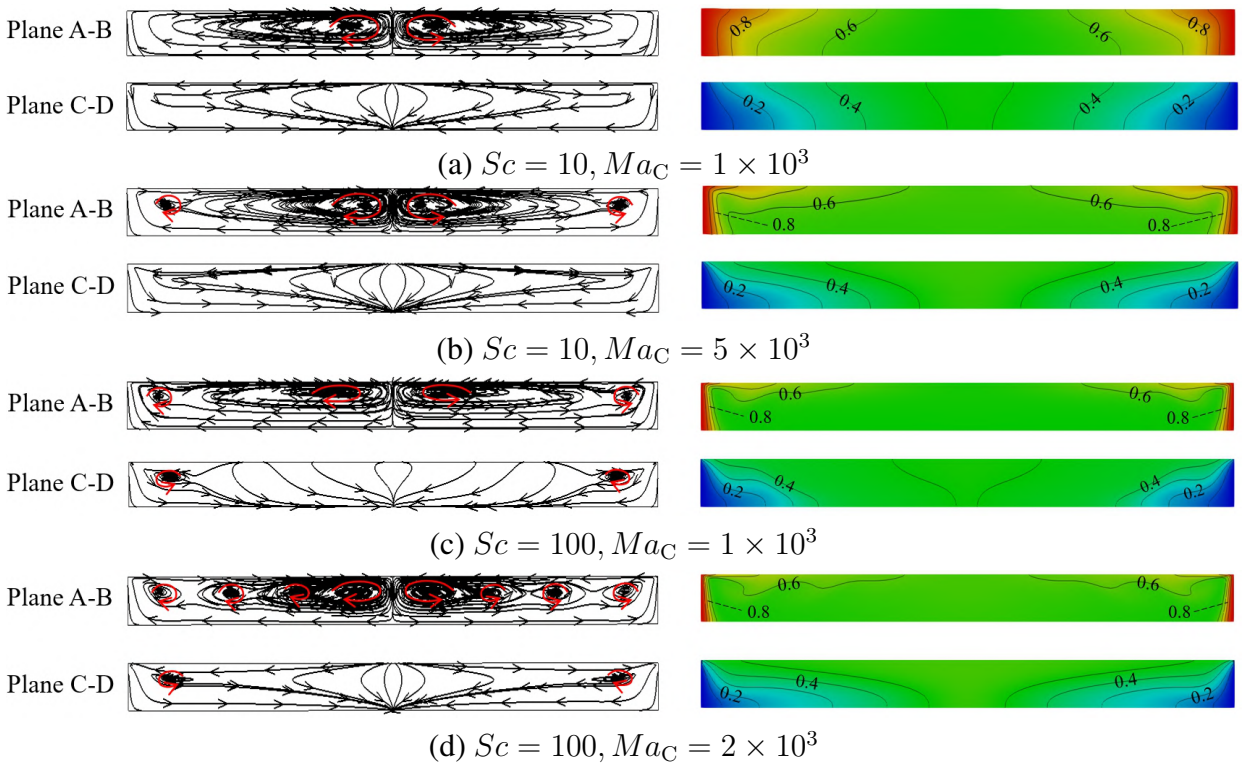

Figure 3.2 Streamlines (left) and iso-concentration lines (right) of basic flow at the A–B and C–D planes. (a) $Sc = 10, Ma_C = 1 \times 10^3$; (b) $Sc = 10, Ma_C = 5 \times 10^3$; (c) $Sc = 100, Ma_C = 1 \times 10^3$ and (d) $Sc = 100, Ma_C = 2 \times 10^3$. The position of the A–B and C–D planes are shown in Figure 3.1(b), and the contour value of concentration is from 0.1 to 0.9 with steps of 0.1.

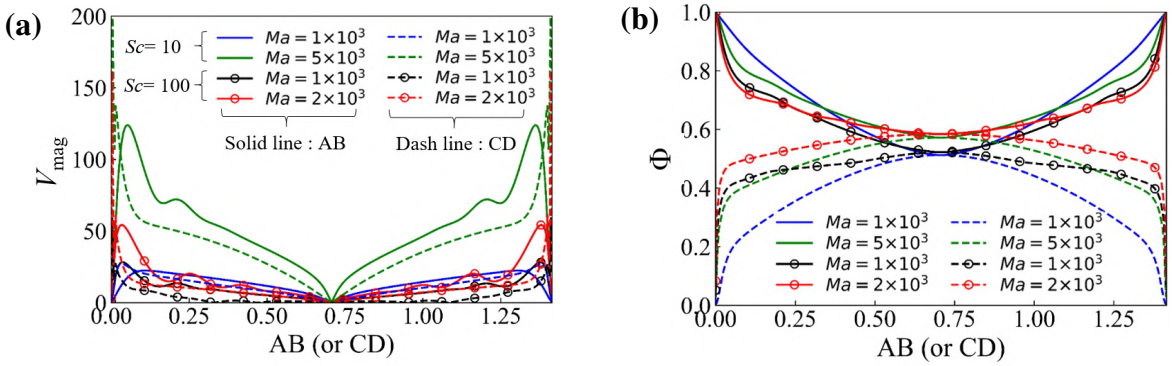

Figure 3.3 Distributions of magnitude of velocity V_{mag} (a) and concentration Φ (b) along the diagonals AB and CD at different Schmidt number and solutal Marangoni number values. The positions of the diagonals AB and CD are shown in Figure 3.1(b).

with the solid and dash lines, respectively. The peaks of the curves in Figure 3.3(a) coincide with their respective vortice-center positions. Large concentration drops appear in the vicinity of the boundary corners so that the effect of solutal Marangoni convection in the mid-section of the free surface is weaker than that at the corners, which agrees well with the result of Figure 3.1(b). Also, as the solutal Marangoni number becomes larger, the concentration drops increase, and the solutal Marangoni effect is enhanced, leading to a stronger fluid flow, as seen in Figure 3.3(b).

3.2 Critical Marangoni number

Once the solutal Marangoni number exceeds a critical value, namely, critical Marangoni number $Ma_{\mathrm{C,cri}}$, the basic flow becomes unsteady and bifurcates into three-dimensional oscillatory flows. The $Ma_{\mathrm{C,cri}}$ value were obtained as 11153 and 2104 in the cases of $Sc = 10$ and 100 by the global linear stability analysis method, which has shown high accuracy in our previous studies [87]. At the high Schmidt number value, as mentioned earlier, larger solutal Marangoni effect is observed near the boundary corners at the same Ma_{C} number level (see Figure 3.3), which makes the three-dimensional disturbance gestate and develop easily. Thus, the $Ma_{\mathrm{C,cri}}$ value with respect to $Sc = 10$ is approximately 5.3 times larger than that of $Sc = 100$. Imaishi *et al.* [88] reported that for the pure thermal Marangoni flow in an annular pool, as the Prandtl number (Pr) increases from 10 to 100, $Ma_{\mathrm{C,cri}}$ becomes about 5.7 times lower, which is close to the present result.

3.3 Comparison with CBC (constant boundary condition) in oscillatory flow

3.3.1 Characteristics of Marangoni oscillatory flow

In most studies to date [89–92], the simple CBC (constant boundary condition) subjected to horizontal gradients is applied. However, as mentioned earlier the boundary condition used will have an important influence on the characteristics of oscillatory flow. Figure 3.4 presents the variation of concentration at the sampling points (P) at $(x, y, z) = (0.5, 0.5, 0.1)$ and (M) at $(x, y, z) = (0.2, 0.2, 0.1)$ with time for $Sc = 10$ at the CBC and LBC (linear boundary condition). The setups of CBC and LBC are shown in Figure 3.4.

It is noteworthy that the flow in the case of LBC, undergoes a backward transition from an oscillatory mode to a chaotic one at $Ma_{\mathrm{C}} \approx 3 \times 10^4$, then to the oscillatory pattern again, while the concentration oscillation associated with the CBC just becomes more complicated with the increase of Ma_{C}. As shown in Figure 3.4, the concentration Φ at two sampling points is quasi-periodic at $Ma_{\mathrm{C}} = 3.25 \times 10^4$, but the flow velocity fluctuates irregularly in time at $Ma_{\mathrm{C}} = 3 \times 10^4$. This phenomenon of backward transition at the LBC could be illustrated by the dynamic theory. Although, with the increase of the solutal Marangoni number, the temporal complexity of the flow reduces from chaotic to quasi-oscillatory, the spatial flow pattern changes from four to eight vortices, as seen in Figure 3.5. Eventually, the overall complexity of the flow increases, the appearance of the backward transition from chaotic to oscillatory is reasonable. Similar backward transitions from the oscillatory to steady state [45], or from chaotic to an oscillatory flow [55, 93] have been observed in an annular pool and in a rectangular cavity. However, all the cases mentioned here are due to the coupling effect of thermal and solutal Marangoni flows; by suppressing or enhancing each other.

Most interestingly, it was found from Figure 3.4 that, even though the flow instability (oscillatory or chaotic) modes might be different at the same Ma_{C} level, the disturbance energy concerning the CBC is much stronger and the concentration fluctuation is always larger than that of the case of LBC. Also, the oscillation amplitude at the mid-center point P is close to 0 due to the mutually suppressing effects of the symmetrical solutal Marangoni flows in the case of LBC.

3.3.2 Concentration distribution

The control of mass transfer is crucial for the quality of products in applications especially in dying and painting. Thus, the concentration field and its stability are further investigated. Figure 3.6 shows the computed distribution of the time-averaged concentration Φ_{Mean} on the bottom surface for two different boundary conditions. As seen in Figure 3.6(d)– Figure 3.6(f), the concentration fields in the domain are nonuniform everywhere and fluctuate sharply in a wavy form due to the development of oblique traveling waves, as pointed in our previous work [93]. Nevertheless,

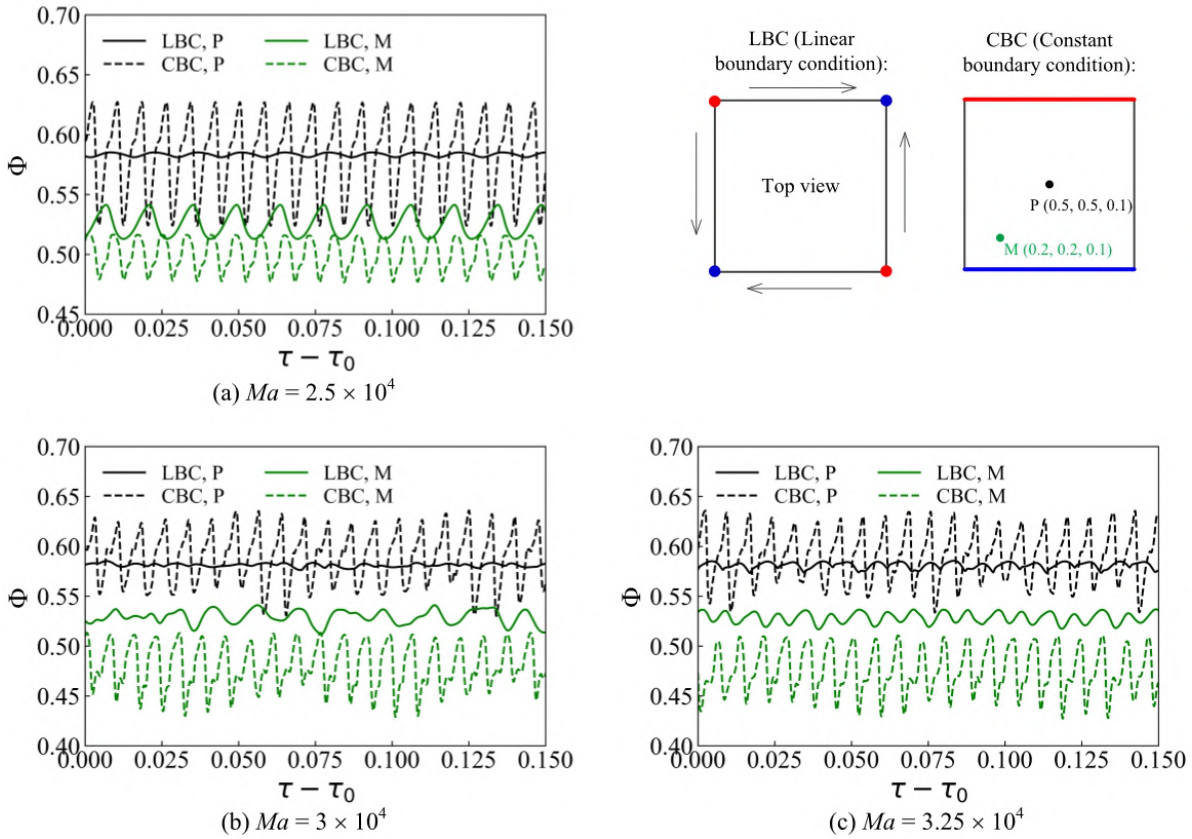

(a) $Ma = 2.5 \times 10^4$

(b) $Ma = 3 \times 10^4$

(c) $Ma = 3.25 \times 10^4$

Figure 3.4 Variation of concentration Φ at the sampling points P and M with time at $Sc = 10$ for two different boundary conditions. (a) $Ma_{\mathrm{C}} = 2.5 \times 10^4$, (b) $Ma_{\mathrm{C}} = 3 \times 10^4$, (c) $Ma_{\mathrm{C}} = 3.25 \times 10^4$. The dimensionless time τ_0 represents an instant. In addition, the setups of LBC and CBC are shown and the red and blue colours represent the high and low concentration, respectively.

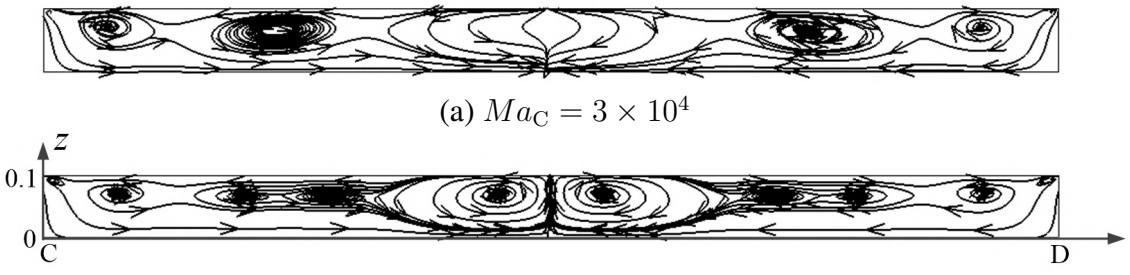

(a) $Ma_{\mathrm{C}} = 3 \times 10^4$

(b) $Ma_{\mathrm{C}} = 3.25 \times 10^4$

Figure 3.5 Streamlines of LBC at the C–D planes at (a) $Ma_{\mathrm{C}} = 3 \times 10^4$ and (b) $Ma_{\mathrm{C}} = 3.25 \times 10^4$. The position of the C–D plane is shown in Figure 3.1(b).

the stability of the concentration field is easier to sustain in the case of LBC, and the concentration contours are more uniform in most areas of the bottom surface as seen in Figure 3.6(a)– Figure 3.6(c). In addition, the concentration distribution in both cases, respectively, gave rise to just a few differences for such a large range of Ma_{C} values.

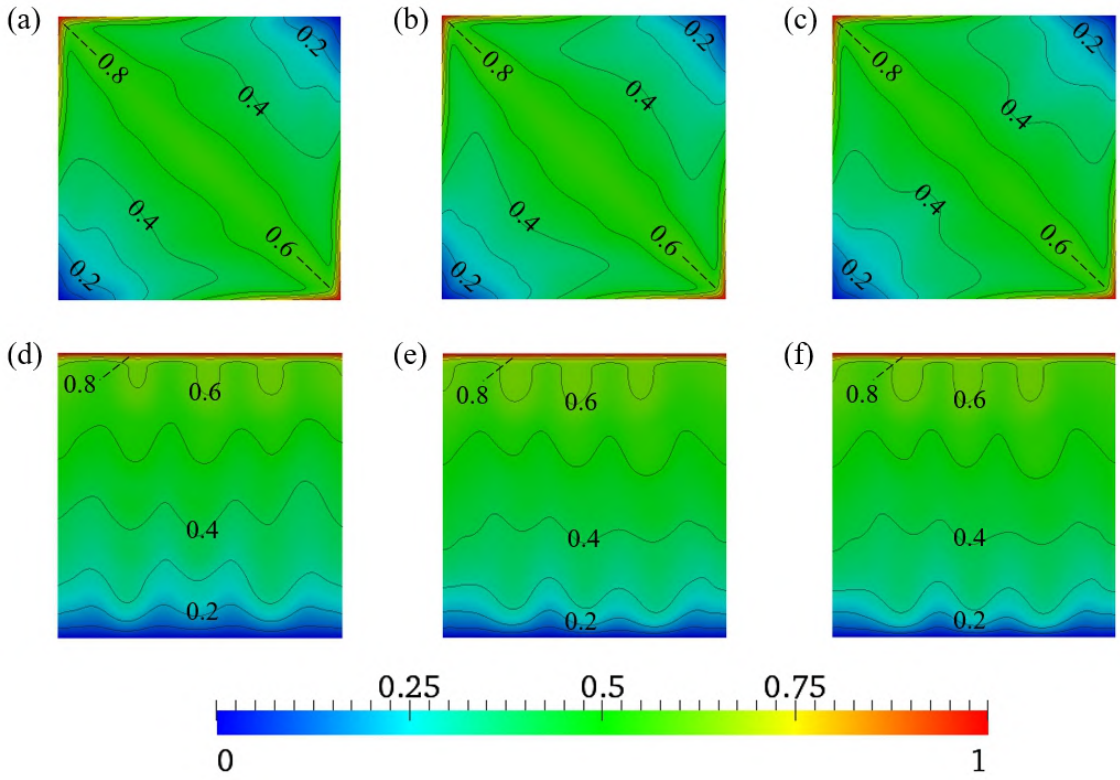

Figure 3.6 Distributions of the time-averaged concentration Φ_{Mean} on the bottom surface in the cases of LBC (a-c) and CBC (d-f) at $Ma_{\mathrm{C}} = 2.5 \times 10^4$ (a, d), $Ma_{\mathrm{C}} = 3 \times 10^4$ (b, e) and $Ma_{\mathrm{C}} = 3.25 \times 10^4$ (c, f). The contour value of concentration is from 0.1 to 0.9 with steps of 0.1.

The boundary conditions affect not only the characteristics of oscillatory flow and concentration stability but also the wave pattern evolution. As pointed out in previous studies [15, 93, 94], there are generally only two kinds of wave patterns, namely standing and oblique traveling waves for CBC, while more diverse and complicated flow patterns develop for LBC, which will be introduced in more detail in the following sections.

3.4 Wave pattern evolution in LBC

3.4.1 For moderate Schmidt number ($Sc = 10$)

In order to quantitatively investigate three-dimensional disturbances of concentration, a fluctuation quantity ($\delta\Phi$) for one period is introduced as,

$$\delta\Phi(x, y, z, \tau) = \Phi(x, y, z, \tau) - \frac{1}{\tau_p}\int_{\tau_0}^{\tau_0+\tau_p} \Phi(x, y, z, \tau)d\tau \tag{3.1}$$

Figure 3.7 shows the computed snapshots of the concentration fluctuations on the free surface and the corresponding space-time diagram (STD), which consists of a series of parallel stripes, at four different Marangoni number values; namely, Ma_{C} = (1.2, 1.5, 2 and 2.5) $\times 10^4$. It is evident that the traveling wave instabilities are observed on the free surface, and the maximum concentration fluctuation is proportional to the solutal Marangoni number value.

At $Ma_{\mathrm{C}} = 1.2 \times 10^4$, the flow destabilizes and bifurcates to an oscillatory flow, and a symmetrical wave 1 (SW1) appears, which is characteristically symmetrical along the diagonals AB and CD, as shown in Figure 3.7(a). The SW1 propagates from low concentration areas (points C, D) to the center region of the free surface, corresponding to the tilted straight stripes on the STD. It should be pointed out that, the flow instability is mainly caused by the sudden change in the flow direction near the low concentration areas when it comes close to the corners. Therefore, when Ma_{C} slightly exceeds the $Ma_{\mathrm{C,cri}}$ value, the maximum concentration fluctuation will not appear on the free surface. It exists in the liquid layer close to the low concentration areas, as shown in Figure 3.8(a). In addition, with the motion of the return flow near the bottom, the fluctuation propagates from the corner to the center region of the domain, which is synchronously accompanied by the attenuation of concentration fluctuations during the propagation process. Hence, the concentration fluctuation near the diagonal AB is approximately 0, as shown in the STD from Figure 3.7(a).

At $Ma_{\mathrm{C}} = (1.5 \text{ and } 2) \times 10^4$, the solutal Marangoni effect becomes strengthened, as shown in Figure 3.7(b) and Figure 3.7(c). As the flow disturbance gets stronger, the concentration fluc-

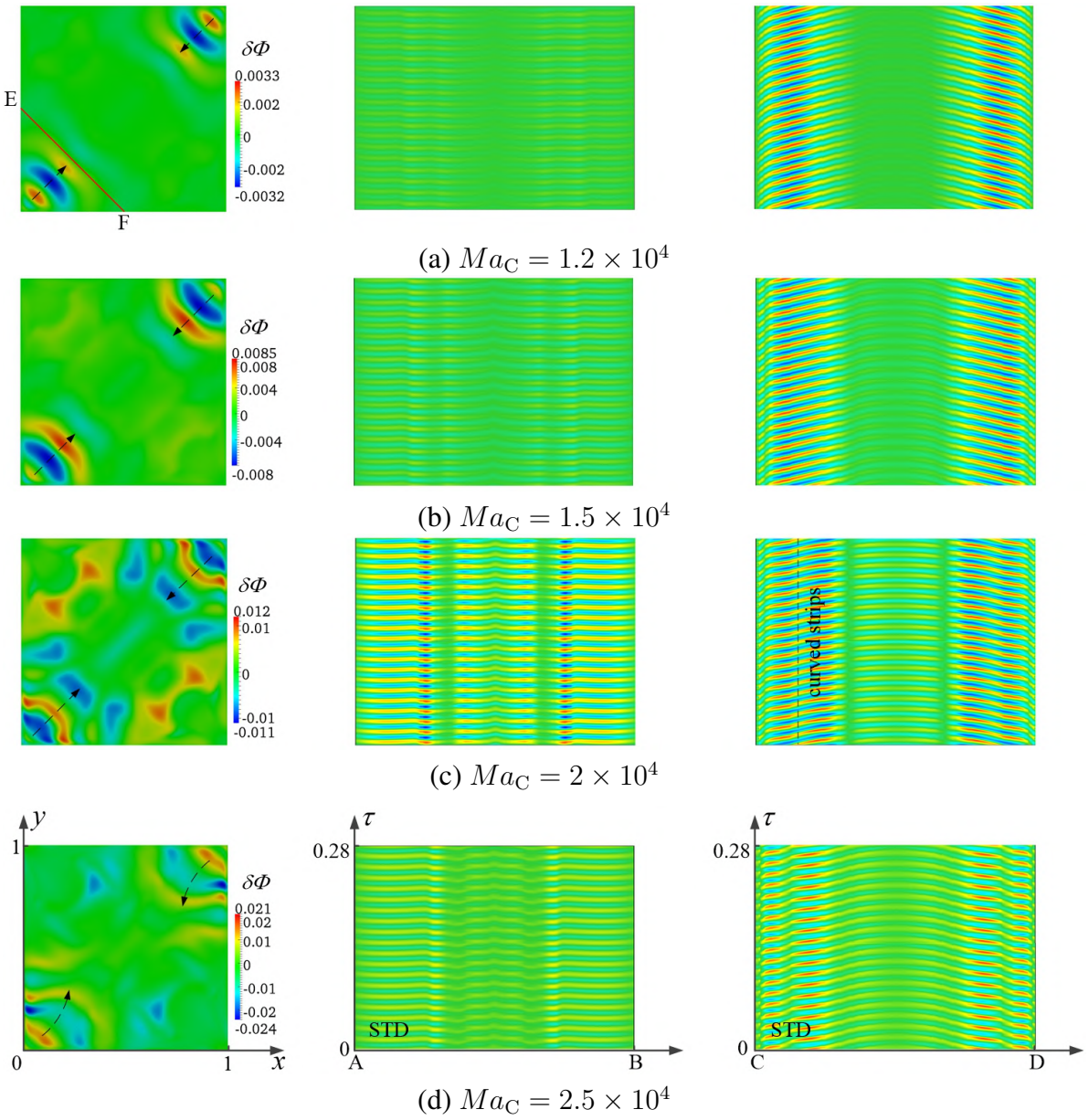

Figure 3.7 Snapshots of surface concentration fluctuations and the corresponding space-time diagram (STD) along the diagonals AB and CD at $Sc = 10$. (a) $Ma_C = 1.2 \times 10^4$, (b) $Ma_C = 1.5 \times 10^4$, (c) $Ma_C = 2 \times 10^4$ and (d) $Ma_C = 2.5 \times 10^4$. The arrows in concentration fluctuations indicate the directions of wave propagation. In addition, the dimensionless time τ for all STDs is 0.28, and the positions of the diagonals AB and CD are shown in Figure 3.1(b).

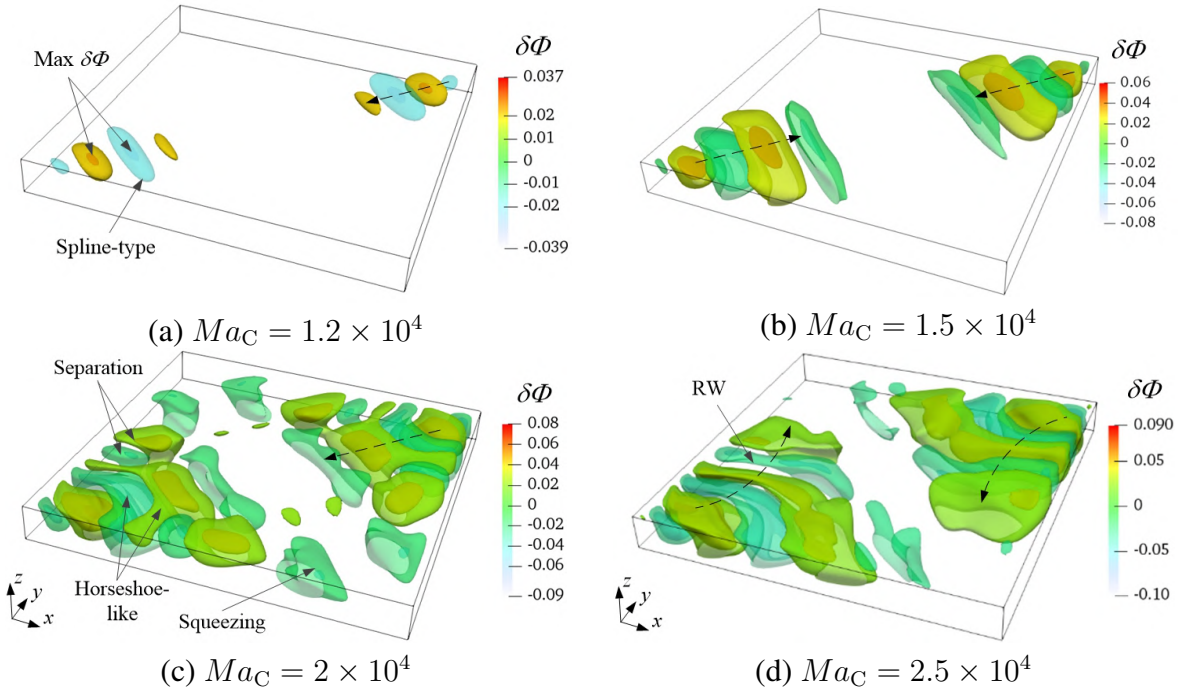

Figure 3.8 Isosurfaces of 3D concentration fluctuations in the whole domain at $Sc = 10$. (a) $Ma_C = 1.2 \times 10^4$, (b) $Ma_C = 1.5 \times 10^4$, (c) $Ma_C = 2 \times 10^4$ and (d) $Ma_C = 2.5 \times 10^4$.

tuations gradually become closer to the center region and cover the whole free surface with the increase of the solutal Marangoni number, as can be clearly observed from the stripes on the STD at lines AB and CD. In addition, due to the effect of cavity walls (the flow is confined within the cavity), the development of flow patterns cannot sufficiently progress, thus the wave patterns undergo a series of evolutions such as expansion, separation, squeezing, and merging during propagation, as shown in Figure 3.8(c). Therefore, the wave patterns transform from spline-like shapes (see Figure 3.8(a)) to horseshoe-like configurations. The locally curved stripes also appear on the STD due to squeezing and merging of wave patterns in the liquid layer, as shown in Figure 3.7(c).

At $Ma_C = 2.5 \times 10^4$, three-dimensional disturbance further increases, the wave patterns change from SW1 to RW (rotation wave) forms, propagating in the counter-clockwise direction, as shown in Figure 3.7(d) and Figure 3.8(d). The streamlines at the E–F plane are depicted in Figure 3.9. The position of the E–F plane is shown in Figure 3.7(a). As indicated in Figure 3.9(b), a secondary instability occurs at $Ma_C = 2.5 \times 10^4$. The symmetry of streamlines is broken, resulting in the

generation of RW. This secondary instability should be attributed to the occurrence of pitchfork bifurcation, in which the direction of propagation is random, as pointed out previously [55]. The RW, propagating in the clockwise direction, is also observed at $Ma_{\mathrm{C}} = 2.4 \times 10^4$. A similar flow instability with respect to the pure thermal Marangoni flow has been reported by Li *et al.* [70] in a thin annular pool, and they called this type of oscillation the "travelling hydrothermal wave".

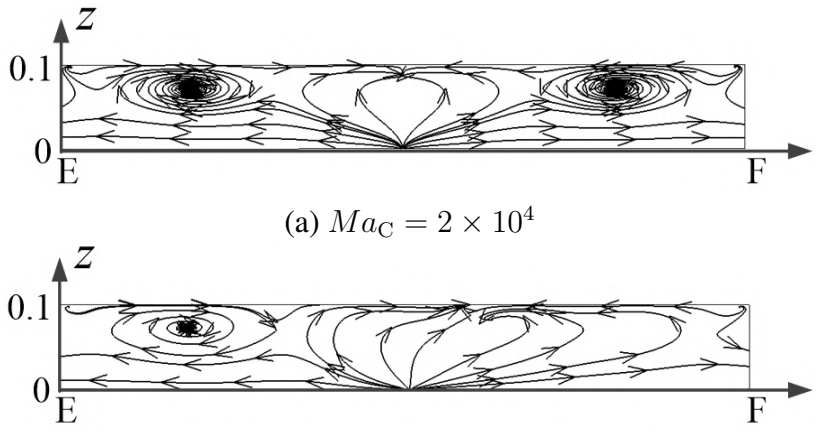

(a) $Ma_{\mathrm{C}} = 2 \times 10^4$

(b) $Ma_{\mathrm{C}} = 2.5 \times 10^4$

Figure 3.9 Streamlines at the E–F plane at (a) $Ma_{\mathrm{C}} = 2 \times 10^4$ and (b) $Ma_{\mathrm{C}} = 2.5 \times 10^4$. The position of the E–F plane is shown in Figure 3.7(a).

At the higher solutal Marangoni number values, the associated flow exhibits another type of symmetrical wave 2 (SW2), which only remains symmetrical along the diagonal AB. Figure 3.10 presents the concentration fluctuation and the associated STD at $Ma_{\mathrm{C}} = (3.25 \text{ and } 4) \times 10^4$. This instability of SW2 is caused by the separation of flow disturbances near the wave sources, as shown in the Figure 3.11. In the liquid layer, the wave oscillations would not propagate further along the line CD but spread directly at a certain curvature from the wave source locations (points C, D) to the wave sinks (points A, B). A similar phenomenon has been observed by Yu *et al.* [57] and Zhang *et al.* [95] in an annular pool in the case of thermal-solutal Marangoni flow, while the positions of wave sources and sinks were random. It could also be found that the regularity of surface fluctuations near the wave source is not obvious in the spatial dimension, while it exhibits apparent flow patterns close to the wave sinks. Moreover, as the four wave instabilities appears, the maxi-

mum fluctuation on the free surface occurs at the location close to the line AB due to the further squeezing and merging of wave instabilities. The oscillation period becomes longer, meanwhile the stripes in the STD are more complex, as shown in Figure 3.10, which is in agreement with the quasi-periodic oscillation shown in Figure 3.4(c).

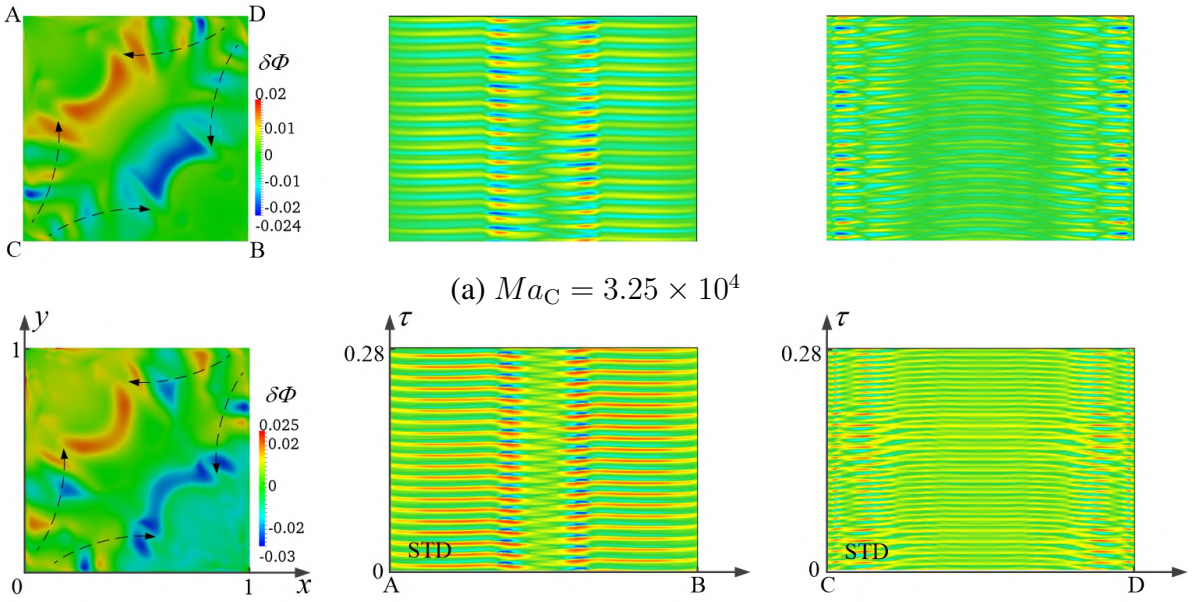

Figure 3.10 Snapshots of the surface concentration fluctuations and the corresponding space-time diagram (STD) along the diagonals AB and CD at $Sc = 10$. (a) $Ma_C = 3.25 \times 10^4$ and (b) $Ma_C = 4 \times 10^4$. The arrows in concentration fluctuations indicate the directions of wave propagation. The positions of the diagonals AB and CD are shown in Figure 3.1(b).

3.4.2 For high Schmidt number ($Sc = 100$)

Analogous to the role of Prandtl number (Pr) in examining thermal Marangoni flows, as pointed in previous studies [71, 96, 97], the Schmidt number plays a similar role in studying solutal Marangoni flows. Figure 3.12 shows the computed snapshots of the concentration fluctuations on the free surface and the corresponding space-time diagram (STD) at $Sc = 100$, at four different Marangoni number values; namely, $Ma_C = (0.225, 1.25, 2 \text{ and } 2.5) \times 10^4$. It is obvious from the STD of Figure 3.12(a)– Figure 3.12(d) that in all four cases, the oscillation frequencies and the concentration fluctuations are considerably smaller than those at $Sc = 10$ (see Figure 3.7).

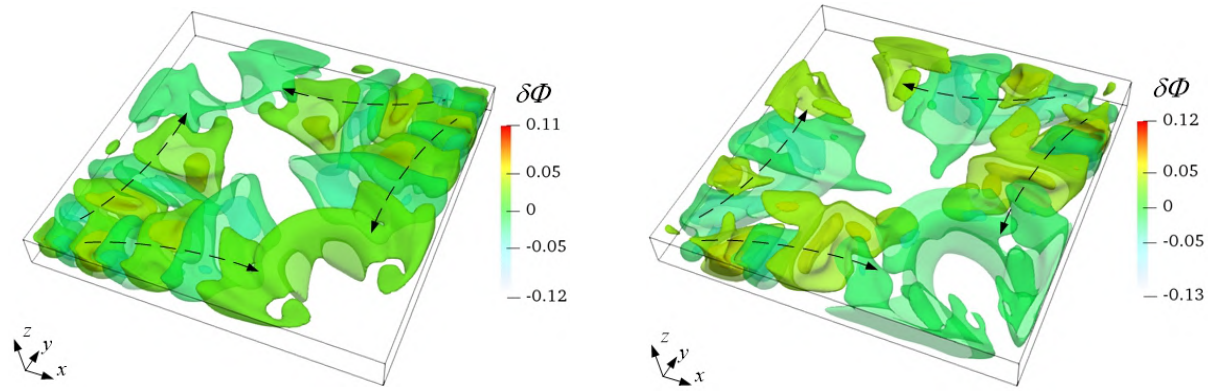

(a) $Ma_{\mathrm{C}} = 3.25 \times 10^4$ (b) $Ma_{\mathrm{C}} = 4 \times 10^4$

Figure 3.11 Isosurfaces of 3D concentration fluctuations in the whole domain at $Sc = 10$. (a) $Ma_{\mathrm{C}} = 3.25 \times 10^4$ and (b) $Ma_{\mathrm{C}} = 4 \times 10^4$. The arrows indicate the directions of wave propagation.

This is consistent with the report of Imaishi *et al.* [88] that the critical oscillation frequency from basic flow to oscillation mode becomes around 7 times lower when Pr increases from 10 to 100 in the case of thermal Marangoni flow. Liu *et al.* [35] also demonstrated that the critical oscillation frequency generally decreases with the increase of Pr.

At $Ma_{\mathrm{C}} = (0.225 \text{ and } 1.25) \times 10^4$, the concentration fluctuations become larger and gradually cover the whole free surface, as shown in Figure 3.12(a) and Figure 3.12(b). It is noteworthy that the maximum fluctuation of concentration on the free surface appears close to the diagonal AB at $Ma_{\mathrm{C}} = 1.25 \times 10^4$, in contrast to the result at $Ma_{\mathrm{C}} = 2.25 \times 10^3$. Because of an even more sensitive advective mechanism, the oscillation is easier to propagate to points A, B than the case of $Sc = 10$, the intensity of squeezing and merging of wave pattern dramatically increases. Thus, the maximum concentration fluctuation on the free surface appears close to the diagonal AB at $Ma_{\mathrm{C}} = 1.25 \times 10^4$. Furthermore, the isosurfaces of 3D concentration fluctuations in the whole domain are more distorted, as shown in Figure 3.13(b), and the wedge-like patterns are observed in comparison with the horseshoe-like patterns in Figure 3.8(b), while both cases keep the modes of SW1.

At $Ma_{\mathrm{C}} = 2 \times 10^4$, more complex fluid flow and STD develop, as seen in Figure 3.12(c). Since the concentration boundary layer occurs as shown in Figure 3.2(c) and Figure 3.2(d), the

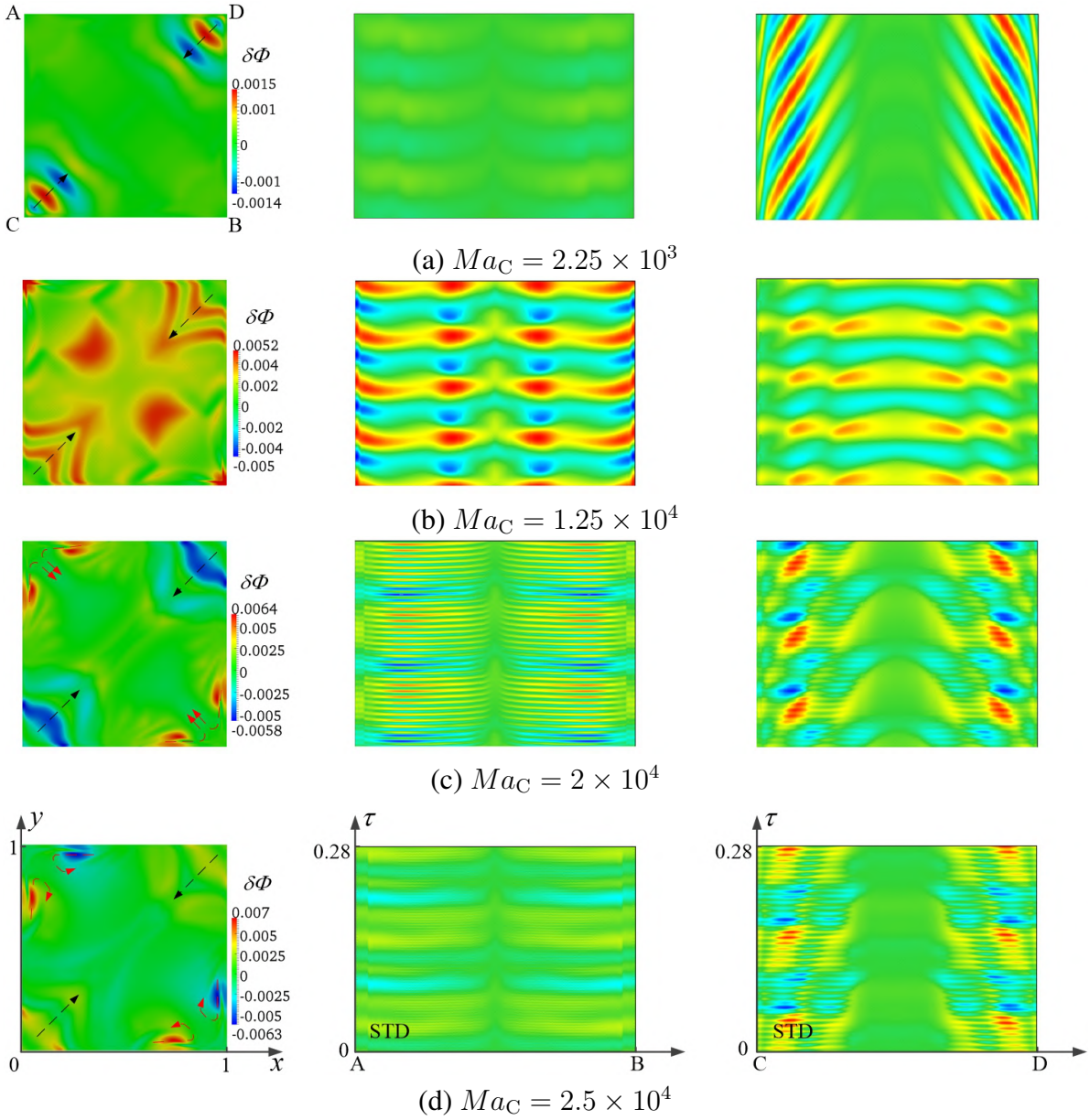

Figure 3.12 Snapshots of the surface concentration fluctuations and the corresponding space-time diagram (STD) along the diagonals AB and CD at $Sc = 100$. (a) $Ma_C = 2.25 \times 10^3$, (b) $Ma_C = 1.25 \times 10^4$, (c) $Ma_C = 2 \times 10^4$ and (d) $Ma_C = 2.5 \times 10^4$. The black and red arrows indicate the propagation directions of the dominant and secondary waves, respectively. The positions of diagonals AB and CD are shown in Figure 3.1(b).

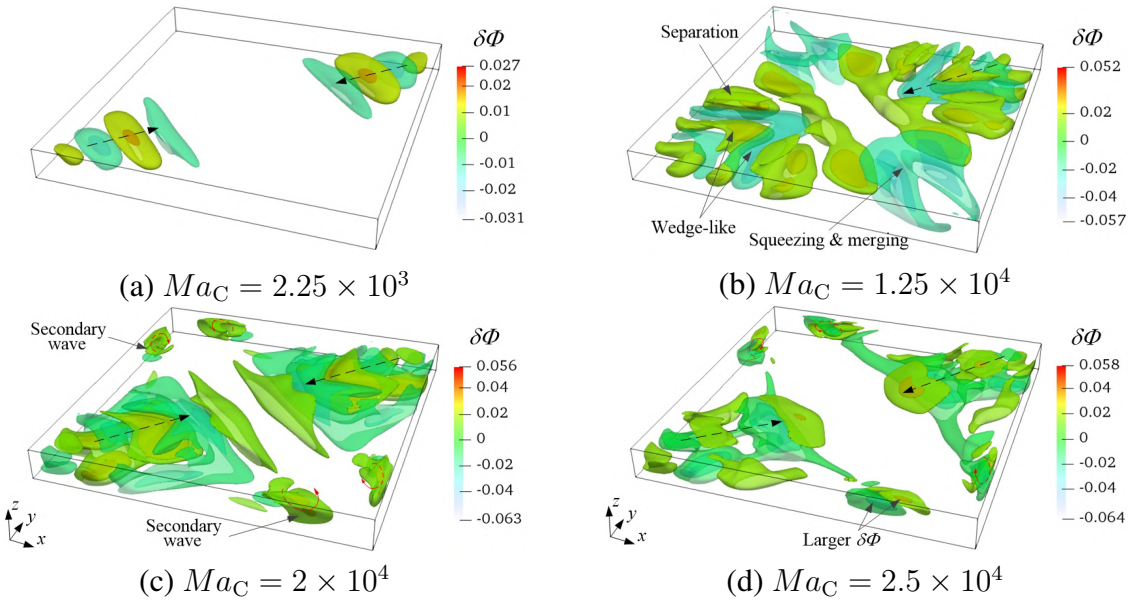

(a) $Ma_{\mathrm{C}} = 2.25 \times 10^3$ (b) $Ma_{\mathrm{C}} = 1.25 \times 10^4$

(c) $Ma_{\mathrm{C}} = 2 \times 10^4$ (d) $Ma_{\mathrm{C}} = 2.5 \times 10^4$

Figure 3.13 Isosurfaces of 3D concentration fluctuations in the whole domain at $Sc = 10$. (a) $Ma_{\mathrm{C}} = 2.25 \times 10^3$, (b) $Ma_{\mathrm{C}} = 1.25 \times 10^4$, (c) $Ma_{\mathrm{C}} = 2 \times 10^4$ and (d) $Ma_{\mathrm{C}} = 2.5 \times 10^4$. The black and red arrows indicate the propagation direction of the dominant and secondary waves, respectively.

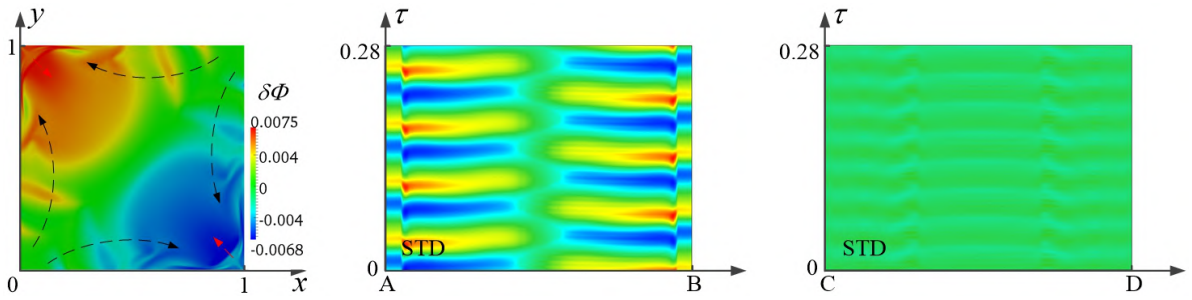

Figure 3.14 Snapshots of the surface concentration fluctuations and the corresponding space-time diagram (STD) along the diagonals AB and CD at $Sc = 100$ and $Ma_{\mathrm{C}} = 3 \times 10^4$. The black and red arrows indicate the propagation directions of the dominant and secondary waves, respectively.

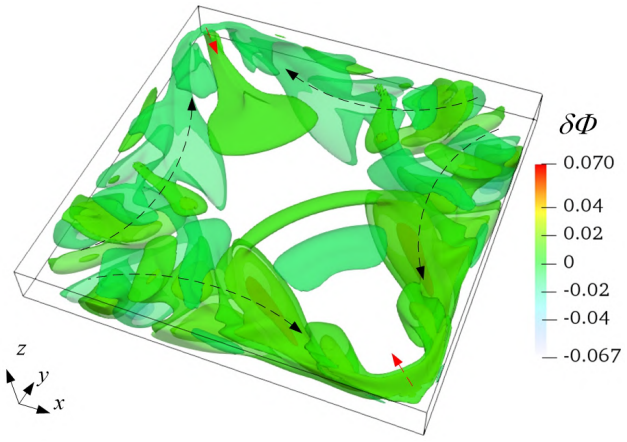

Figure 3.15 Isosurfaces of 3D concentration fluctuations in the whole domain at $Sc = 100$ and $Ma_{\mathrm{C}} = 3 \times 10^4$. The black and red arrows indicate the propagation directions of the dominant and secondary waves, respectively.

solutal Marangoni effect in the vicinity of points A, B would be stronger with the increase of Ma_{C}. Four new secondary waves begin to gestate and form, as shown in Figure 3.13(c), resulting in a sudden drop in the oscillation frequency, as depicted in the STD of Figure 3.12(c). The flow region is significantly affected by the development of multi-waves, and the concentration fluctuations in most areas of the free surface become relatively small, while the concentration oscillates sharply in the local area near the boundary corners.

At $Ma_{\mathrm{C}} = 2.5 \times 10^4$, the wave pattern changes from SW1 to a new symmetrical wave 3 (SW3), which is characteristically symmetrical only along the diagonal CD, as shown in Figure 3.12(d). At this solutal Marangoni number level, larger concentration fluctuations are observed in the vicinity of the sidewall of the corners due to the mutual interactions between the dominant and secondary waves, as shown in Figure 3.13(d). Again, due to the effect of the cavity walls, near corners (points A, B) every two secondary waves would separate near the free surface after coming close to the corner, and the oscillation mode is not synchronized anymore. As seen the STD along diagonal CD does not remain symmetrical. Note that in Figure 3.12(c), two secondary waves remain in the merging state instead of separating near the free surface after getting close to the corner.

Similar to the results described in the previous section, a symmetrical wave 2 (SW2) develops at the higher solutal Marangoni number value, as shown in Figure 3.14. At $Ma_{\mathrm{C}} = 3 \times 10^4$, one

dominant wave would separate into two, propagating respectively at a certain curvature towards points C, D. From Figure 3.15, it can be concluded that the dominant wave plays a leading role in most part of the domain, while the contribution of the secondary wave is relatively larger only near points A, B. Also, the maximum concentration fluctuation on the free surface is even closer to points A, B compared to the case at $Sc = 10$ shown in Figure 3.10. In addition, a series of curved stripes form on the STD associated with the diagonal AB due to the coupling effects of the dominant and secondary wave instabilities, as shown in Figure 3.14.

CHAPTER 4

THERMAL-SOLUTAL MARANGONI CONVECTION WITH MUTUALLY PERPENDICULAR TEMPERATURE AND CONCENTRATION GRADIENTS

Most previous studies considered only the cases of mutually parallel thermal and concentration gradients in a rectangular cavity. However, the case of mutually perpendicular gradients has not been considered yet. It would be an interesting phenomenon to investigate since it occurs in some processes such as painting and drying [41, 43]. In this chapter, a series of three-dimensional numerical simulations are performed to study thermal-solutal Marangoni convection in a shallow rectangular cavity under the effect of mutually perpendicular thermal and concentration gradients to shed further light on flow characteristics and flow pattern transitions.

4.1 The overall flow map

The flow regimes computed at various thermal and solutal Marangoni numbers are summarized in Figure 4.1. The flow regimes in this map are identified by the time variation of concentration and temperature values on the free surface at the sampling point (P) at $(x, y, z) = (0.5, 0.5, 0.1)$. In this figure we present the computed values at fixed thermal Marangoni numbers Ma_{T} (which are 0, 1, 3, and 7×10^4 along the horizontal axis) by varying the solutal Marangoni number Ma_{C} (presented along the vertical axis). For each value of Ma_{T}, the flow pattern changes from a steady to oscillatory and then to chaotic with the increase of the solutal Marangoni number. At the higher Ma_{C} values, generally all flow regimes become chaotic. The variation at $Ma_{\mathrm{T}} = 3 \times 10^4$ differs from the others; it becomes chaotic first after the oscillatory traveling mode, and then oscillatory again, and then finally chaotic at the higher Ma_{C} values like others. This will be discussed later in detail.

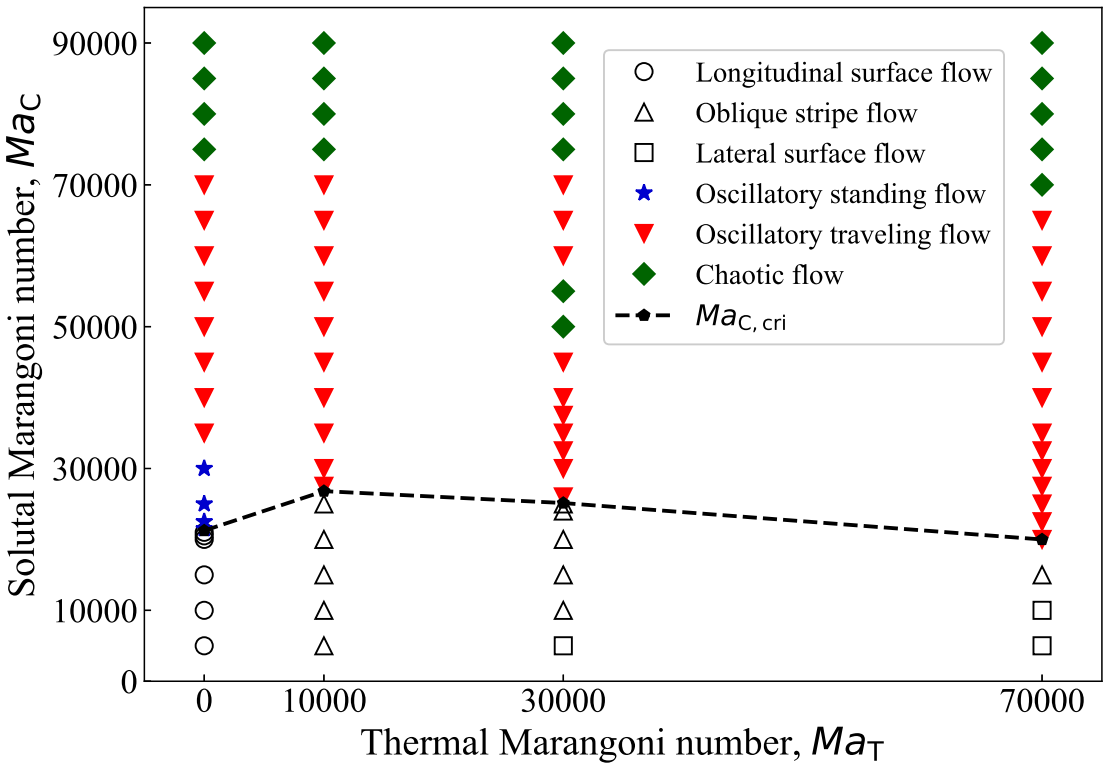

Figure 4.1 The (Ma_{T},Ma_{C}) map of computed flow regimes. The dashed line indicates the critical solutal Marangoni numbers at the fixed Ma_{T} values. In all cases, the flow is steady when Ma_{C} is smaller than a critical value and is unstable above this critical value.

4.2 Basic flow pattern

When Ma_{C} is relatively small, the Marangoni flow is steady, which is called the "basic flow" hereafter. Figure 4.2 shows the computed streamlines, isotherms, and iso-concentration lines of the basic flow at $Ma_{\mathrm{C}} = 1 \times 10^4$. It can be noted at this Ma_{C} level, the basic flow evolves into three types of steady flows (a longitudinal surface flow, an oblique stripe flow, and a lateral surface flow) with the increase of the thermal Marangoni number.

At $Ma_{\mathrm{T}} = 0$, only the solutal Marangoni convection develops (pure solutal Marangoni flow), and the fluid on the surface flows in the positive y-direction by the solutal Marangoni force, then returns back near the bottom due to the mass conservation, as seen in Figure 4.2(a). When Ma_{T} is higher than 0, the effect of the thermal Marangoni force kicks in. As seen in Figure 4.2(b,c), the surface fluid flows diagonally with flow velocity components in both the x- and y-directions. At the higher thermal Marangoni number, as seen in Figure 4.2(d), the fluid flow is almost in the x-direction. This means that the flow is dominated by the thermal Marangoni effect at this state.

The Prandtl number ($Pr = 0.01$) of the working fluid in the present work is much less than unity; it means that the heat transfer is basically by diffusion in the liquid. Thus, the isotherms of the primary basic flow are almost uniform and parallel to the left and right sidewalls. As noted however, the iso-concentration lines are much more distorted and the mass transport is sensitive to the flow regime due to the equal contributions ($Sc = 1$) of the diffusion and advective mechanisms, as seen in Figure 4.2. The variation of the concentration gradient along line AB (at $x = 0.5$) on the free surface is plotted in Figure 4.3. The position of the AB line is shown in Figure 4.2(a). As seen from the figure, the solutal concentration boundary layers are thinner in the vicinity of the back sidewall ($y = 1$) at $Ma_{\mathrm{T}} = 0$. At the higher thermal Marangoni number, the contribution of solutal Marangoni flow decreases, the local maximum concentration gradients rapidly get lower, and the overall concentration distribution becomes relatively uniform.

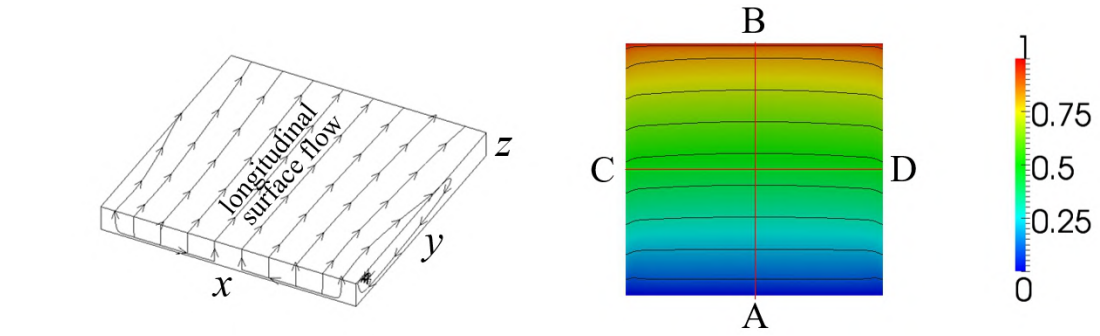

(a) $Ma_{\mathrm{T}} = 0$

(b) $Ma_{\mathrm{T}} = 1 \times 10^4$

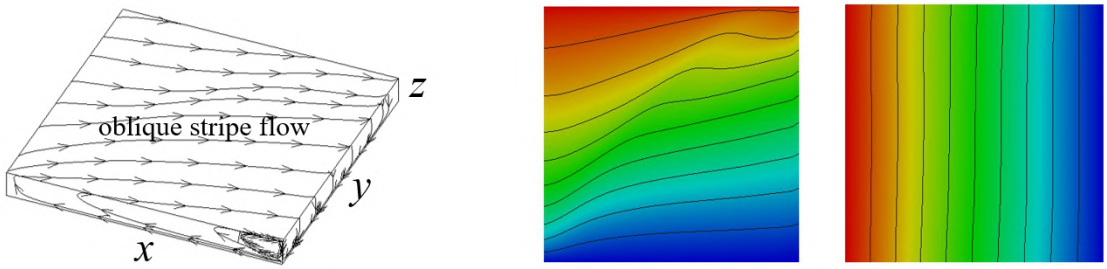

(c) $Ma_{\mathrm{T}} = 3 \times 10^4$

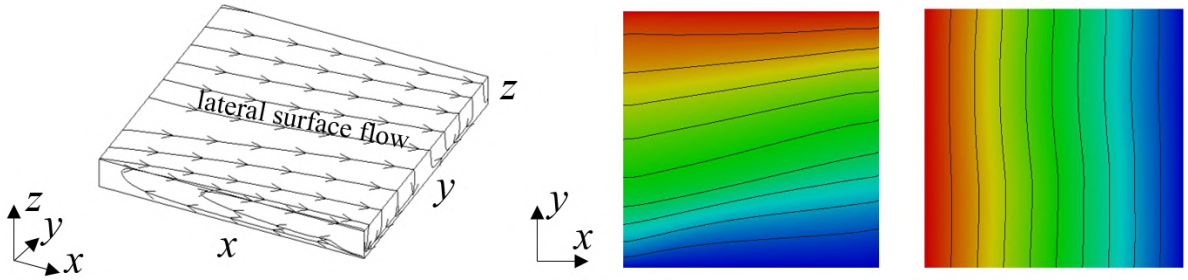

(d) $Ma_{\mathrm{T}} = 7 \times 10^4$

Figure 4.2 Streamlines along the boundaries (left), iso-concentration lines (middle) and isotherms (right) on the top free surface as $Ma_{\mathrm{T}} = 1 \times 10^4$. The contour values of temperature and concentration are from 0.1 to 0.9 with steps of 0.1.

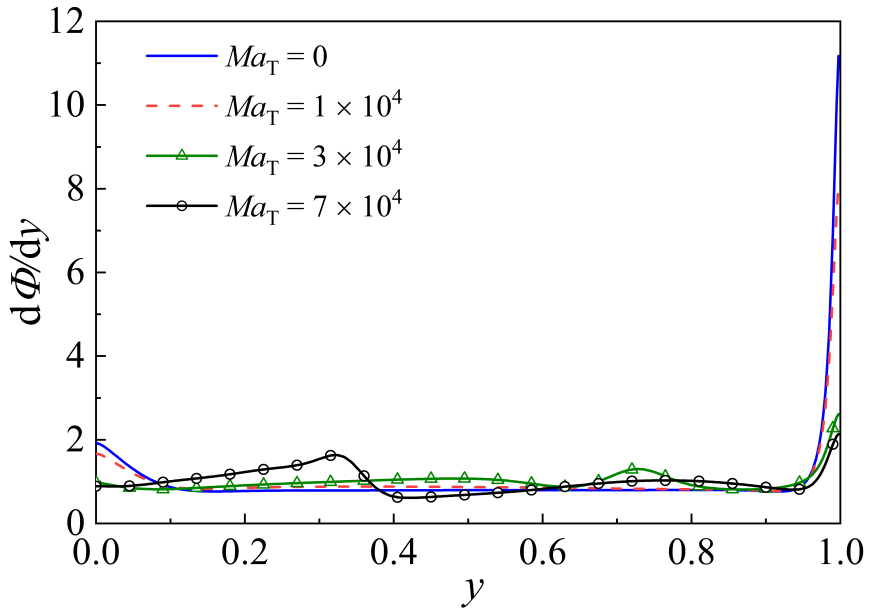

Figure 4.3 Distribution of the concentration gradient along line AB on the free surface at $Ma_{\mathrm{C}} = 1 \times 10^4$ without/with radiation.

4.3 Critical Marangoni number

As mentioned earlier, at all the selected thermal Marangoni numbers, the basic flow may become unsteady and bifurcate into different three-dimensional oscillatory flows once the solutal Marangoni number exceeds a critical value; called the "critical" solutal Marangoni number ($Ma_{\mathrm{C,cri}}$). In Figure 4.4, the variations of temperature A_{T} and concentration A_{C} at a sampling point (A) on the free surface are plotted at $Ma_{\mathrm{T}} = 1 \times 10^4$. As seen, the temperature and concentration amplitudes increase linearly with Ma_{C}. The critical solutal Marangoni number, $Ma_{\mathrm{C,cri}}$ are estimated by means of the linear extrapolation method [98]. The critical solutal Marangoni numbers values, which depend on the corresponding thermal Marangoni number Ma_{T}, are given in Figure 4.1 (the dash line). At smaller Ma_{T} values, the solutal Marangoni effect is dominant in the whole system. On the other hand, the local maximum concentration gradient is weakened (see Figure 4.3), thus a larger Ma_{C} value is needed to make the flow unsteady. At large Ma_{T} values, the thermal Marangoni effect is dominant, thus only a small Ma_{C} value can also destabilize the flow. As a result, as seen, the value of $Ma_{\mathrm{C,cri}}$ firstly increases and then decreases at a slope of

about 0.1 with the increasing thermal Marangoni number.

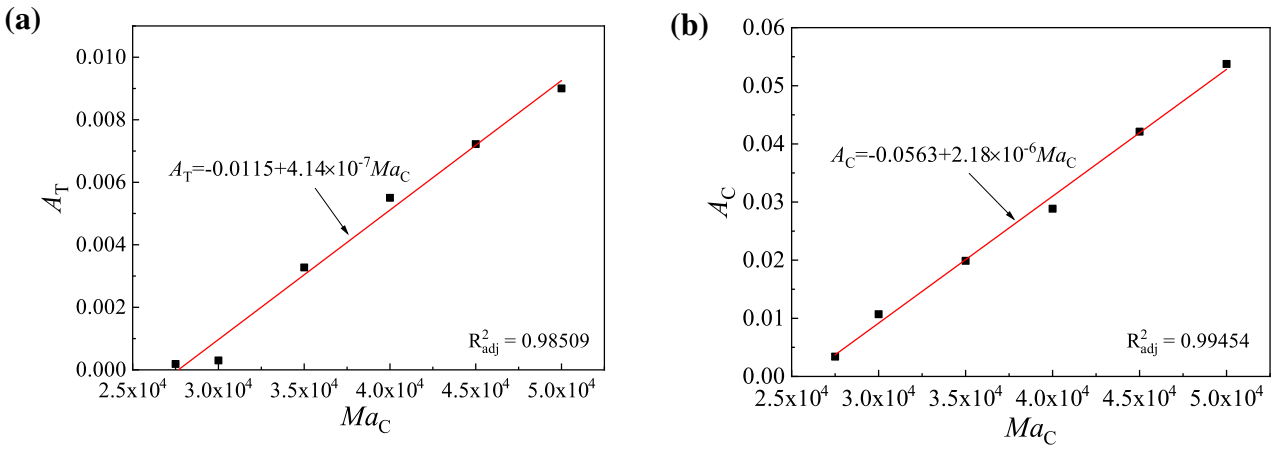

Figure 4.4 Variations of temperature amplitude A_{T} and concentration amplitude A_{C} with time at $Ma_{\mathrm{T}} = 1 \times 10^4$.

4.4 Oscillatory flow

4.4.1 Characteristics of the thermal-solutal Marangoni oscillatory flow

When the solutal Marangoni number exceeds the critical value $Ma_{\mathrm{C,cri}}$, the thermal-solutal Marangoni flow bifurcates to an oscillatory flow. Figure 4.5 presents the computed time dependencies of temperature, concentration and longitudinal velocity component at a sampling point (P) at $(x, y, z) = (0.5, 0.5, 0.1)$, and the corresponding frequency spectra at $Ma_{\mathrm{T}} = 1 \times 10^4$ and $Ma_{\mathrm{C}} = 3 \times 10^4$. The velocity oscillation, V_y, due to the inertial effect of fluid flow is always delays. There is a phase difference between temperature, concentration, and flow velocity variations. Their coupling leads to the development of instabilities in the form of hydrothermal waves (HTW) and hydrosolutal waves (HSW) on the free surface (as seen from Figure 4.8(a)). A similar phase difference in HTW, or in HSW, was also reported in Refs. [18, 57]. Meanwhile, the same frequencies ($F = 262.81$) are observed in the frequency spectra shown in Figure 4.5(b).

Figure 4.6 presents the variation of concentration at the sampling point (A) with time and its frequency spectra at $Ma_{\mathrm{T}} = 7 \times 10^4$. Variations were calculated for three solutal Marangoni numbers: Ma_{C} =(2.25, 5 and 7) $\times 10^4$. At the small solutal Marangoni number value, i.e., $Ma_{\mathrm{C}} =$

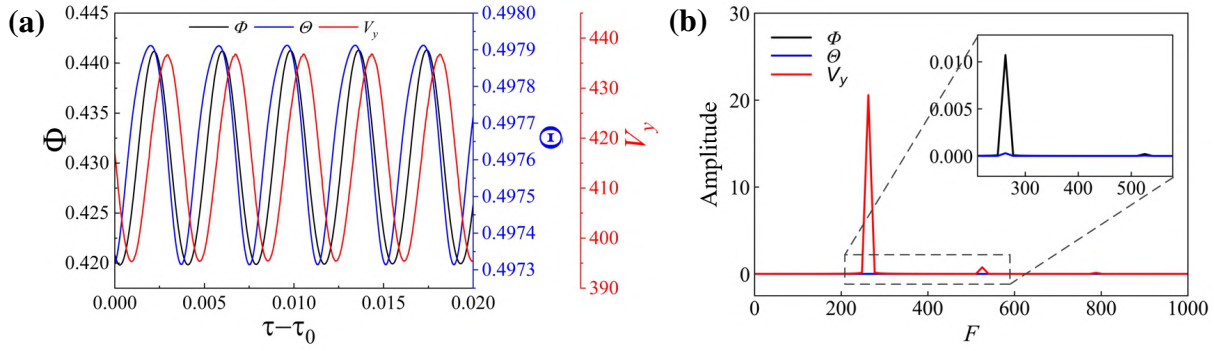

Figure 4.5 Time variations of the velocity, temperature and concentration at the sampling point A (a) and their frequency spectra (b) at $Ma_{\mathrm{T}} = 1 \times 10^4$ and $Ma_{\mathrm{C}} = 3 \times 10^4$.

2.25×10^4, the concentration oscillation amplitude is small and constant, with only one fundamental frequency $F_1 = 300$ and two harmonic frequencies $F_2 = 2F_3/3 = 2F_1$, as shown in Figure 4.6(a). When the solutal Marangoni number is larger, i.e., $Ma_{\mathrm{C}} = 5 \times 10^4$, the variation of concentration oscillates like an amplitude modulation (AM) wave, the amplitude still varies periodically with time at the sampling point, which has more complicated frequency spectra. At the highest solutal Marangoni number value, i.e., $Ma_{\mathrm{C}} = 7 \times 10^4$, the concentration oscillation is not periodic. No obvious dominant frequency can be detected in the spectra, and the Marangoni flow becomes completely chaotic. The same evolution process can also be observed in pure thermal or solutal Marangoni convection [28, 99].

4.4.2 Wave pattern evolution

In order to quantitatively investigate the three-dimensional disturbances, a fluctuation quantity (δW) over one period is introduced as,

$$\delta W(x, y, z, \tau) = W(x, y, z, \tau) - \frac{1}{\tau_p} \int_{\tau_0}^{\tau_0 + \tau_p} W(x, y, z, \tau) d\tau \tag{4.1}$$

where W can be Θ or Φ.

When the case of pure solutal Marangoni convection ($Ma_{\mathrm{T}} = 0$) is considered, the associated flow exhibits two different wave-type oscillations. Figure 4.7 shows the computed snapshots of the concentration fluctuations on the free surface and the streamlines at a plane at $y = 0.5$ (the

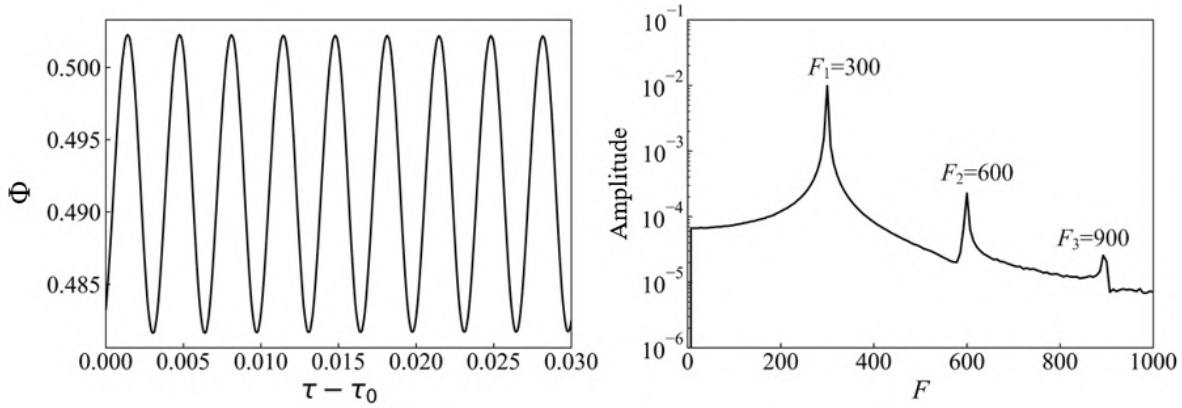

(a) $Ma_{\mathrm{C}} = 2.25 \times 10^4$

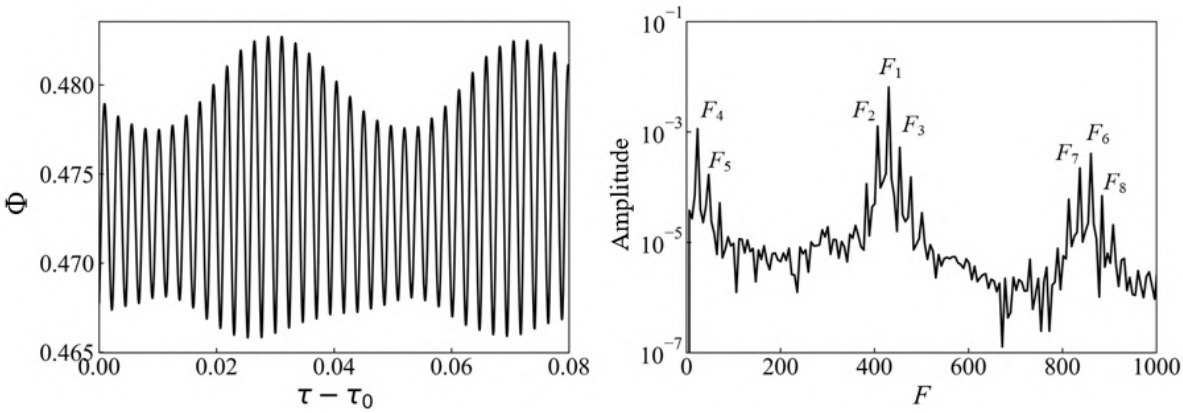

(b) $Ma_{\mathrm{C}} = 5 \times 10^4$

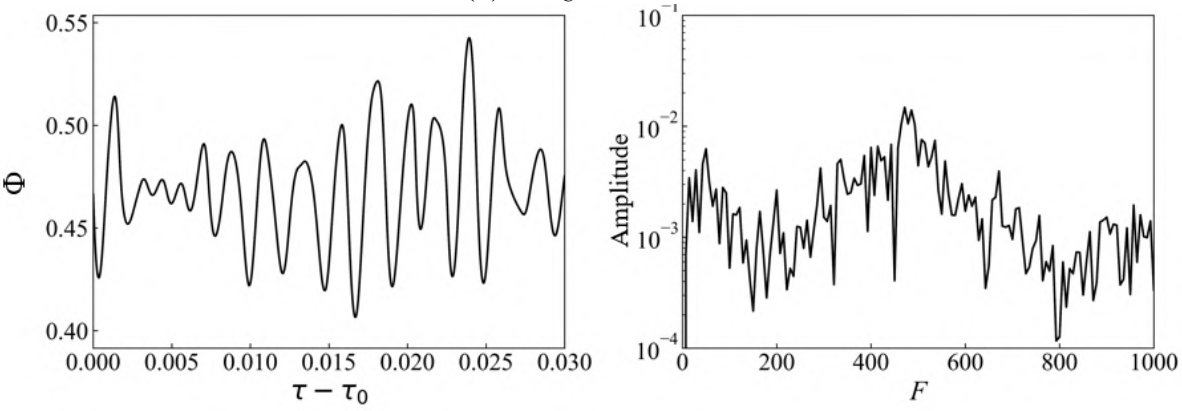

(c) $Ma_{\mathrm{C}} = 7 \times 10^4$

Figure 4.6 Variation of concentration at the sampling point A with time and its frequency spectra at $Ma_{\mathrm{T}} = 7 \times 10^4$.

C–D plane as shown in Figure 4.2(a)), at two different solutal Marangoni number values; namely, Ma_{C} =(2.15 and 5) $\times 10^4$. At $Ma_{\mathrm{C}} = 2.15 \times 10^4$, the concentration wave pattern resembles a checkerboard-like configuration and propagates in the negative y-direction. The mechanism of instability in the flow pattern is the periodical evolution of rolling cells, as shown in the streamlines in Figure 4.7(a). A similar flow pattern has been reported by Chen *et al.* [40] for the oscillatory flow in a thin annular pool, and they called this kind of oscillation the "standing-wave type oscillation". As the solutal Marangoni number further increases, i.e., at $Ma_{\mathrm{C}} = 5 \times 10^4$, as seen in Figure 4.7(b), the amplitudes of oscillations get larger, and the wave pattern changes from a standing wave to a HSW. The propagation angle of HSW φ_{C} is about 51°. Smith and Davis [13] reported that, for an infinite pure fluid layer with $Pr = 1$, the propagation angle of HTW is about 54°, which is close to that of the present HSW. Also, from Figure 4.7(b) we see that a secondary instability occurs. The symmetry of streamlines is broken, resulting in the generation of HSW. The secondary instability should be attributed to the occurrence of pitchfork bifurcation, as pointed previously [55].

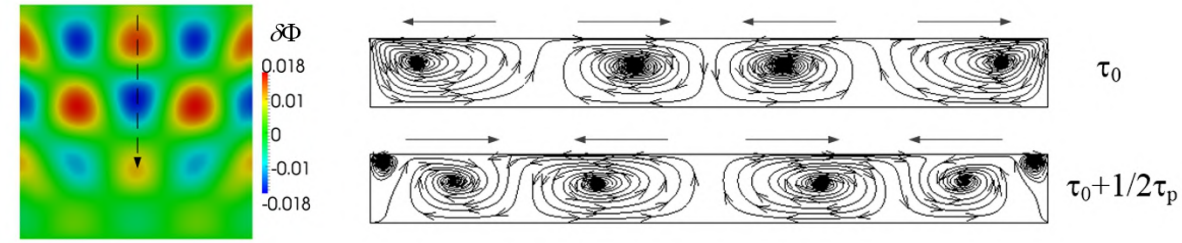

(a) $Ma_{\mathrm{C}} = 2.15 \times 10^4$

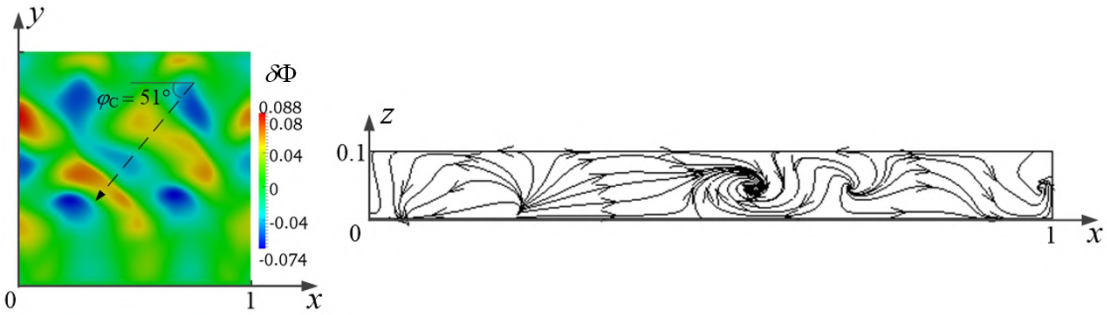

(b) $Ma_{\mathrm{C}} = 5 \times 10^4$

Figure 4.7 Snapshots of surface concentration fluctuations (left) and the streamlines (right) at the C–D plane ($y = 0.5$) at $Ma_{\mathrm{T}} = 0$. The arrows in the left figures indicate the direction of wave propagation.

Next considering a case where both the thermal and solutal Marangoni effects are in place. For this case, three different thermal Marangoni number values, namely Ma_{T} =(1, 3 and 7) $\times 10^4$, are used at the value of $Ma_{\mathrm{C}} = 3 \times 10^4$. Results are presented in Figure 4.8. In all three cases, the fluctuations of temperature and concentration on the free surface form HTWs and HSWs, respectively, propagating at a certain angle with respect to the negative x-axis. As seen from the figure, the space-time diagram (STD) consists of a series of parallel tilted stripes. It is evident from Figs. Figure 4.8(a)-(c) that in all three cases the maximum fluctuation of temperature is proportional to the thermal Marangoni effect although it is far less than that of the concentration due to the large Lewis number of the working fluid.

At $Ma_{\mathrm{T}} = 1 \times 10^4$ and $Ma_{\mathrm{C}} = 3 \times 10^4$, the solutal Marangoni effect is dominant (solutal Marangoni number is larger), as also seen in Figure 4.3. The wave patterns of HTW and HSW are similar, and both patterns propagate from the upper-right corner towards the lower-left corner as shown in Figure 4.8(a). Since the relative contribution of solutal Marangoni effect along the x-axis in the negative direction gradually increases, and the iso-concentration line is denser in the vicinity of the left sidewall ($x = 0$) shown in Figure 4.2(b), the stripes on the STD bends slightly inward, which is synchronously accompanied by the enhancement of temperature and concentration fluctuations during the propagation. Chen *et al.* [45] also reported such HTWs and HSWs under the effects of mutual parallel temperature and concentration gradients, while the wave pattern was more regular and straightforward in the spatiotemporal distribution than the present cases because the thermal and solutal Marangoni forces could suppress or enhance each other in only one dimension.

At $Ma_{\mathrm{T}} = 7 \times 10^4$ and $Ma_{\mathrm{C}} = 3 \times 10^4$, the thermal Marangoni effect is dominant (thermal Marangoni number is larger), and the propagation is towards the upper-left corner, as seen in Figure 4.8(c). It appears that the maximum fluctuations of temperature and concentration are close to the top corner due to a higher temperature gradient near the cold sidewall ($x = 1$), which is consistent with the prediction made in the case of pure Marangoni convection by Liu *et al.* [35]. Also, the strips of both STDs are almost parallel to the x-axis, which means the HTW and HSW

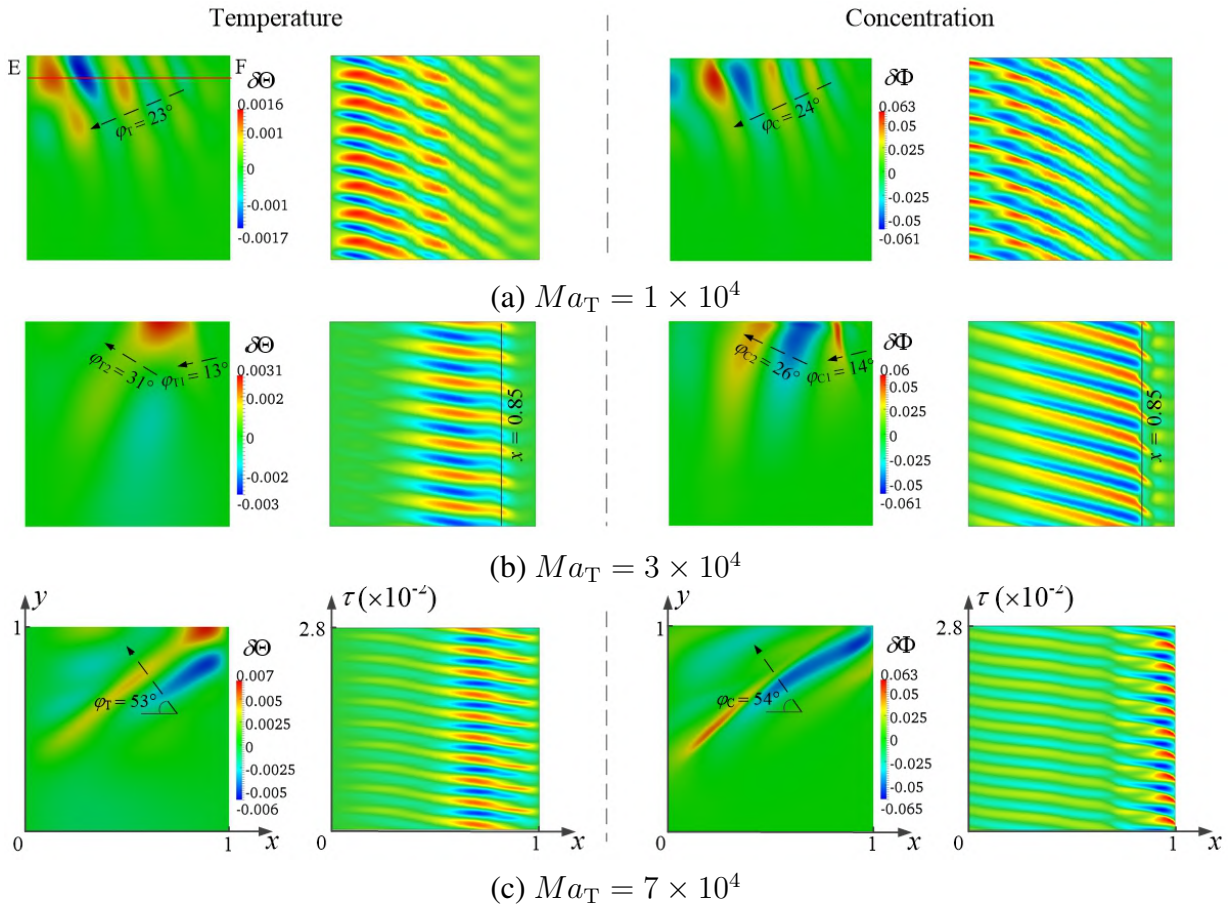

(a) $Ma_{\mathrm{T}} = 1 \times 10^4$

(b) $Ma_{\mathrm{T}} = 3 \times 10^4$

(c) $Ma_{\mathrm{T}} = 7 \times 10^4$

Figure 4.8 Snapshots of the surface temperature (left) and concentration (right) fluctuations and the corresponding space-time diagram (STD) at the EF line ($y = 0.9$) at $Ma_{\mathrm{C}} = 3 \times 10^4$. The arrows in HTW and HSW indicate the directions of wave propagation. In addition, the dimensionless time τ for all STDs is 0.028, and the position of the EF line is shown in Figure 4.8(a).

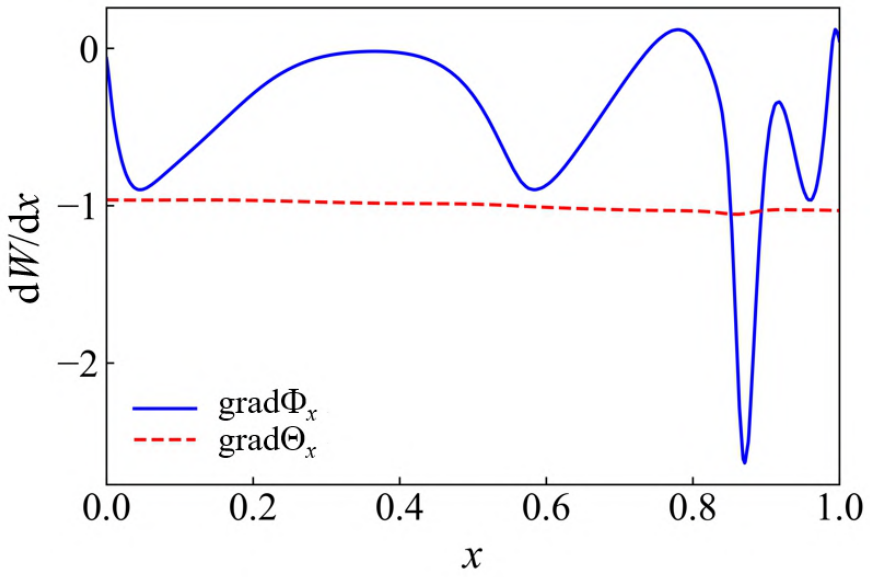

Figure 4.9 Distribution of the temperature and concentration gradients along $y = 0.9$ (the EF line in Figure 4.8) on the free surface at $Ma_{\mathrm{T}} = 3 \times 10^4$ and $Ma_{\mathrm{C}} = 3 \times 10^4$. W is Θ or Φ.

also have some characteristics of standing wave type oscillations as seen in Figure 4.7(a).

At $Ma_{\mathrm{T}} = 3 \times 10^4$ and $Ma_{\mathrm{C}} = 3 \times 10^4$, the overall contributions of thermal and solutal Marangoni effects are in the same order (thermal and solutal Marangoni numbers are equal). However, as shown in Figure 4.9, the value of concentration gradient (Φ_x) along x-axis at $y = 0.9$ (the EF line in Figure 4.8) varies widely and is larger than the temperature gradient (Θ_x) in the local region ($x \approx 0.85$), while Θ_x remains around -1 due to the small Prandtl number of the working fluid. Note that in Figure 4.8(a) and Figure 4.8(c) the propagation directions of HTW and HSW were in one direction only. In Fig.9(b), however, we see both directions appear at the same time. This simultaneous appearance is due to the fact that the thermal and solutal Marangoni effects have comparable contributions in this case. In addition, a series of curved narrow stripes appear at $x \approx 0.85$ on the STD due to the mutual interactions between the thermal and solutal Marangoni flows.

4.4.3 Frequency drop of oscillatory flow and backward transition to a chaotic flow

The Marangoni number has a significant influence on the frequency of the oscillatory flow. Figure 4.10 shows the frequency value at the sampling point (A) as a function of Ma_{C} for each Ma_{T}. The frequency monotonically increases at $Ma_{\mathrm{T}} = 0$. When the thermal Marangoni effect is included, as shown in Figure 4.11, only one wave instability exists near the back sidewall ($y = 1$) at $Ma_{\mathrm{C}} = 3 \times 10^4$, while another wave instability is observed near the front sidewall ($y = 0$), which propagates from the lower-left corner to upper-right when Ma_{C} increases to 3.5×10^4. Since the signals at the sampling point (A) will be affected by the two waves, a sudden drop occurs in the frequency, as seen in Figure 4.10.

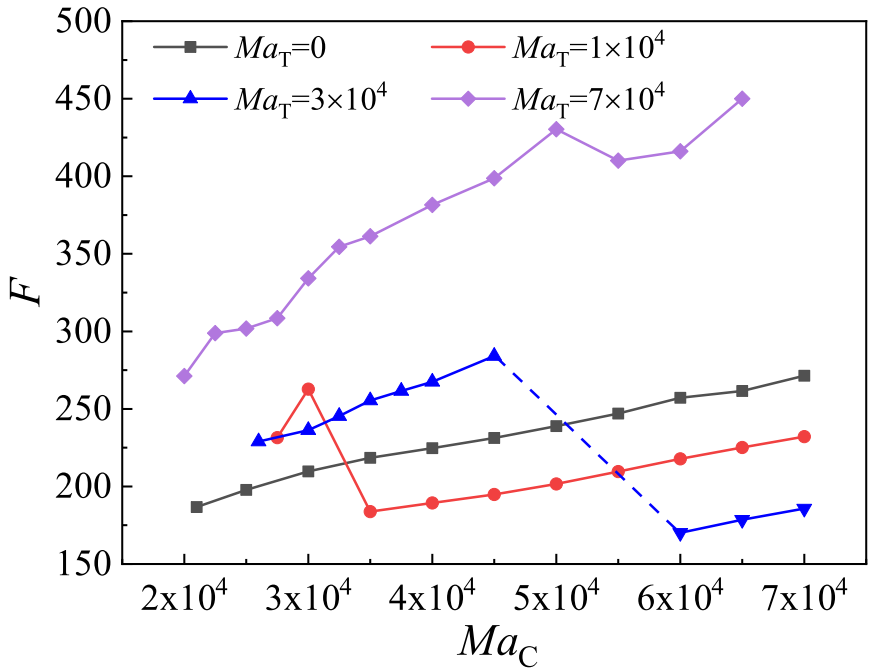

Figure 4.10 Variation of the oscillation frequency F with the solutal Marangoni number Ma_{C} for each thermal Marangoni number Ma_{T} at the sampling point A.

It is noteworthy that the flow undergoes a backward transition from the oscillatory flow to a chaotic one at around $Ma_{\mathrm{C}} \approx 5 \times 10^4$, then to an oscillatory pattern again (see the dashed line in Figure 4.10) when the thermal Marangoni number is around 3×10^4. Figure 4.12 shows the snapshots of concentration surface fluctuation and its STD at $Ma_{\mathrm{T}} = 3 \times 10^4$. The wave pattern

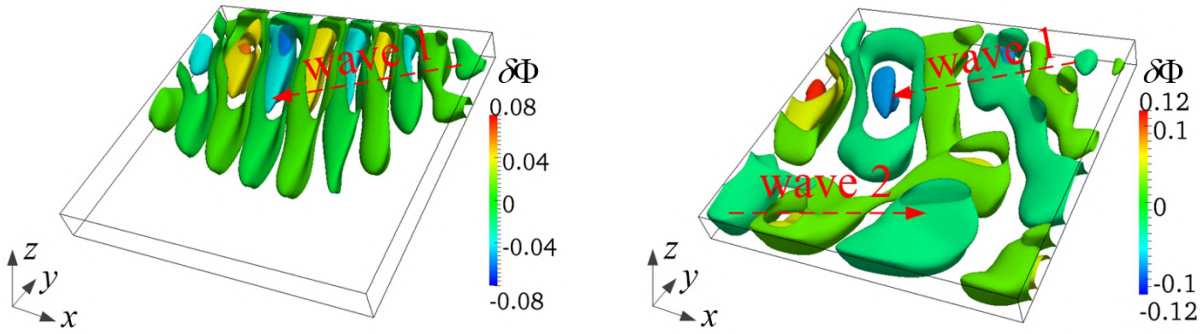

(a) $Ma_{\mathrm{C}} = 3 \times 10^4$ (b) $Ma_{\mathrm{C}} = 3.5 \times 10^4$

Figure 4.11 Isosurfaces of 3D concentration fluctuations at $Ma_{\mathrm{T}} = 1 \times 10^4$.

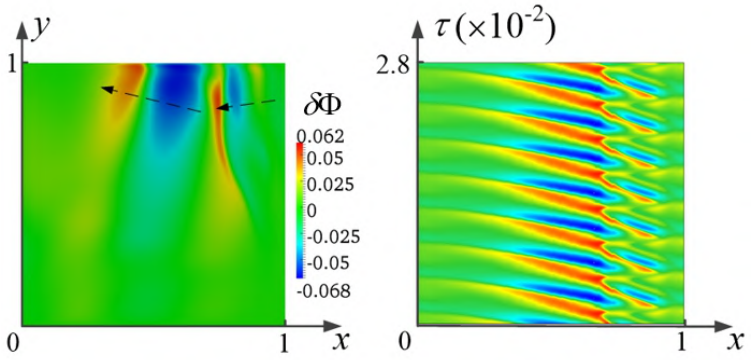

(a) $Ma_{\mathrm{C}} = 4 \times 10^4$

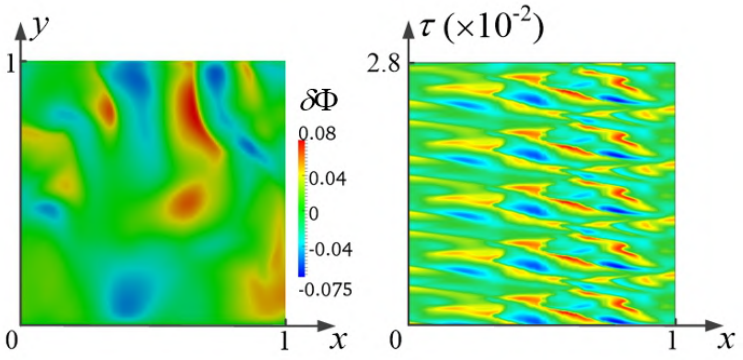

(b) $Ma_{\mathrm{C}} = 6 \times 10^4$

Figure 4.12 Snapshots of concentration surface fluctuations (left) and the corresponding STD (right) at the EF line ($y = 0.9$) at $Ma_{\mathrm{T}} = 3 \times 10^4$. The position of the EF line is shown in Figure 4.8(a)

in Figure 4.12(a) is similar to that shown in Figure 4.8(b) at $Ma_{\mathrm{C}} = 4 \times 10^4$, while there is no obvious wave pattern in concentration fluctuation at $Ma_{\mathrm{C}} = 6 \times 10^4$, which means that the flow developed becomes more complex due to the stronger solutal Marangoni effect. However, in the STD of Figure 4.12(b), the concentration fluctuations are still regular in time. As demonstrated in Figure 4.13, the longitudinal velocity V_y at the sampling point is quasi-periodic for $Ma_{\mathrm{C}} = 6 \times 10^4$, but the flow velocity fluctuates irregularly in time at $Ma_{\mathrm{C}} = 5 \times 10^4$. Although, as the solutal Marangoni number increases, the temporal complexity of the flow reduces from chaotic to the secondary oscillatory flow, the spatial flow pattern changes from two vortices to five coherent vortices as seen in Figure 4.14. As a result, since the overall complexity of the flow increases, the appearance of the backward transition from chaotic to oscillatory is reasonable. Zhan *et al.* [55] have also analyzed the rationality of backward transition using dynamic theory, while the flow goes from chaotic into the steady state. In addition, the same backward transition from chaotic to an oscillatory flow in the thermal and solutal Marangoni flows of opposite directions in a liquid bridge was also numerically observed by Jin *et al.* [84].

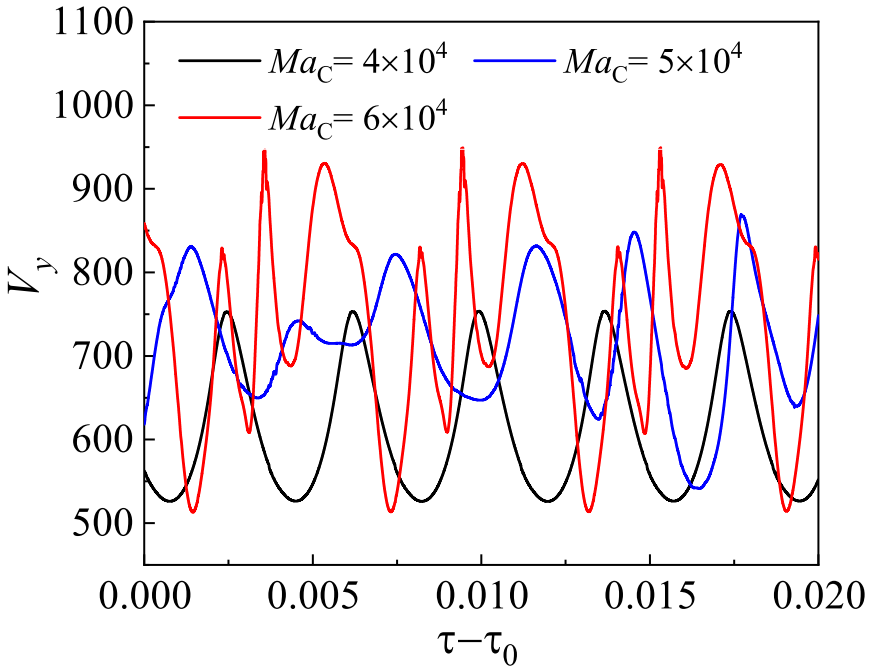

Figure 4.13 Time dependency of the longitudinal velocity V_y at various solutal Marangoni numbers Ma_{C} at the sampling point A at $Ma_{\mathrm{T}} = 3 \times 10^4$.

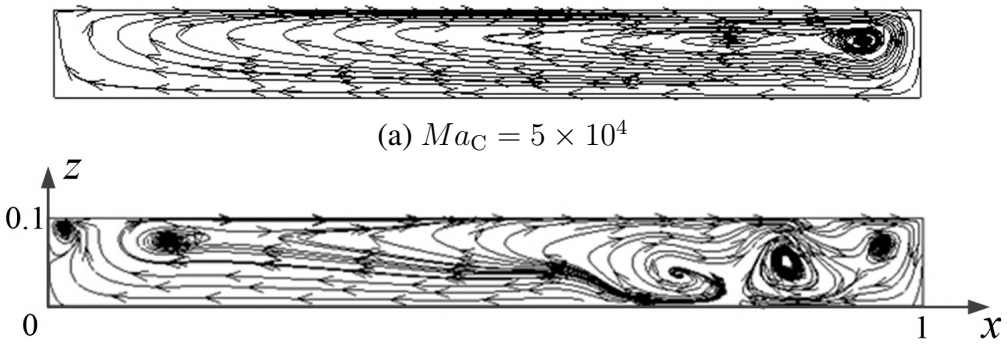

(a) $Ma_{\mathrm{C}} = 5 \times 10^4$

(b) $Ma_{\mathrm{C}} = 6 \times 10^4$

Figure 4.14 Streamlines at the C–D plane ($y = 0.5$) at $Ma_{\mathrm{T}} = 3 \times 10^4$.

4.5 Comparison with a cylindrical configuration

4.5.1 Onset of flow instabilities

It is well known that the configurations have an important influence on the instabilities of Marangoni flow. Many studies in two basic rectangular and cylindrical configurations have been reported on the investigation of Marangoni effect. Therefore, it would be an interesting phenomenon to analyze the difference between these two configurations.

Figure 4.12 shows the variation of critical solutal Marangoni number with Marangoni ratio in the present rectangular and previous cylindrical cases. It is worthy to note that, in the previous case by Agampodi Mendis *et al.* [58], the Schmidt number ($Sc = 14$) of working fluid is larger than the unity, while the Prandtl number value is close to the present study. Similar to the result described in the last chapter, the flow disturbance gestate and develop easily at a higher Schmidt number, thus the critical solutal Marangoni number $Ma_{\mathrm{C,cri}}$ with respect to the cylindrical case is around 10 times smaller than that of the present case. In addition, with the increase of Marangoni ratio Ma_σ, $Ma_{\mathrm{C,cri}}$ values for both two cases show the same tendencies overall, namely, first increase and then decrease. For the cylindrical configuration, the thermal and solutal Marangoni flows are in the opposite direction, the $Ma_{\mathrm{C,cri}}$ value first increases at small Ma_σ due to the suppression effect of combined thermal and solutal Marangoni flows. When $Ma_\sigma > 1$, the thermal Marangoni effect becomes dominant. As shown in the black line of Figure 4.12, $Ma_{\mathrm{C,cri}}$ decreases rapidly,

it is caused by the instability effect of thermal Marangoni flow on the flow behavior in the whole system. In response to the rectangular configuration, owing to the mutually perpendicular thermal and concentration gradients, the suppression and enhancement effects of coupling thermal and solutal Marangoni flows in the whole system coexist. Therefore, the inflection point (see red line) appears at $Ma_\sigma < 1$.

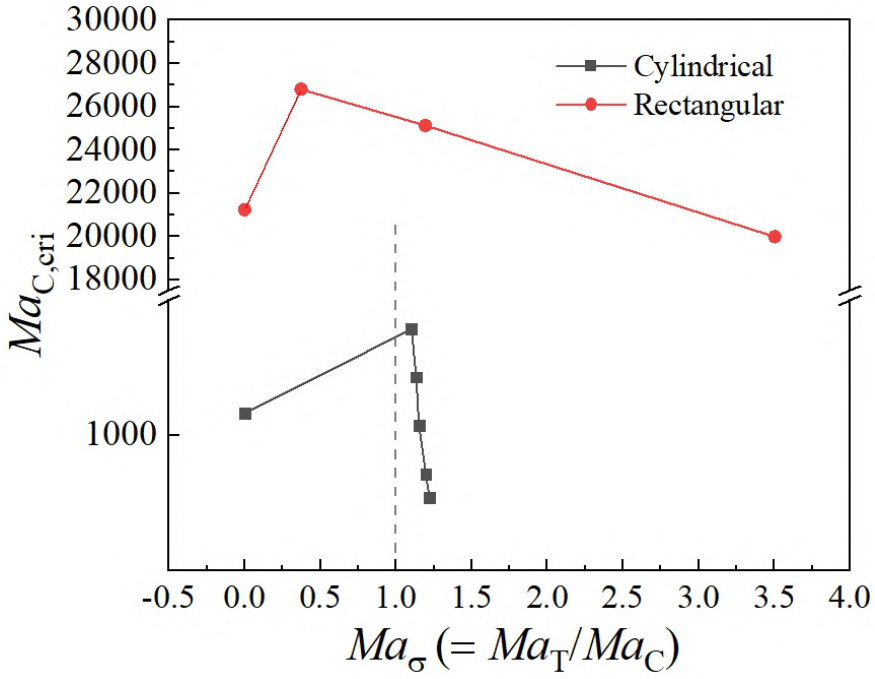

Figure 4.15 The variation of critical solutal Marangoni number with Marangoni ratio in the rectangular case (present study) and cylindrical case (reported by Laknath *et al.* [58]).

4.5.2 Wave pattern evolution

As summarized in Figure 4.1, there are mainly two kinds of oscillatory wave patterns, namely, standing wave and traveling wave. Figure 4.16 and Figure 4.17 present such two oscillatory waves in the cases of rectangular and cylindrical configurations. The appearance of oscillatory standing wave results from the periodical evolution of rolling cells, and the stationary longitudinal rolls exist in the whole system, as pointed in the work of Smith and Davis [13]. It is obvious from Figure 4.16(a) and Figure 4.17(a) that the standing wave propagates in the longitudinal direction for both configurations. However, due to the effect of the rectangular cavity wall, the flow pattern

close to the left and right sidewalls cannot sufficiently progress, and wave patterns are squeezed to extent. In addition, the wave patterns of checkerboard-like and strip-like are respectively observed in the rectangular and cylindrical configurations, it may be induced by the fluid properties and aspect ratio.

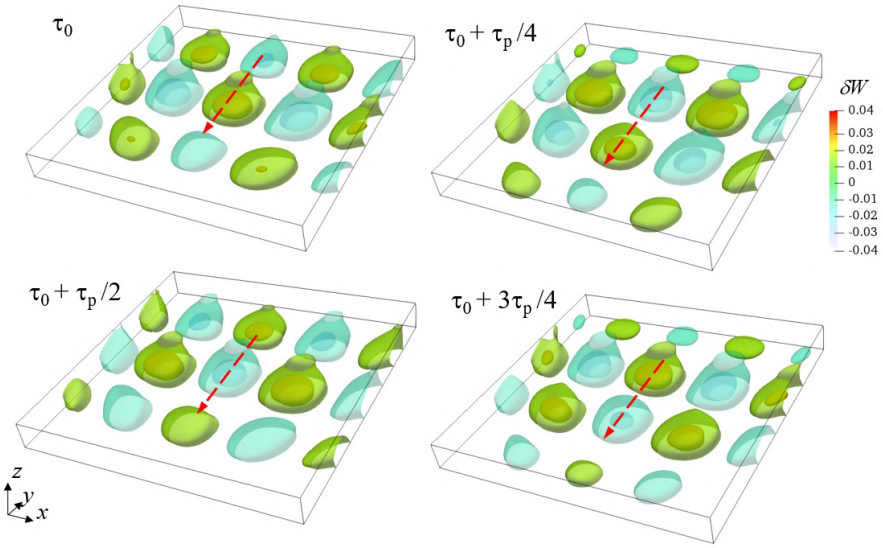

(a) Standing wave

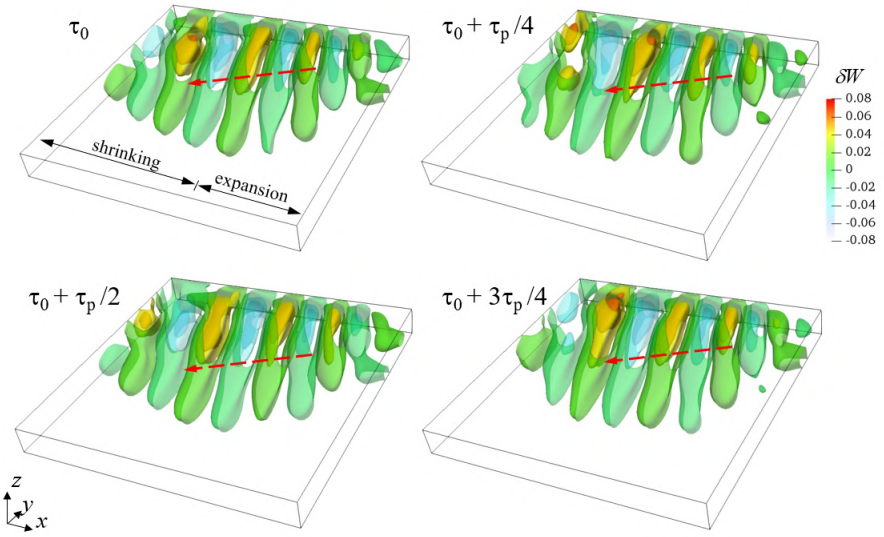

(b) Travelling wave

Figure 4.16 Standing wave (a) and travelling wave (b) inside a rectangular cavity. The red arrows in the figures indicate the direction of wave propagation. W is Θ or Φ.

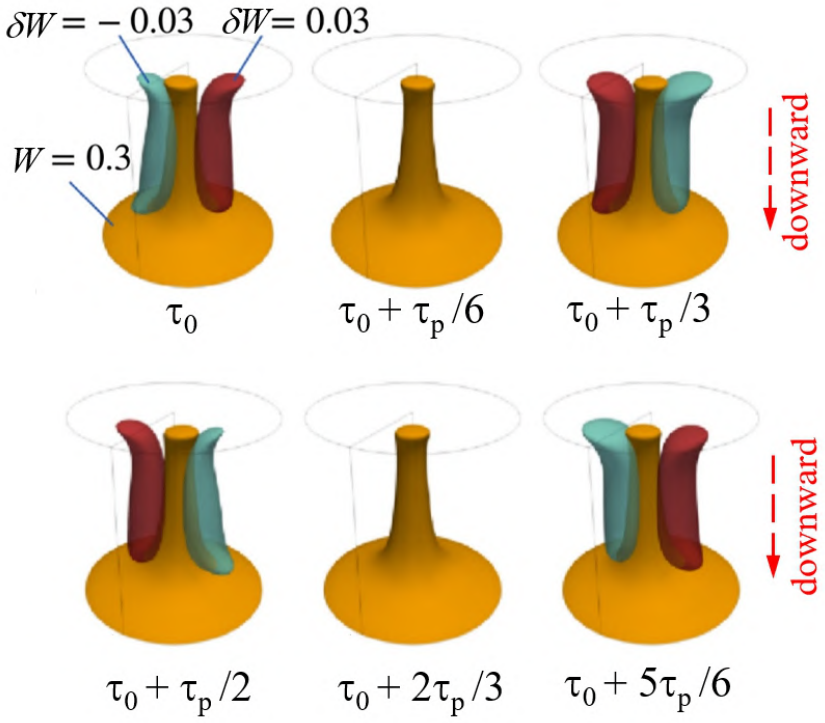

(a) Standing wave

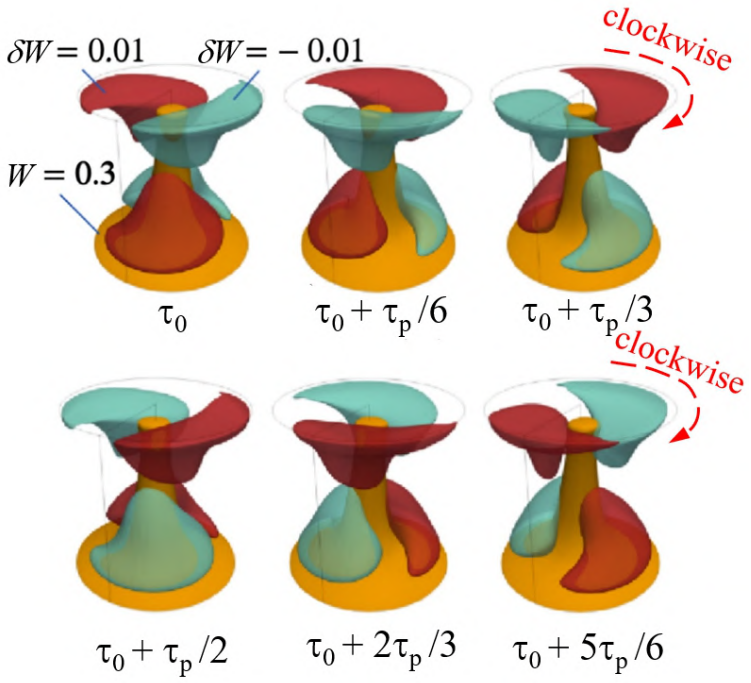

(b) Travelling wave

Figure 4.17 Standing wave (a) and travelling wave (b) inside a cylindrical configuration [100]. The red arrows in the figures indicate the direction of wave propagation. W is Θ or Φ.

With the further increase of Marangoni effect, the pitchfork bifurcation mentioned in the previous section would occur, resulting in the appearance of oscillatory traveling wave shown in Figure 4.16(b) and Figure 4.17(b). On the one hand, the propagation direction highly depends on the configurations. Wherein, as shown in Figure 4.17(b), the traveling wave propagates in the clockwise direction inside a cylindrical configuration, while the oblique oscillation wave appears in the rectangular cavity. On the other hand, the development of flow patterns exhibits different characteristics. Compared with the observation in the rectangular cavity, the wave pattern inside a cylindrical configuration could develop more sufficiently and shows no obvious difference during the propagation process. However, in the cavity, wave pattern undergoes two stages of evolution such as expansion and shrinking during propagation, which is also induced by the effect of cavity wall, as shown in Figure 4.16(b).

CHAPTER 5

THERMAL-SOLUTAL MARANGONI CONVECTION UNDER RADIATIVE HEAT TRANSFER

The interfacial heat transfer is inevitable in industrial processes and has a significant effect on the quality of final products, especially in welding [101] and crystal growth [67]. However, most studies that focused on the thermal-solutal Marangoni flow considered only the case of an adiabatic free surface. The surface heat transfer has not been taken into account. To extend the existing knowledge and gain more insight into the subject, based on our previous work [93], we perform a series of three-dimensional numerical simulations considering the effect of radiative heat transfer on thermal-solutal Marangoni convection in a shallow rectangular cavity with mutually perpendicular thermal and concentration gradients. It is also hoped to shed further light on the related flow characteristics and flow pattern transitions in the cavity.

5.1 The overall flow map

The flow regimes without/with thermal radiation computed at various thermal Marangoni number values are summarized in Figure 5.1. In this figure we present the computed values at the conditions of adiabatic free surface and fixed ambient temperature Θ_{a} (which are -1.5, -1, -0.5, 0, 0.5, 1 and 1.5) along the horizontal axis by varying the thermal Marangoni number Ma_{T} (presented along the vertical axis). It is obvious that, in all cases (without/with radiative heat transfer), the flow pattern always changes from steady to oscillatory and then to chaotic with the increase of the thermal Marangoni number. In addition, oscillatory modes highly depend on the ambient temperature. Three types of oscillatory modes appear at different ambient temperature Θ_{a} values. This will be discussed later in detail.

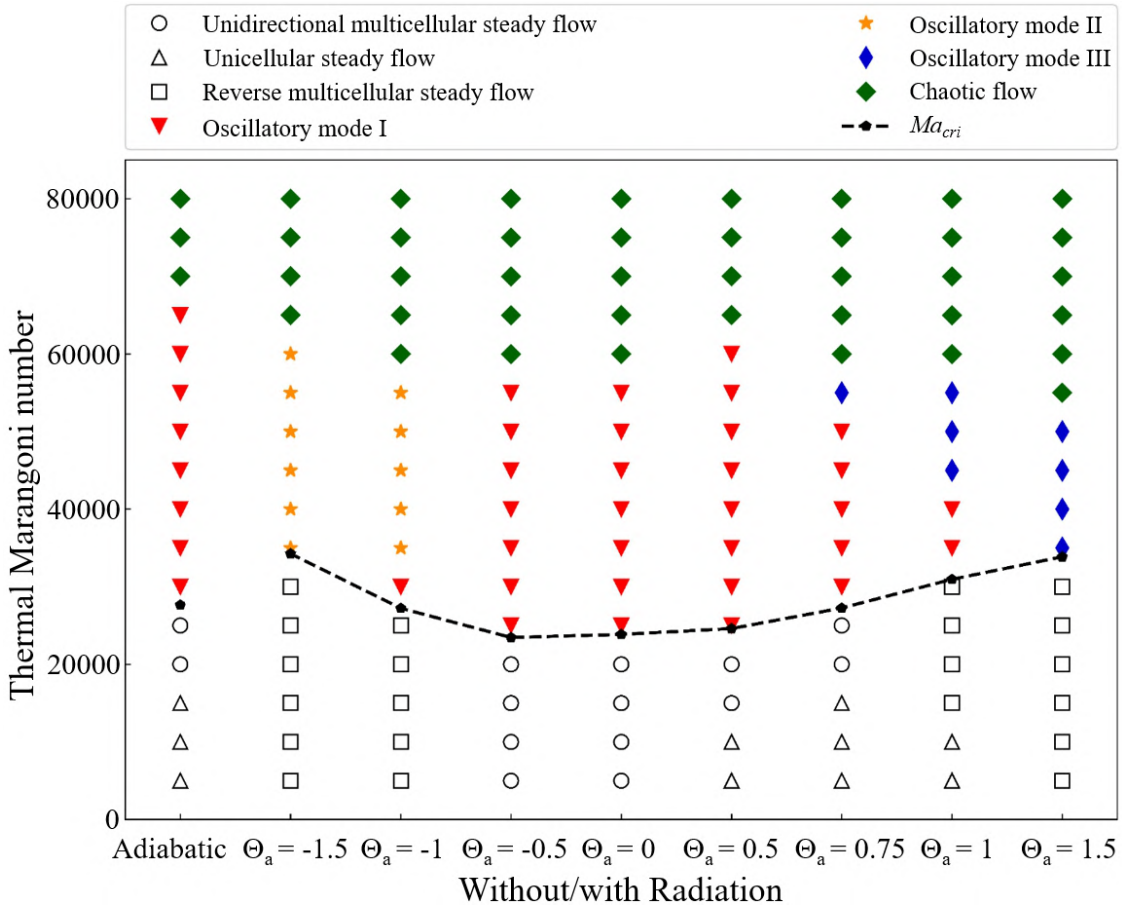

Figure 5.1 The computed flow regimes without/with thermal radiation. The dashed line indicates the critical solutal Marangoni numbers for the corresponding free surface conditions. In all cases, the flow is steady when Ma_{T} is smaller than a critical value and is unstable above this critical value.

5.2 Basic flow pattern

When the Marangoni number is relatively small, the thermal-solutal Marangoni convection is steady, which is called the "basic flow" hereafter. Figure 5.2 presents the computed streamlines, isotherms, and iso-concentration lines of a typical basic flow at $Ma_{\mathrm{T}} = 1 \times 10^4$ at various free surface conditions. Since the overall thermal and solutal Marangoni effects are of equal strengths (Ma_σ = 1), the fluid along the free surface (called here "surface fluid") usually flows diagonally with a flow velocity with the components in the x- and y-directions, and then returns back near the bottom due to the mass conservation since the flow is confined within the cavity, as seen in the streamlines of Figure 5.2. The variations at Θ_{a} = -1.5 and Θ_{a} = 1.5 differ from the others in the local region; namely, in the vicinity of the right ($x = 1$) and left ($x = 0$) sidewalls, respectively. The surface fluid locally flows towards the upper-left direction, as shown as the secondary reverse vortex in Figure 5.3(b) and Figure 5.3(f). This is caused by the movement of maximum and minimum temperature positions from the sidewall to the free surface due to the strong radiative heat transfer, as depicted in Figure 5.2(b) and Figure 5.2(d). The temperature difference is larger than 1 on the free surface.

Since the Prandtl number ($Pr = 0.01$) of the working fluid is far less than unity; the heat transfer in the liquid layer is basically by conduction. The isotherms of the basic flow are almost parallel to the left and right sidewalls, while the iso-concentration lines are much more distorted and sensitive to the flow region due to the equal contribution ($Sc = 1$) of conduction and momentum transfer. It is noted that the ambient temperature has a significant influence on the thermal-solutal Marangoni flow. As shown in Figure 5.2(a)-(d), thermal radiation gives rise to a difference of temperature gradient and thus to a change in the fluid flow that triggers a distortion in the concentration field. The distortion in the concentration in turn affects the distributions of temperature and flow velocity. This coupling mechanism is responsible for the effect of thermal radiation on the thermal-solutal Marangoni flow. Accordingly, as depicted in Figure 5.3, the basic flow appears in three forms of steady flow, namely, unidirectional multicellular flow, unicellular flow, and reverse multicellular flow at different free surface conditions.

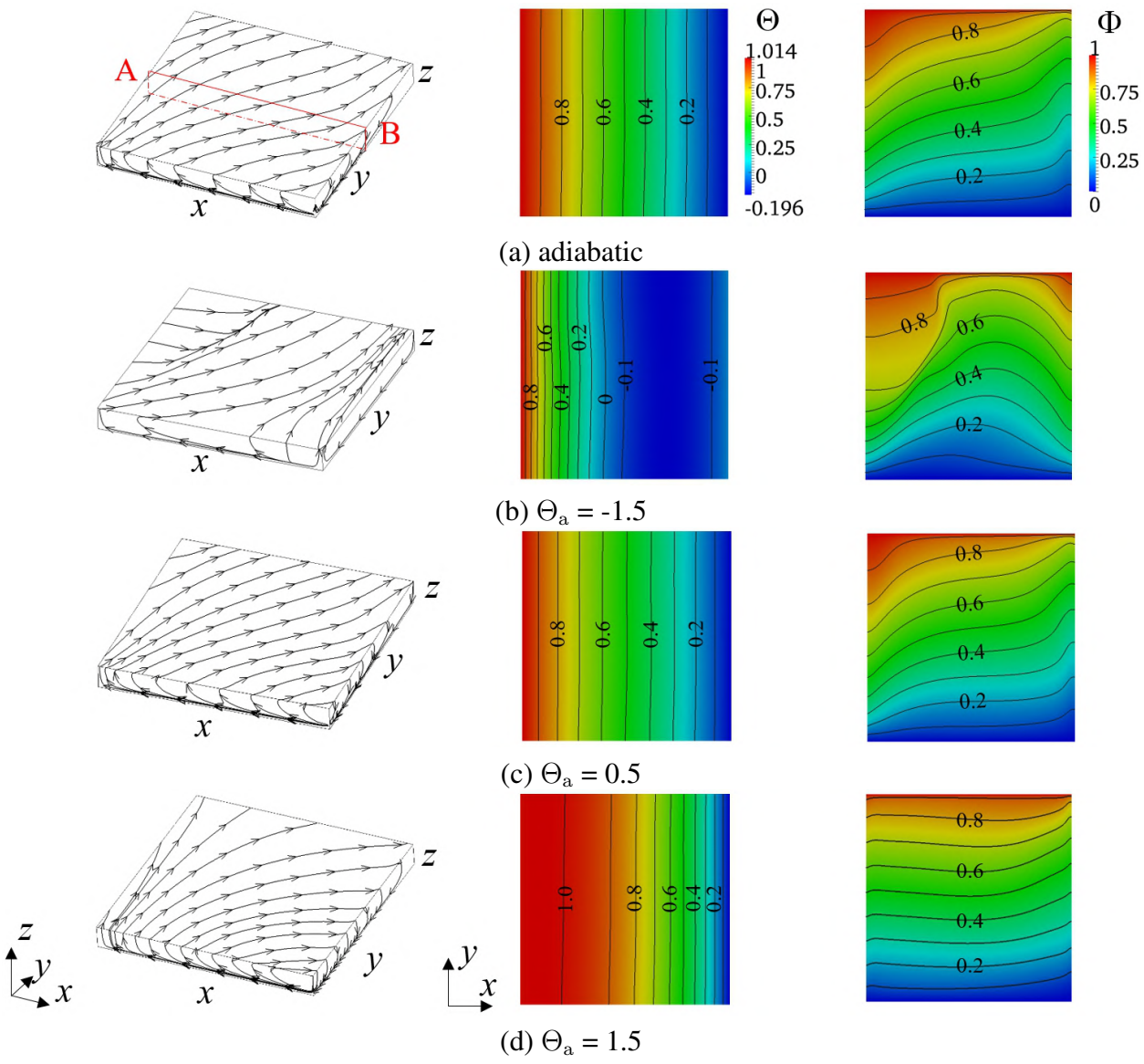

Figure 5.2 Streamlines along the boundaries (left), isotherms (middle) and iso-concentration lines (right) on the top free surface at $Ma_{\mathrm{T}} = 1 \times 10^4$ at different free surface conditions. (a) adiabatic, (b) Θ_{a} = -1.5, (c) Θ_{a} = 0.5, and (d) Θ_{a} = 1.5. The contour values of temperature and concentration are with steps of 0.1.

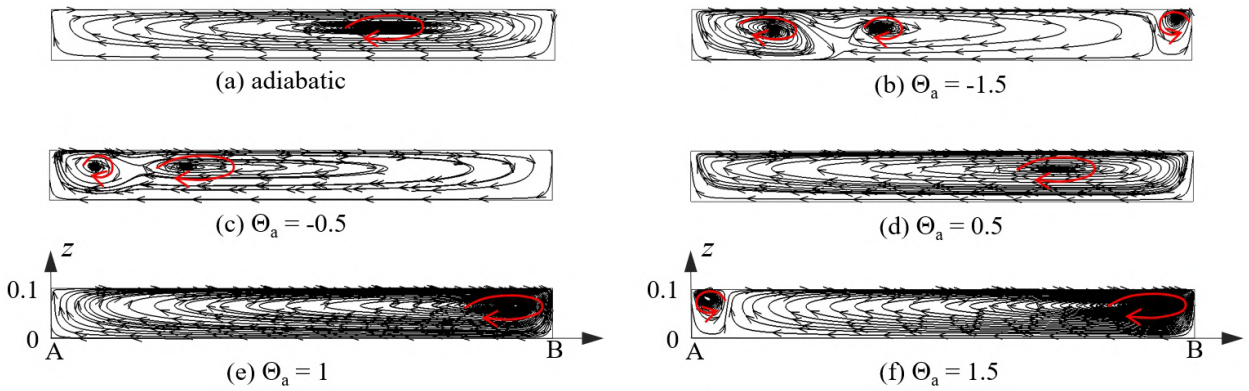

Figure 5.3 Streamlines at the A–B plane ($y = 0.5$) at $Ma_{\mathrm{T}} = 1 \times 10^4$ at different free surface conditions. (a) adiabatic, (b) Θ_{a} = -1.5, (c) Θ_{a} = -0.5, (d) Θ_{a} = 0.5, (e) Θ_{a} = 1, and (f) Θ_{a} = 1.5. The position of A–B plane is shown in Figure 5.2(a).

Figure 5.4 shows the computed distributions of temperature gradient $\mathrm{grad}\Theta_x$ and velocity magnitude V_{mag} along the AB line (y = 0.5) at various free surface conditions. With the increase of ambient temperature, the overall radiative heat transfer on the free surface exhibits transition from heat loss to heat gain. Thus, as shown in Figure 5.4(a), the maximum temperature gradient first decreases then increases, and the positions of that transit from left to right sidewalls. It is noted that, at Θ_{a} = 0.5 (green line), although the temperature gradient close to sidewalls is larger than that of the adiabatic case (orange line), it is contrary at the central region, while the temperature gradient is always approximately -1 under the adiabatic condition. Owing to the coexistence of heat gain and heat loss, the overall radiative heat flux in terms of Θ_{a} = 0.5 is close to 0, as shown in Figure 5.5. Therefore, the similar distributions of streamline, temperature, and concentration overall are observed, which are shown in Figure 5.2(a) and Figure 5.2(c). In addition, as shown in Figure 5.4(b), the distribution of flow velocity magnitude also accordingly changes with the intensity of thermal radiation, which greatly affects the flow structure in the system (see Figure 5.3).

5.3 Critical Marangoni number

The control of flow stability is crucial for the quality of products in applications especially in material welding, glass production, and crystal growth. Thus, the relationships between the thermal radiation and flow stability need to be further investigated. As the thermal Marangoni

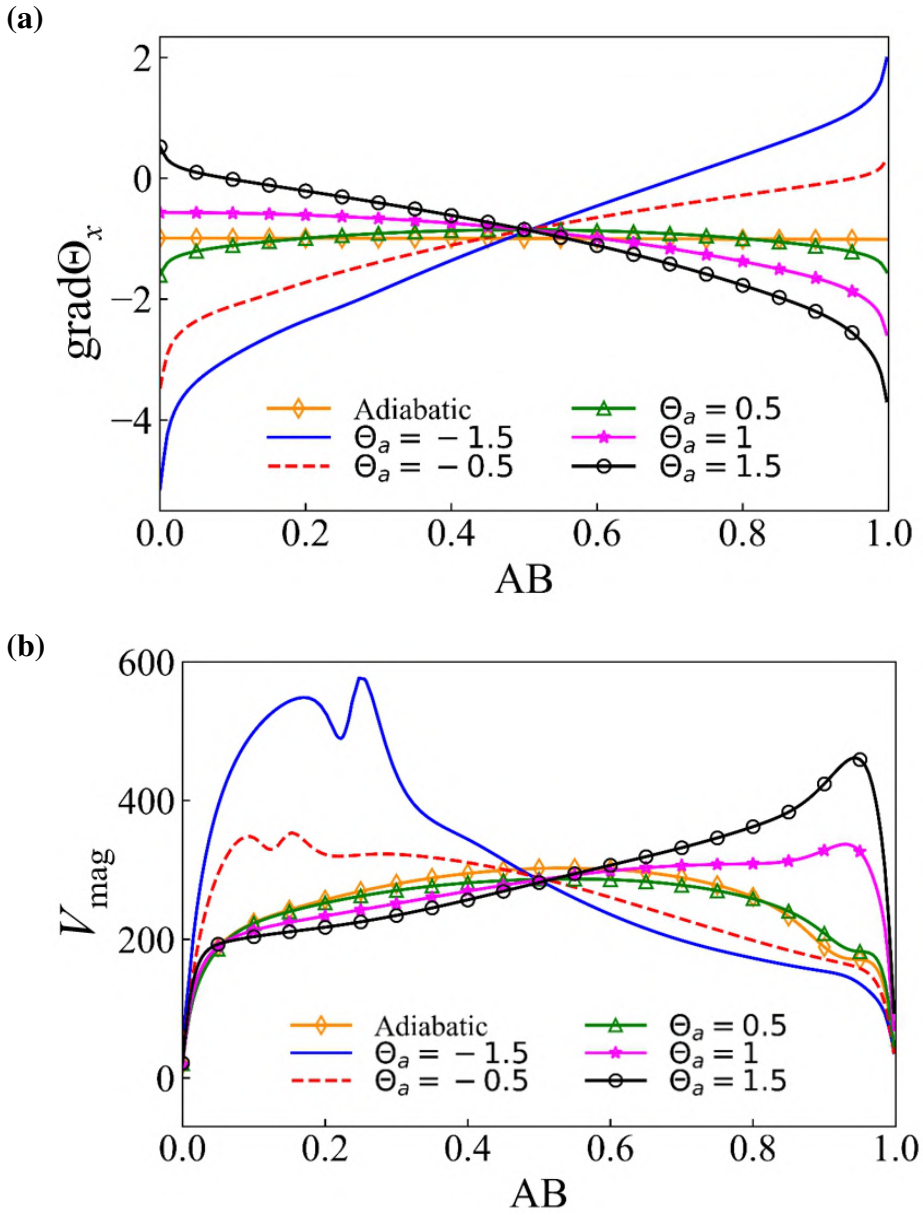

Figure 5.4 Distributions of the temperature gradient $\mathrm{grad}\Theta_x$ (a) and velocity magnitude V_{mag} (b) along AB line on the free surface at $Ma_{\mathrm{T}} = 1 \times 10^4$.

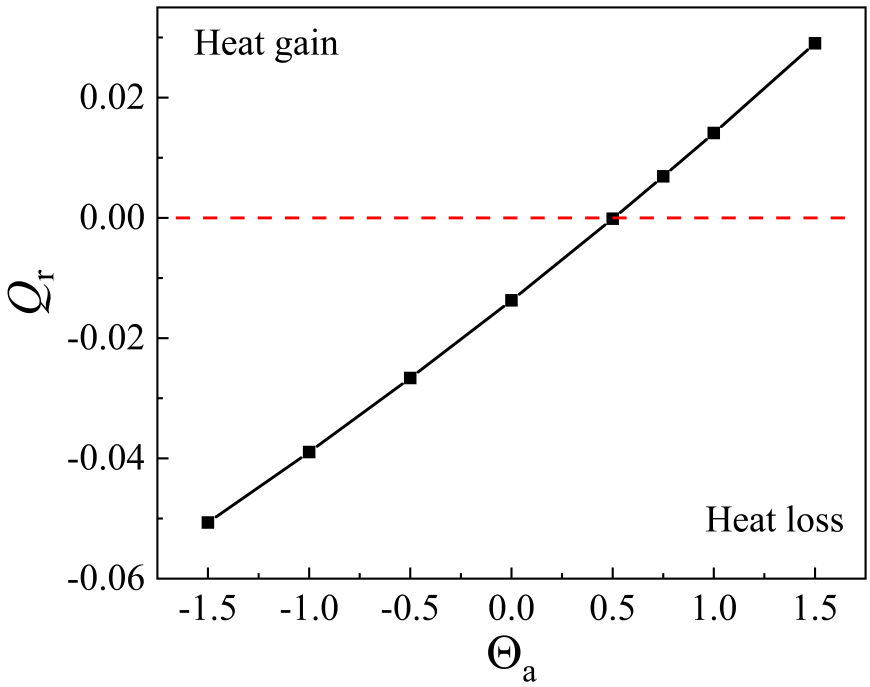

Figure 5.5 Variation of the overall interfacial radiative heat flux with different ambient temperature.

number exceeds a critical value, namely, critical Marangoni number Ma_{cri}, the three-dimensional disturbances begin to gestate and develop. The basic flow may become unsteady and bifurcate into various three-dimensional oscillatory flows.

Dynamic mode decomposition (DMD) is a useful technique to investigate the hydrodynamic processes involved, which was successfully applied to determine the critical condition with the respect to the instability of thermal-solutal Marangoni flow in our previous work [58]. In the DMD method, a temporal sequence of data snapshots from the numerical simulation are represented by a matrix $\boldsymbol{M}_1^N$,

$$\boldsymbol{M}_1^N = \{\boldsymbol{m}_1, \boldsymbol{m}_2, \boldsymbol{m}_3, ..., \boldsymbol{m}_N\} \tag{5.1}$$

where $\boldsymbol{m}_i$ stands for the i-th flow field ($N = 1, 2, 3, ..., N$).

We assume that, in a short constant sampling time, a linear mapping $\boldsymbol{A}$ between a flow field $\boldsymbol{m}_i$ and the subsequent flow field $\boldsymbol{m}_{i+1}$ can be expressed as $\boldsymbol{m}_{i+1} = \boldsymbol{A}\boldsymbol{m}_i$, which is considered as a linear approximation of solving the governing equations. The dynamic characteristics of the

system is given by the eigenvalues and eigenvectors of the matrix $\boldsymbol{A}$. And the corresponding matrix form can be represented as,

$$\boldsymbol{M}_2^N = \boldsymbol{A}\boldsymbol{M}_1^{N-1} + \boldsymbol{r}\boldsymbol{e}_{N-1}^T \tag{5.2}$$

where $\boldsymbol{r}$ denotes the residual vector and $\boldsymbol{e}_{N-1} \in \mathbb{R}^{N-1}$ applies as the $(N-1)$ unit vector. Substituting the singular value decomposition ($\boldsymbol{M}_1^{N-1} = \boldsymbol{U}\boldsymbol{\Sigma}\boldsymbol{W}^H$) into above equation, then

$$\boldsymbol{U}^H\boldsymbol{A}\boldsymbol{U} = \boldsymbol{U}^H\boldsymbol{M}_2^N\boldsymbol{W}\boldsymbol{\Sigma}^{-1} \equiv \tilde{\boldsymbol{A}} \tag{5.3}$$

with the matrix $\boldsymbol{U}$ contains the proper orthogonal modes of $\boldsymbol{M}_1^{N-1}$. As $\boldsymbol{A}$ related to $\tilde{\boldsymbol{A}}$ by a similarity transformation, the dynamic modes κ_i can be expressed as follow,

$$\kappa_i = \boldsymbol{U}\boldsymbol{y}_i \tag{5.4}$$

where $\boldsymbol{y}_i$ is the i-th eigenvector of $\tilde{\boldsymbol{A}}$, i.e. $\tilde{\boldsymbol{A}}\boldsymbol{y}_i = \mu_i\boldsymbol{y}_i$. In consequence, the corresponding eigenvalues λ, which present the stability of extracted dynamic oscillatory mode, is obtained by the logarithmic transform of μ_i. The real part of the eigenvalues, λ_r, determines the growth/decay rate: unstable, λ_r ¿ 0; neutral, λ_r = 0; stable, λ_r ¡ 0. And the imaginary part, λ_i represents the frequency of the mode.

Table 5.1 The non-dimensional frequencies of disturbances obtained by DMD and simulation.

Θ_a	Ma_T	F	
		DMD	Simulation
-0.5	2.35×10^4	191.80	191.21
0.5	2.47×10^4	226.19	226.27
0.5	2.5×10^4	226.87	226.88
0.5	2.6×10^4	228.88	228.89
1	3.1×10^4	284.19	284.17
1.5	3.4×10^4	86.13	86.12

Figure 5.6 shows an example of the eigenvalue spectrum at Θ_a = 0.5 obtained by DMD method near the onset of thermal-solutal Marangoni convection. At $Ma_\mathrm{T} = 2.47 \times 10^4$, as shown in the inset of Figure 5.6, the real part of the leading eigenvalue ($\lambda = \lambda_r + \lambda_i = 0.00098 \pm 1.99\mathrm{i}$) is larger than zero, which indicates the unstable oscillatory mode appears. However, the flow remains steady

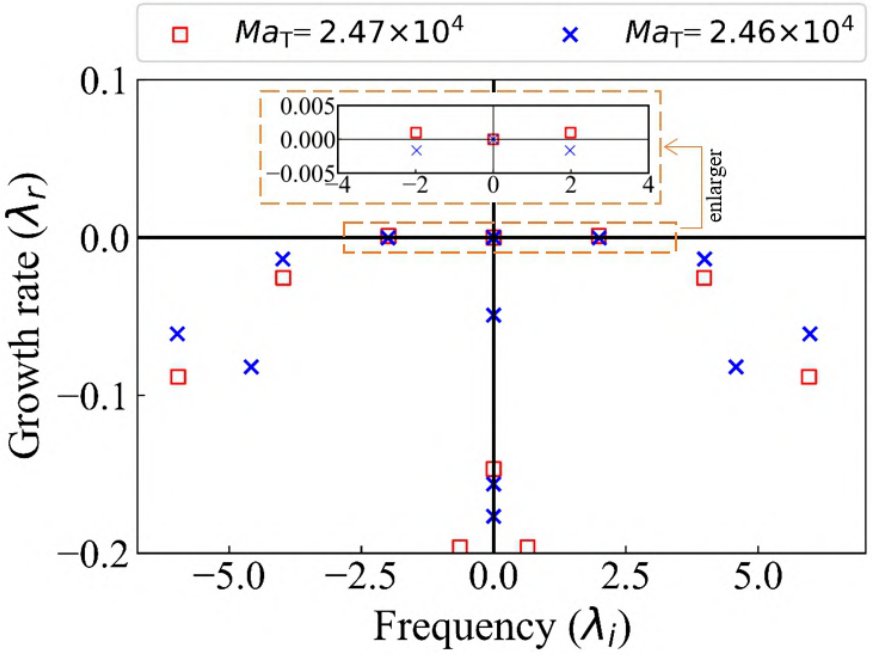

Figure 5.6 Eigenvalue spectrum of thermal-solutal Marangoni convection onset at Θ_a = 0.5.

at $Ma_T = 2.46 \times 10^4$ due to the negative growth rate λ_r. Thus, the critical Marangoni number is calculated as $Ma_{cri} = 2.465 \times 10^4 \pm 0.2\%$. In addition, as summarized in Table 5.1, the predicted frequencies from DMD are in good agreement with those of simulation.

The critical Marangoni number values at various free surface conditions are given in Figure 5.1 (the dashed line). In the case of heat loss, at -0.5 $\leq \Theta_a <$ 0.5, with the increase of ambient temperature, the amount of heat loss decreases, and the maximum temperature gradient on the free surface becomes smaller. Thus the critical Marangoni number Ma_{cri} slightly increases due to the weakened flow velocity intensity. At $\Theta_a <$ -0.5, the reverse multicellular flow appears and the primary flow region becomes small. Therefore, although the flow intensity would still increase, the effective aspect ratio becomes larger, resulting in the larger Ma_{cri}, which is in good agreement with those earlier predictions made for the relationship of aspect ratio and critical Marangoni number [33, 71]. Zhang *et al.* [102] reported that for the pure thermal Marangoni flow in an annular pool, the critical Marangoni number of flow destabilization becomes larger at strong heat loss conditions, while that value is basically unchanged in the case of weak heat loss. In the case of heat gain ($\Theta_a >$

0.5), the maximum thermal gradient moves from left to the right sidewall and interacts directly with solutal Marangoni effect near the upper-right corner, leading to the appearance of a suppressing effect between thermal and solutal Marangoni flows to some extend. On the other hand, analogous to the case of large heat loss, a secondary reverse flow appears, and the effective aspect ratio increases. Hence, Ma_{cri} gradually increases at the higher Θ_{a} values. Furthermore, a Ma_{cri} higher than that of Θ_{a} = 0.5 is observed in the adiabatic case.

5.4 Effect of radiative heat transfer on flow pattern

When the Marangoni number exceeds the critical value Ma_{cri}, the stability of the Marangoni flow gets lost, and a three-dimensional oscillatory flow develops. In order to quantitatively investigate the three-dimensional disturbances, a fluctuation quantity (δW) over one period is introduced as,

$$\delta W(x,y,z,\tau) = W(x,y,z,\tau) - \frac{1}{\tau_p}\int_{\tau_0}^{\tau_0+\tau_p} W(x,y,z,\tau)d\tau \tag{5.5}$$

where W can be Θ or Φ.

5.4.1 No heat flux ($Q_{\mathrm{r}} \approx 0$)

In the case of pure thermal Marangoni flow, as predicted by Smith and Davis [13], the hydrothermal wave (HTW) propagates from the low temperature sidewall to the high temperature sidewall at a certain angle of φ_{T} with respect to the horizontal temperature gradient. This prediction is observed in subsequent experimental observations [103–105] and numerical simulations [29, 106], as shown in Figure 5.7(a). Analogous to the HTW, in the case of pure solutal Marangoni flow, the hydrosolutal wave (HSW) due to the inverse surface tension coefficient ($\sigma_{\mathrm{C}} > 0$) would propagate from the high concentration sidewall to the low concentration sidewall at a certain angle of φ_{C} with respect to the horizontal concentration gradient, as shown in Figure 5.7(b).

In the present work, we consider the cases where both the thermal and solutal Marangoni effects are present. Figure 5.8 shows the computed snapshots of surface temperature and concentration fluctuations and their corresponding space-time diagram (STD), which consists of a series

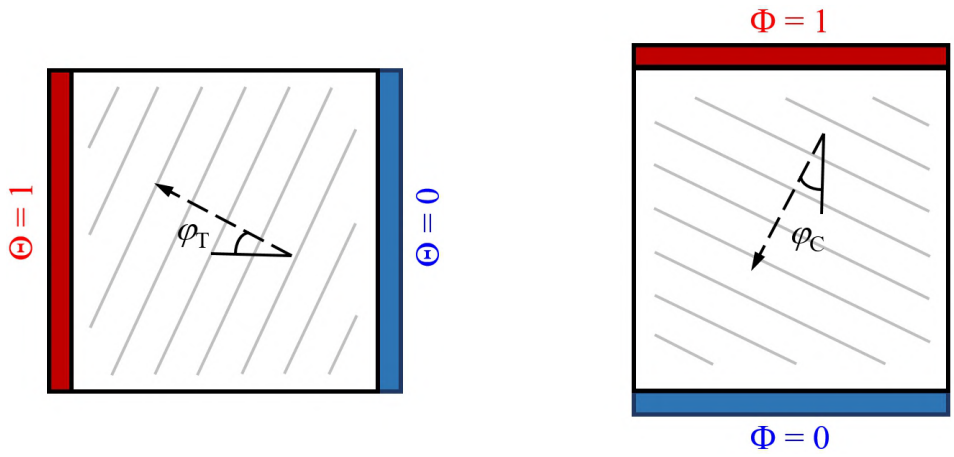

(a) HTW (b) HSW

Figure 5.7 The schematic drawing of propagation direction associated with HTW (a) and HSW (b) in the pure thermal Marangoni flow and pure solutal Marangoni flow. The dash arrow indicates the direction of the wave propagation.

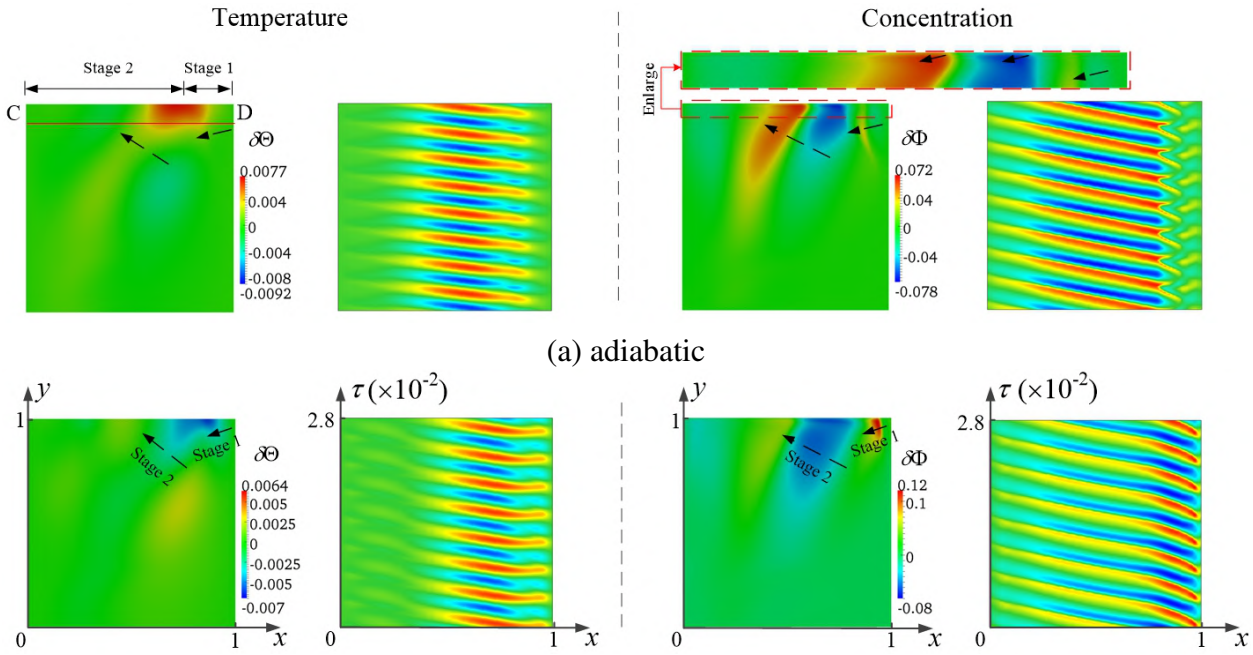

Figure 5.8 Snapshots of the surface temperature (left) and concentration (right) fluctuations and the corresponding space-time diagram (STD) at the CD line ($y = 0.9$) at $Ma_T = 4 \times 10^4$. (a) adiabatic, and (b) $\Theta_a = 0.5$. The arrows in HTW and HSW indicate the directions of wave propagation. In addition, the dimensionless time τ for all STDs is 0.028, and the position of the CD line is shown in Figure 5.8(a).

of parallel stripes, at $Ma_{\mathrm{T}} = 4 \times 10^4$. It is evident that the flow instabilities are observed on the free surface in the forms of HTW and HSW. Meanwhile, for both wave forms, the thermal and solutal Marangoni flows are of equal strengths (Marangoni ratio Ma_σ = 1). Thus, two different propagation directions of wave pattern always coexist at the same time. This is in good agreement with the results of our previous study [93].

In the case of an adiabatic free surface assumption, as shown in Figure 5.8(a), the wave patterns of HTW and HSW propagate from the upper-right corner towards the lower-left corner first (Stage 1), and then to the upper-left corner (Stage 2), which is called the "oscillatory mode I" hereafter. This phenomenon occurs because the thermal and solutal Marangoni effects have comparable contributions locally. During Stage 1, as also shown in Figure 5.2, the dense iso-concentration lines are observed in the vicinity of upper-right corner, the solutal Marangoni effect is dominant, resulting in the lower-left propagation direction, which is consistent with the prediction made in the case of pure Marangoni flow shown in Figure 5.7(b). On the contrary, the thermal Marangoni flow plays a prominent role during Stage 2, thus the wave propagates towards the upper-left corner. It should be pointed out that the wave propagation in the lower-left direction appears in the narrow region of the back sidewall ($y = 1$) due to the strong solutal Marangoni effect. When Θ_{a} = 0.5, as shown in Figure 5.8(b), a similar flow pattern is observed. Compared with the adiabatic case, the intensity of the thermal Marangoni effect near the right sidewall ($x = 1$) becomes slightly stronger (see Figure 5.4(a)), thus the propagation distance of Stage 1 is smaller, as shown in the STD of Figure 5.8(b).

5.4.2 Heat loss ($Q_{\mathrm{r}} < 0$)

When $\Theta_{\mathrm{a}} < 0.5$, heat loss occurs on the free surface. The maximum temperature gradient would be observed close to the left sidewall ($x = 0$) due to the effect of radiative heat transfer. Figure 5.9 shows the computed snapshots of the surface temperature and concentration fluctuations and their corresponding space-time diagram at $Ma_{\mathrm{T}} = 4\times10^4$ at two different ambient temperature values; namely, Θ_{a} = 0 and -1. It is obvious that in both cases, due to the physical properties of the

working fluid ($Pr = 0.01, Sc = 1$), the patterns of HTW and HSW would be different, while the directions of wave propagation are basically the same. Therein, the propagation process of HTW is not notable during Stage 1 due to the weak thermal Marangoni effect, but the upper-left oblique stripes could be found in the corresponding STD.

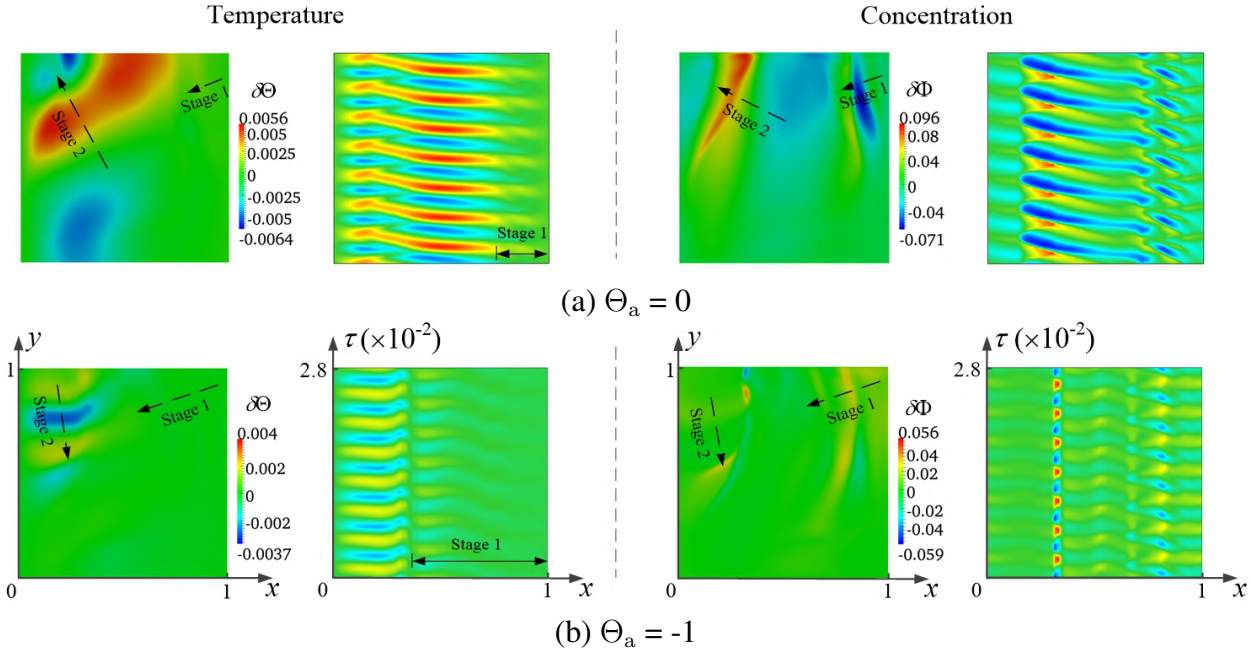

Figure 5.9 Snapshots of the surface temperature (left) and concentration (right) fluctuations and the corresponding space-time diagram (STD) at the CD line ($y = 0.9$) at $Ma_{\mathrm{T}} = 4 \times 10^4$. (a) Θ_{a} = 0, and (b) Θ_{a} = -1. The dimensionless time τ for all STDs is 0.028, and the position of the CD line is shown in Figure 5.8(a).

At Θ_{a} = 0, the amount of heat loss through the free surface is small, the wave patterns in the forms of HTW and HSW are similar at Θ_{a} = 0.5, while the propagation distance of Stage 1 increases and the position of maximum temperature fluctuation on the free surface close towards the left sidewall, as shown in the STD of Figure 5.9(a). As the intensity of heat loss becomes larger, i.e., at Θ_{a} = -1, as shown in Figure 5.9(b), the associated wave pattern exhibits another type of oscillatory mode (mode II), which propagates towards the lower-right corner during Stage 2. As shown in Figure 5.10, the value of the concentration gradient ($\mathrm{grad}\Phi_{\mathrm{mag}}$) along the CD line ($y = 0.9$) varies widely and is larger than the temperature gradient ($\mathrm{grad}\Theta_{\mathrm{mag}}$) in the most region ($0.3 < x < 1.0$), resulting in the further increase of the propagation distance during Stage 1, while

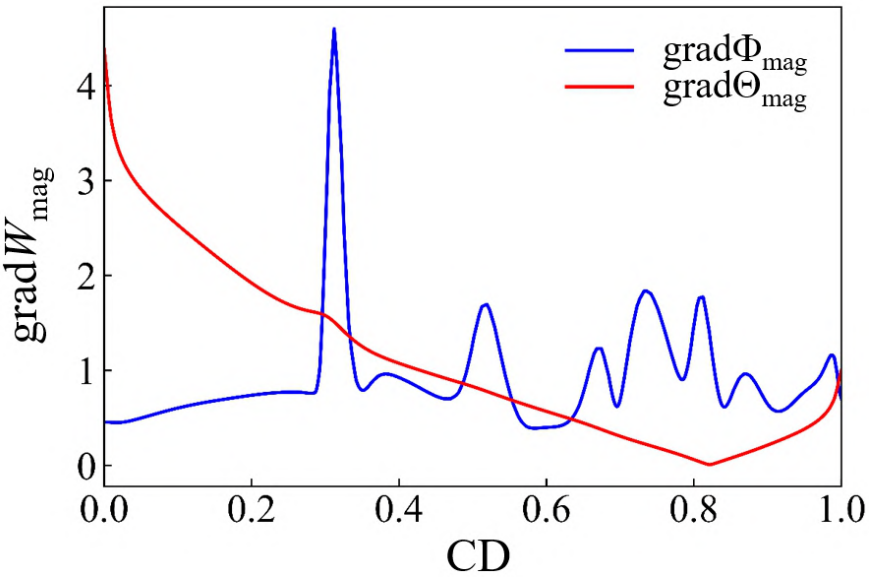

Figure 5.10 Distributions of the temperature and concentration gradients along $y = 0.9$ (the CD line in Figure 5.8) on the free surface at $Ma_{\mathrm{T}} = 4 \times 10^4$ at Θ_{a} = -1. W is Θ or Φ.

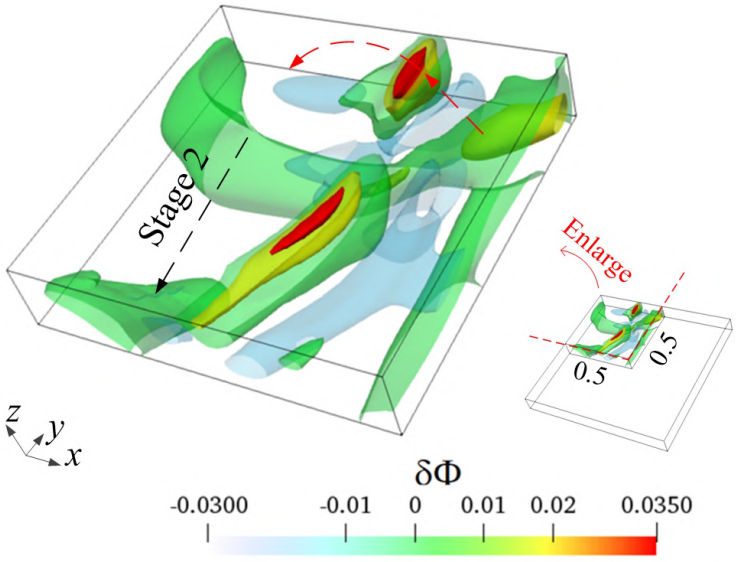

Figure 5.11 Isosurfaces of 3D concentration fluctuations at $Ma_{\mathrm{T}} = 4 \times 10^4$ at Θ_{a} = -1. The red arrow represents the process of impinging the sidewall.

the wave pattern associated with the thermal Marangoni effect in Stage 2 suddenly propagates towards the lower-right corner. Figure 5.11 presents the snapshots of the concentration fluctuation at $Ma_{\mathrm{T}} = 4 \times 10^4$ within the upper-left part ($0 \leq x \leq 0.5, 0.5 \leq y \leq 1$) of the rectangular cavity. Due to the effect of the cavity walls, after the wave instabilities impinge the sidewall along the upper-right direction, the reversed propagation direction at the lower-right corner would appear finally. A similar phenomenon with respect to the effect of the cavity walls on the propagation direction was also illustrated in previous studies in the case of pure thermal Marangoni convection [29, 105].

5.4.3 Heat gain ($Q_{\mathrm{r}} > 0$)

When $\Theta_{\mathrm{a}} > 0.5$, heat gain occurs on the free surface, and the maximum temperature gradient would move towards the right sidewall ($x = 1$) due to the effect of radiative heat transfer. Figure 5.12 shows the computed snapshots of surface temperature and concentration fluctuations and their corresponding space-time diagram at $Ma_{\mathrm{T}} = 4 \times 10^4$ at three different ambient temperature values; namely, Θ_{a} = 0.75, 1, and 1.5. When the heat gain is small, as shown in Figure 5.12(a), the associated result is similar to the case of Θ_{a} = 0.5, while the propagation region of Stage 1 becomes smaller. In addition, the wave pattern would change from the oblique wave to the straight wave during the propagation process of Stage 2, as shown in Figure 5.13(a). This should be attributed to the comparable contributions of the thermal and solutal Marangoni effects in the local region shown in Figure 5.14, the difference between temperature and concentration gradient values gradually decreases along the negative x direction and finally becomes approximately 0 at x ¡ 0.4.

When we have heat gain again, i.e. at Θ_{a} = 1, the temperature gradient increases near the right sidewall ($x = 1$) but decreases near the left sidewall ($x = 0$). Therefore, the region of Stage 1 further decreases, and the new Stage 3 appears with the propagation direction towards the lower-left corner due to the dominant solutal Marangoni effect, as shown in Figure 5.13(b). With the further increase of heat gain, at Θ_{a} = 1.5 shown in Figure 5.12(c), the thermal Marangoni flow is confined at the right part of the rectangular cavity, resulting in the more complicated coupling effects of

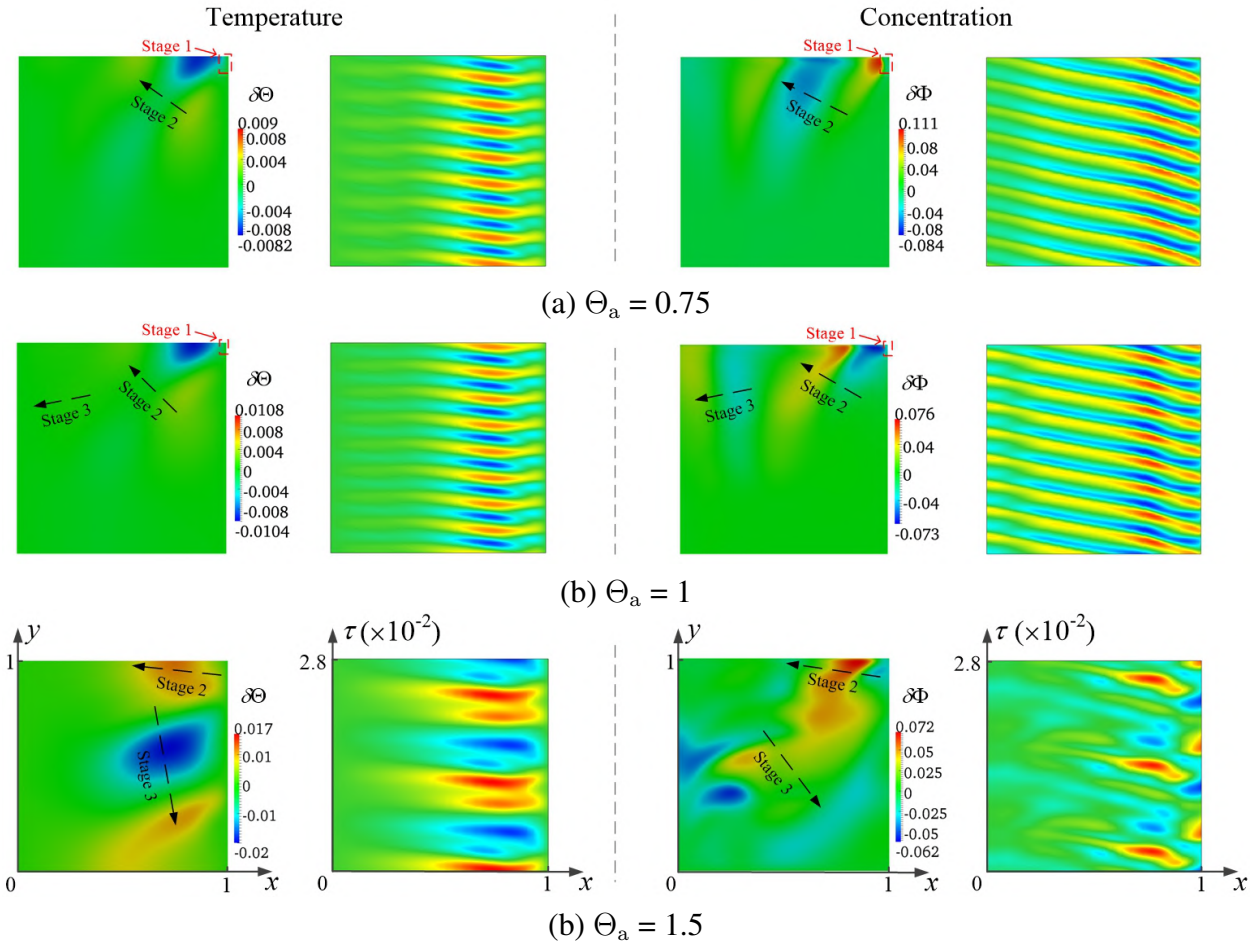

(a) Θ_a = 0.75

(b) Θ_a = 1

(b) Θ_a = 1.5

Figure 5.12 Snapshots of the surface temperature (left) and concentration (right) fluctuations and the corresponding space-time diagram (STD) at the CD line ($y = 0.9$) at $Ma_T = 4 \times 10^4$. (a) Θ_a = 0.75, (b) Θ_a = 1, and (c) Θ_a = 1.5. The dimensionless time τ for all STDs is 0.028, and the position of the CD line is shown in Figure 5.8(a).

thermal and solutal Marangoni flows. The oscillation period would become larger, meanwhile the strips in the STD are more complex. The wave pattern changes from oscillatory mode I to a new oscillatory mode III, which typically propagates towards the upper-left corner first, and then to the lower-right corner. As shown in Figure 5.13(c), Stage 1 starts to disappear and the transition of propagation direction during the stage 3 appears due to the effect of the cavity wall, which is analogous to the results described in the previous subsection.

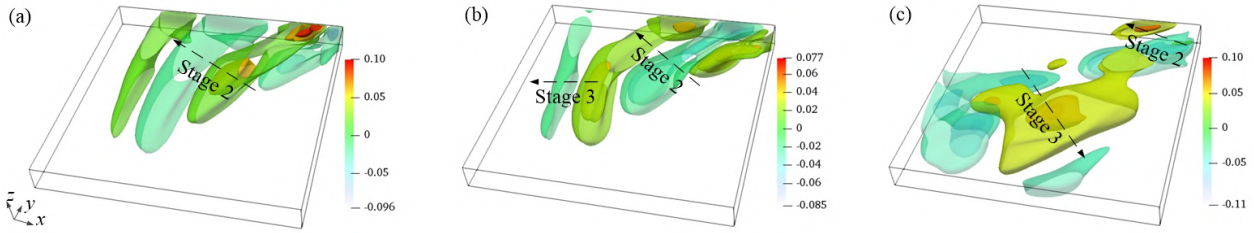

Figure 5.13 Isosurfaces of 3D concentration fluctuations at $Ma_{\mathrm{T}} = 4 \times 10^4$. (a) Θ_{a} = 0.75, (b) Θ_{a} = 1, and (c) Θ_{a} = 1.5.

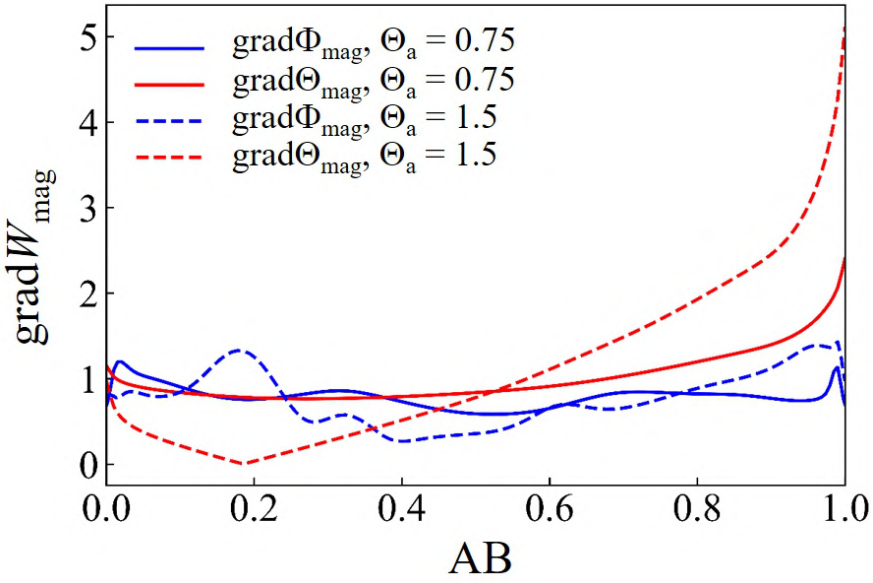

Figure 5.14 Distributions of the temperature and concentration gradients along $y = 0.5$ (the AB line in Figure 5.2) on the free surface at $Ma_{\mathrm{T}} = 4 \times 10^4$ at Θ_{a} = 0.75 and 1.5. W is Θ or Φ.

5.5 Characteristics of the thermal-solutal Marangoni oscillatory flow

The coupling effect of the thermal-solutal Marangoni flow and the radiative heat transfer has a significant influence on the characteristics of oscillatory flow. Figure 5.15 shows the time dependencies of temperature, concentration, and longitudinal velocity at the monitoring point (P) at (x, y, z) = (0.5, 0.5, 0.1) and the associated frequency spectra at $Ma_{\mathrm{T}} = 4 \times 10^4$ at different ambient temperatures. It is clearly shown that there is a constant phase difference between the velocity, temperature, and concentration oscillations. The phase lag phenomenon is the basic characteristic of flow instabilities and would result in the occurrence of HTW and HSW on the free surface (see Figure 5.8). Similar observations have been reported not only in the case of pure Marangoni flow [18, 40] but also in the case of thermal-solutal Marangoni flow [57, 95] with an adiabatic free surface assumption.

The sequence and difference of the phase lag depend on the intensity of thermal radiation. In the case of Θ_{a} = -0.5, as shown in Figure 5.15(a), the velocity oscillation is behind the temperature and concentration oscillations in the time phase, while the contrary sequence is observed at Θ_{a} = 1.5. In addition, the same frequencies are obtained in the frequency spectra as shown in Figure 5.15(a), and there are three main peaks with the values of F_1 = 255.1 and $F_2 = 2F_3/3 = 2F_1$. Therein, F_1 is the dimensionless fundamental frequency, F_2 and F_3 are the harmonics frequencies. However, at higher Θ_{a}, the maximum temperature gradient is close to the right sidewall, and the interactive effect of thermal and solutal Marangoni flows becomes stronger. This results in more complicated frequency spectra and a smaller fundamental frequency, as shown in Figure 5.15(b).

Figure 5.16 shows the variation of frequency value with the thermal Marangoni number at different free surface conditions. It can be seen that the frequency value with respect to the adiabatic case almost coincide with the result of Θ_{a} = 0.5 at a small thermal Marangoni number, and the difference of that becomes larger at a higher thermal Marangoni number due to the enhanced radiative heat transfer. In addition, with the increase of Marangoni number, the 3D disturbance gets stronger, as shown in Figure 5.17. The transition from the oscillatory flow to the quasi-oscillatory flow occurs, and it results in the occurrence of a sudden drop in the frequency, while there are

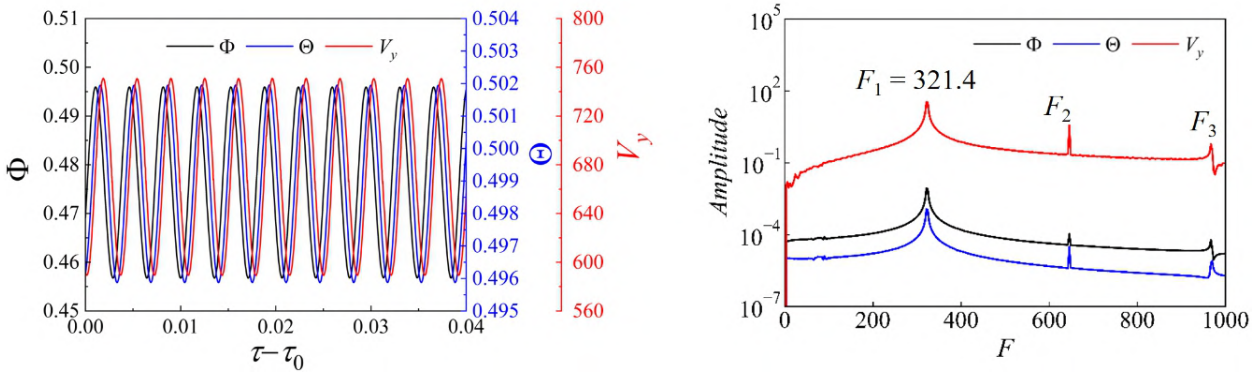

(a) $\Theta_a = 0.5$

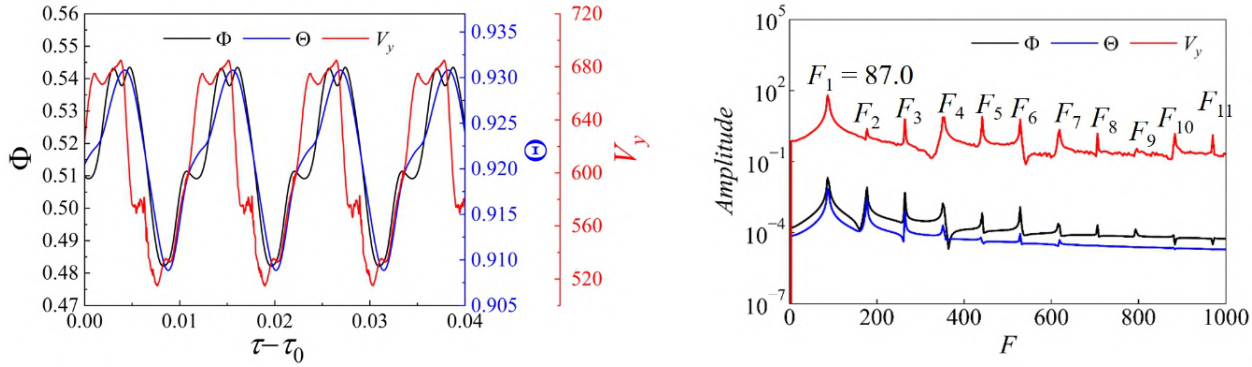

(b) $\Theta_a = 1.5$

Figure 5.15 Time variations of temperature Θ, concentration Φ, and the longitudinal velocity V_y at the sampling point P (left) and their frequency spectra (right) at $Ma_T = 4 \times 10^4$. (a) Θ_a = 0.5, and (b) Θ_a = 1.5.

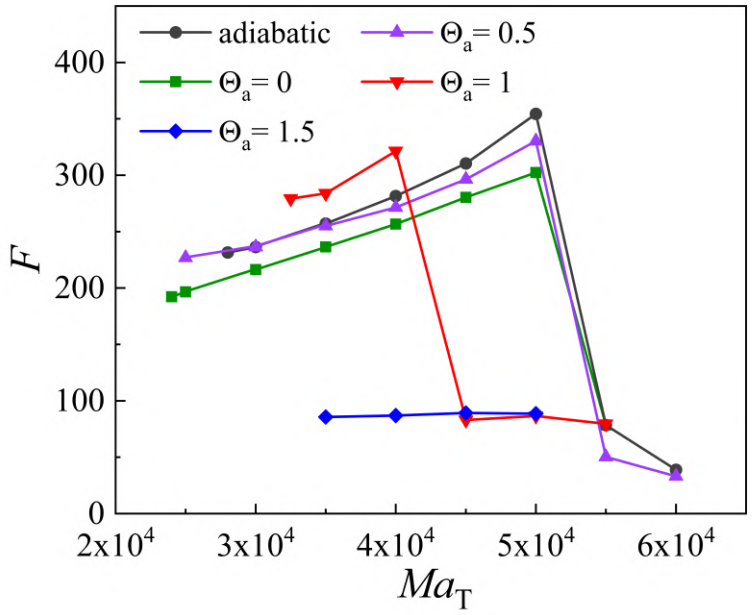

Figure 5.16 Variation of the oscillation frequency F with the thermal Marangoni number Ma_{T} for different free surface conditions at the sampling point P.

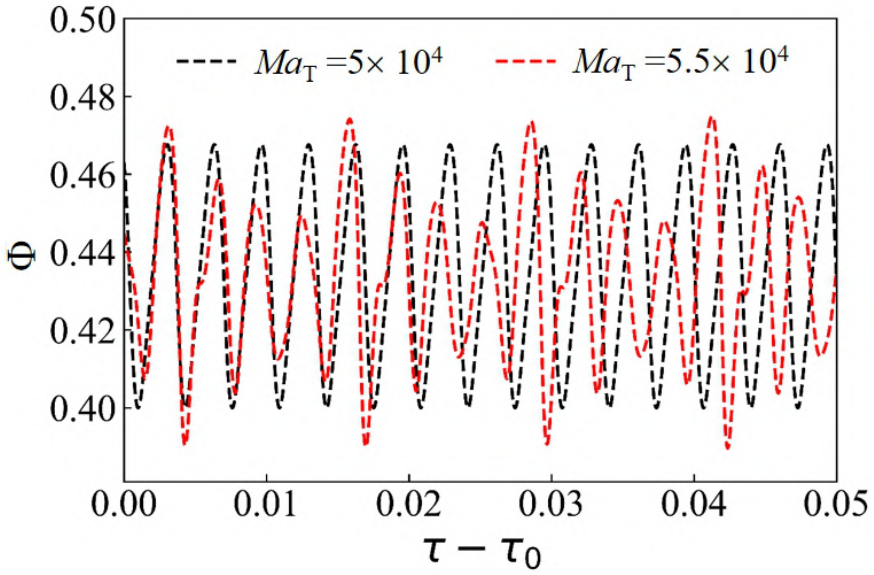

Figure 5.17 Time dependency of the concentration Φ at various thermal Marangoni numbers Ma_{T} at the sampling point P at $\Theta_{\mathrm{a}} = 0$.

no notable variations for Θ_a = 1.5. Note that in Figure 5.16 the frequency drop at Θ_a = 1 is also accompanied by the transition of wave pattern from oscillatory mode I to oscillatory mode III (see flow map in Figure 5.1).

CHAPTER 6

CONCLUSIONS AND FUTURE PERSPECTIVES

6.1 Pure Marangoni convection with a linear solutal boundary condition

This work deals with the characterstics of Marangoni convection developing in a rectangular cavity subjected to a linear solutal boundary condition. A series of three-dimensional simulations are performed with two Schmidt number values (moderate and high) ($Sc = 10$ and 100). The results exhibit some unique characteristics compared with those of previous studies based on a constant boundary condition. The following conclusions are drawn from the present study:

(1) At a relatively small solutal Marangoni number, the basic flow is steady, and the flow structures remain symmetric along the diagonals of the domain. Small secondary vortices are embedded into the liquid layer, which has a significant influence on the concentration distribution. Also, the number of secondary vortices depends on the levels of the solutal Marangoni and the Schmidt numbers.

(2) Comparing with the oscillatory flows develop using CBC (constant boundary condition), one can see that the disturbance energy is considerably less at all levels of Ma_{C} values considered, although a backward transition from chaotic to oscillatory is observed with the use of LBC (linear boundary condition) for a moderate Schmidt number at $Ma_{\mathrm{C}} = 3 \times 10^4$. In addition, the concentration distribution displays more uniformity on the bottom surface.

(3) At higher solutal Marangoni number values, the steady flow evolves into three types of oscillatory flows, namely, SW1 (symmetric along diagonals AB and CD), RW (rotating wave), and SW2 (symmetric only along diagonal AB) at a moderate Schmidt number. However, in the case of a higher Schmidt number, the flow bifurcates orderly to SW1, then to SW3 (symmetric only along diagonal CD), and finally to SW2. It is worth noting that the RW does not appear during the flow evolution, resulting from the coupling effect of the dominant and secondary waves.

(4) The concentration fluctuations usually first appear in the liquid layer due to the sudden change in flow direction. In addition, at the higher solutal Marangoni number values, due to the effect of cavity walls, the wave patterns undergo expansion, separation, squeezing, and merging during propagation, resulting in the occurrence of patterns in the forms of spline-like, horseshoe-like, and wedge-like.

The simulation results show that the Marangoni convection developing in a rectangular cavity, that is subjected to a liner solutal boundary condition, exhibits more complex flow and concentration characteristics compared to the findings of previous studies in similar systems that were subjected to a constant boundary condition. This shows that the selection of a concentration boundary condition needs further studying in order to gain a deeper understanding of the role of Marangoni convection in industrial processes such as painting and drying.

6.2 Thermal-solutal Marangoni convection with mutually perpendicular temperature and concentration gradients

Numerical simulations are carried out to investigate the thermal-solutal Marangoni convection that is subjected to mutually perpendicular temperature and concentration gradients. Basing on the simulation results, the main conclusions are drawn:

(1) At the relatively small solutal Marangoni number, solutal Marangoni convection is greatly affected by the thermal Marangoni effect. The basic flow evolves into three types of steady flows, namely a longitudinal surface flow, an oblique stripe flow, and a lateral surface flow, at the higher thermal Marangoni number values.

(2) With the increase of thermal Marangoni number, the critical solutal Marangoni number firstly increases and then decreases due to the change of relative contributions of the thermal and solutal Marangoni effect, as shown in Figure 4.1.

(3) Once the flow becomes unstable, the concentration fluctuation on the free surface is similar to the temperature fluctuation. The propagation directions of wave patterns depend on the coupling thermal–solutal Marangoni effect. Also, a backward transition from chaotic to

oscillatory is encountered at $Ma_{\mathrm{T}} = 3 \times 10^4$. The Marangoni flow becomes completely chaotic at higher solutal Marangoni number values.

(4) Oscillatory standing wave and traveling wave are observed not only in the rectangular cavity but also in the cylindrical configurations. However, owing to the effect of cavity wall, the flow pattern in a cylindrical configuration could develop more sufficiently and shows different characteristics.

Thermal-solutal Marangoni convection developing in a rectangular cavity that is subjected to mutual perpendicular temperature and concentration gradients have shown significant difference from the findings of previous studies in similar setups that were subjected to mutual parallel thermal and concentration gradients. Results show that the relationship between the directions of imposed temperature and concentration gradients needs to be further examined for a deeper understanding of the subject.

6.3 Thermal-solutal Marangoni convection under radiative heat transfer

A series of three-dimensional simulations under the effect of radiative heat transfer have been carried out on the thermal-solutal Marangoni convection in a rectangular cavity that is subjected to mutually perpendicular temperature and concentration gradients. The following conclusions are obtained from the analysis.

(1) For the basic flow, with the increase of ambient temperature, the maximum temperature gradient first decreases then increases, and the positions of that transit from the left to right sidewalls, which in turn greatly affects the concentration and velocity fields in the whole system.

(2) Radiative heat transfer has significant influence on the stability of thermal-solutal Marangoni convection. With the transition from heat loss to heat gain, the critical Marangoni number first decreases and then increases due to the coupling effects of the thermal radiation and thermal-solutal Marangoni flow.

(3) Once the flow destabilizes, the fluctuations of temperature and concentration are observed on the free surface in the forms of hydrothermal wave and hydrosolutal wave. Two different propagation directions of wave patterns coexist on the free surface due to the equal overall contributions of thermal and solutal effects, while the associated directions of wave propagation highly depend on the intensity of radiative heat transfer. Furthermore, a frequency drop suddenly appears at a higher thermal Marangoni number due to the more complex interactive effects of thermal and solutal Marangoni flows.

We can conclude that the present numerical results under the effect of radiative heat transfer exhibits more unique characteristics compared to the findings of previous studies in similar systems that used an assumption of adiabatic free surface. Results show that instabilities of thermal-solutal Marangoni flow, which is crucial for the quality of final products in applications, are greatly affected by the intensity of thermal radiation, and exhibits different characteristics in the cases of heat loss and heat gain. Such a study would be beneficial for the industrial processes such as material welding, glass production, and crystal growth, for better design and high-quality production.

6.4 Future perspectives

This thesis numerically demonstrated the instabilities on Marangoni convection in a shallow rectangular cavity with various boundary conditions. However, owing to the limited time and heavy computational workload, there are still some aspects that can be further studied.

(1) Note that, the fluid properties would have significant effects on flow characteristics, while only low Prandtl number and Schmidt number fluids are considered on the thermal-solutal Marangoni flow in the present study. In order to examine the instabilities of Marangoni flow with different working fluids in the case of thermal radiation, the effect of fluid properties needs to be considered.

(2) The convective heat transfer is also an important component of interfacial heat transfer and has a significant effect on the heat transfer in the whole system. Thus, the relative contribution of convective and radiative heat transfer would also be further investigated.

(3) The two free surfaces system is a potential way to realize a new kind of crystallization process of materials, to avoid the liquid being contaminated by impurities supplied from the solid. The characteristic on thermal-solutal Marangoni flow with two free surfaces is hoped to examined, in order to provide the theoretical foundations for perfecting the crystal growth process.

REFERENCES

[1] X Chen, X Wang, PG Chen, and Q Liu. Thermal effects of substrate on marangoni flow in droplet evaporation: response surface and sensitivity analysis. *Int. J. Heat Mass Transfer*, **113**:354–365, 2017.

[2] R Seemann, JB Fleury, and CC Maass. Self-propelled droplets. *Eur. Phys. J.: Spec. Top.*, **225**(11):2227–2240, 2016.

[3] DC Venerus and DN Simavilla. Tears of wine: New insights on an old phenomenon. *Sci. Rep.*, **5**(1):1–10, 2015.

[4] D Kang, A Nadim, and M Chugunova. Marangoni effects on a thin liquid film coating a sphere with axial or radial thermal gradients. *Phys. Fluids*, **29**(7):072106, 2017.

[5] SB Lee, S Lee, DG Kim, SH Kim, B Kang, and K Cho. Solutal-marangoni-flow-mediated growth of patterned highly crystalline organic semiconductor thin film via gap-controlled bar coating. *Adv. Funct. Mater.*, page 2100196, 2021.

[6] Z Liu, Z Li, Z Cai, Y Yang, S Chen, X Ma, H Li, Q Meng, F Zhang, Y Song, et al. Vapor-induced marangoni coating for organic functional film. *J. Mater. Chem. C*, 2021.

[7] D Camel, P Tison, and JP Garandet. Experimental study of Marangoni flows in molten and solidifying Sn and Sn-Bi layers heated from the side. *Eur. Phys. J. Appl. Phys.*, **18**(3): 201–219, 2002.

[8] YY Teng, JC Chen, CW Lu, and CY Chen. The carbon distribution in multicrystalline silicon ingots grown using the directional solidification process. *J. Cryst. Growth*, **312**(8): 1282–1290, 2010.

[9] W Guo and R Narayanan. Onset of rayleigh–marangoni convection in a cylindrical annulus heated from below. *J. Colloid Interface Sci.*, **314**(2):727–732, 2007.

[10] T Yamamoto, Y Takagi, Y Okano, and S Dost. Numerical investigation of oscillatory thermocapillary flows under zero gravity in a circular liquid film with concave free surfaces. *Phys. Fluids*, **28**(3):032106, 2016.

[11] R Liu and OA Kabov. Instabilities in a horizontal liquid layer in cocurrent gas flow with an evaporating interface. *Phys. Rev. E*, **85**(6):066305, 2012.

[12] CW Lan and JH Chian. Three-dimensional simulation of marangoni flow and interfaces in floating-zone silicon crystal growth. *J. Cryst. Growth*, **230**(1-2):172–180, 2001.

[13] MK Smith and SH Davis. Instabilities of dynamic thermocapillary liquid layers. Part 1. convective instabilities. *J. Fluid Mech.*, **132**:119–144, 1983.

[14] S Benz and D Schwabe. The three-dimensional stationary instability in dynamic thermocapillary shallow cavities. *Exp. Fluids*, **31**(4):409–416, 2001.

[15] T Yano, K Nishino, I Ueno, S Matsumoto, and Y Kamotani. Sensitivity of hydrothermal wave instability of Marangoni convection to the interfacial heat transfer in long liquid bridges of high Prandtl number fluids. *Phys. Fluids*, **29**(4):044105, 2017.

[16] RJ Riley and GP Neitzel. Instability of thermocapillary–buoyancy convection in shallow layers. Part 1. characterization of steady and oscillatory instabilities. *J. Fluid Mech.*, **359**: 143–164, 1998.

[17] Q Kang, D Wu, L Duan, JQ Zhang, B Zhou, J Wang, ZY Han, L Hu, and WR Hu. Space experimental study on wave modes under instability of thermocapillary convection in liquid bridges on tiangong-2. *Phys. Fluids*, **32**(3):034107, 2020.

[18] MK Smith. Instability mechanisms in dynamic thermocapillary liquid layers. *Phys. Fluids*, **29**(10):3182–3186, 1986.

[19] SH Davis. Thermocapillary instabilities. *Annu. Rev. Fluid Mech.*, **19**(1):403–435, 1987.

[20] CY Yan, KX Hu, and QS Chen. Thermocapillary instabilities of liquid layers on an inclined plane. *Phys. Fluids*, **30**(8):082101, 2018.

[21] W Shi and N Imaishi. Hydrothermal waves in differentially heated shallow annular pools of silicone oil. *J. Cryst. Growth*, **290**(1):280–291, 2006.

[22] YR Li, L Peng, Y Akiyama, and N Imaishi. Three-dimensional numerical simulation of thermocapillary flow of moderate prandtl number fluid in an annular pool. *J. Cryst. Growth*, **259**(4):374–387, 2003.

[23] YR Li, L Peng, SY Wu, DL Zeng, and N Imaishi. Thermocapillary convection in a differentially heated annular pool for moderate prandtl number fluid. *Int. J. Therm. Sci.*, **43**(6): 587–593, 2004.

[24] T Azami, S Nakamura, M Eguchi, and T Hibiya. The role of surface-tension-driven flow in the formation of a surface pattern on a czochralski silicon melt. *J. Cryst. Growth*, **233**(1-2): 99–107, 2001.

[25] D Schwabe. Buoyant-thermocapillary and pure thermocapillary convective instabilities in czochralski systems. *J. Cryst. Growth*, **237**:1849–1853, 2002.

[26] MA Pelacho and J Burguete. Temperature oscillations of hydrothermal waves in thermocapillary-buoyancy convection. *Phys. Rev. E*, **59**(1):835, 1999.

[27] J Burguete, N Mukolobwiez, F Daviaud, N Garnier, and A Chiffaudel. Buoyant-thermocapillary instabilities in extended liquid layers subjected to a horizontal temperature gradient. *Phys. Fluids*, **13**(10):2773–2787, 2001.

[28] I Ueno, S Tanaka, and H Kawamura. Oscillatory and chaotic thermocapillary convection in a half-zone liquid bridge. *Phys. Fluids*, **15**(2):408–416, 2003.

[29] I Ueno and T Torii. Thermocapillary-driven flow in a thin liquid film sustained in a rectangular hole with temperature gradient. *Acta Astronaut.*, **66**(7-8):1017–1021, 2010.

[30] J Xu and A Zebib. Oscillatory two-and three-dimensional thermocapillary convection. *J. Fluid Mech.*, **364**:187–209, 1998.

[31] D Schwabe, A Zebib, and BC Sim. Oscillatory thermocapillary convection in open cylindrical annuli. Part 1. experiments under microgravity. *J. Fluid Mech.*, **491**:239, 2003.

[32] BC Sim, A Zebib, and D Schwabe. Oscillatory thermocapillary convection in open cylindrical annuli. Part 2. simulations. *J. Fluid Mech.*, **491**:259, 2003.

[33] H Liu, Z Zeng, L Yin, Z Qiu, and L Qiao. Influence of aspect ratio on the onset of thermocapillary flow instability in annular pool heated from inner wall. *Int. J. Heat Mass Transfer*, **129**:746–752, 2019.

[34] L Zhang, YR Li, and CM Wu. Effect of surface heat dissipation on thermocapillary convection of low Prandtl number fluid in a shallow annular pool. *Int. J. Heat Mass Transfer*, **110**: 460–466, 2017.

[35] H Liu, Z Zeng, L Yin, Z Qiu, and L Zhang. Effect of the Prandtl number on the instabilities of the thermocapillary flow in an annular pool. *Phys. Fluids*, **31**(3):034103, 2019.

[36] L Peng, YR Li, WY Shi, and N Imaishi. Three-dimensional thermocapillary–buoyancy flow of silicone oil in a differentially heated annular pool. *Int. J. Heat Mass Transfer*, **50**(5-6): 872–880, 2007.

[37] M Iguchi and OJ Ilegbusi. *Modeling multiphase materials processes*. Springer, 2011.

[38] CM Wu, JH Chen, B Yuan, and YR Li. Bifurcations and pattern evolutions of thermosolutocapillary flow in rotating cylinder with a top disk. *Phys. Fluids*, **31**(9):094103, 2019.

[39] LM Witkowski and JS Walker. Solutocapillary instabilities in liquid bridges. *Phys. Fluids*, **14**(8):2647–2656, 2002.

[40] JC Chen, L Zhang, YR Li, and JJ Yu. Three-dimensional numerical simulation of pure solutocapillary flow in a shallow annular pool for mixture fluid with high schmidt number. *Microgravity Sci. Technol.*, **28**(1):49–57, 2016.

[41] F Doumenc, E Chénier, B Trouette, T Boeck, C Delcarte, B Guerrier, and M Rossi. Free convection in drying binary mixtures: solutal versus thermal instabilities. *Int. J. Heat Mass Transfer*, **63**:336–350, 2013.

[42] S Shiratori, D Kato, K Sugasawa, H Nagano, and K Shimano. Spatio-temporal thickness variation and transient Marangoni number in striations during spin coating. *Int. J. Heat Mass Transfer*, **154**:119678, 2020.

[43] M Curak, N Saranjam, and S Chandra. Colour variation in drying paint films. *Prog. Org. Coat.*, **136**:105173, 2019.

[44] JG Zhang, Y Okano, and S Dost. Numerical simulation of Marangoni convection in a shallow rectangular cavity with a linear solutal boundary condition. *Int. J. Heat Mass Transfer*, **178**:121578, 2021.

[45] JC Chen, CM Wu, YR Li, and JJ Yu. Effect of capillary ratio on thermal-solutal capillary-buoyancy convection in a shallow annular pool with radial temperature and concentration gradients. *Int. J. Heat Mass Transfer*, **109**:367–377, 2017.

[46] C Wu, J Chen, and Y Li. Mixed oscillation flow of binary fluid with minus one capillary ratio in the czochralski crystal growth model. *Crystals*, **10**(3):213, 2020.

[47] TL Bergman. Numerical simulation of double-diffusive Marangoni convection. *Phys. Fluids*, **29**(7):2103–2108, 1986.

[48] K Arafune and A Hirata. Thermal and solutal Marangoni convection in in–ga–sb system. *J. Cryst. Growth*, **197**(4):811–817, 1999.

[49] K Arafune and A Hirata. Interactive solutal and thermal Marangoni convection in a rectangular open boat. *Numer. Heat Transfer, Part A*, **34**(4):421–429, 1998.

[50] K Arafune, K Yamamoto, and A Hirata. Interactive thermal and solutal Marangoni convection during compound semiconductor growth in a rectangular open boat. *Int. J. Heat Mass Transfer*, **44**(13):2405–2411, 2001.

[51] Y Okano, S Umemura, Y Enomoto, Y Hayakawa, M Kumagawa, A Hirata, and S Dost. Numerical study of Marangoni convection effect on the melting of Gasb/Insb/Gasb. *J. Cryst. Growth*, **235**(1-4):135–139, 2002.

[52] Y Okano, T Suzumura, S Sakai, Y Hayakawa, M Kumagawa, A Hirata, and S Dost. Oscillatory behaviour in melting of a Gasb/Insb/Gasb system. *Mech. Res. Commun.*, **31**(5): 605–610, 2004.

[53] MA Sheremet and I Pop. Marangoni natural convection in a cubical cavity filled with a nanofluid. *J. Therm. Anal. Calorim.*, **135**(1):357–369, 2019.

[54] ZW Chen, YS Li, and JM Zhan. Double-diffusive Marangoni convection in a rectangular cavity: Onset of convection. *Phys. Fluids*, **22**(3):034106, 2010.

[55] JM Zhan, ZW Chen, YS Li, and YH Nie. Three-dimensional double-diffusive Marangoni convection in a cubic cavity with horizontal temperature and concentration gradients. *Phys. Rev. E*, **82**(6):066305, 2010.

[56] JJ Yu, CM Wu, YR Li, and JC Chen. Thermal-solutal capillary-buoyancy flow of a low Prandtl number binary mixture with a -1 capillary ratio in an annular pool. *Phys. Fluids*, **28** (8):084102, 2016.

[57] JJ Yu, YR Li, JC Chen, Y Zhang, and CM Wu. Thermal-solutal capillary-buoyancy flow of a low Prandtl number binary mixture with various capillary ratios in an annular pool. *Int. J. Heat Mass Transfer*, **113**:40–52, 2017.

[58] RL Agampodi Mendis, A Sekimoto, Y Okano, H Minakuchi, and S Dost. The relative contribution of solutal Marangoni convection to thermal Marangoni flow instabilities in a liquid bridge of smaller aspect ratios under zero gravity. *Crystals*, **11**(2):116, 2021.

[59] X Zhou and X Huai. Thermosolutocapillary convection in an open rectangular cavity with dynamic free surface. *J. Heat Transfer*, **137**(8), 2015.

[60] X Zhou and X Huai. Influence of thermal and solutal Marangoni effects on free surface deformation in an open rectangular cavity. *J. Therm. Sci.*, **26**(3):255–262, 2017.

[61] CZ Zhu and L Peng. The effect of rotation on the thermal-solutal capillary-buoyancy flow in a shallow annular pool with various capillary ratios. *Int. J. Heat Mass Transfer*, **152**: 119482, 2020.

[62] L Deng, J Chen, H Huang, Y Li, and JJ Yu. The thermo-soultal capillary-buoyancy convection at positive capillary ratio in a shallow annular pool. In *International Heat Transfer Conference Digital Library*. Begel House Inc., 2018.

[63] Y Liu, Z Zeng, L Zhang, H Liu, Y Xiao, and Y Wang. Effect of crystal rotation on the instability of thermocapillary–buoyancy convection in a czochralski model. *Phys. Fluids*, **33**(10):104101, 2021.

[64] AY Gelfgat. Numerical study of three-dimensional instabilities of Czochralski melt flow driven by buoyancy convection, thermocapillarity and rotation. *In Studies of Flow Instabilities in Bulk Crystal Growth, ed. AY Gelfgat, Transworld Research Network*, pages 57–82, 2007.

[65] PS Wei and FK Chung. Unsteady Marangoni flow in a molten pool when welding dissimilar metals. *Metall. Mater. Trans. B*, **31**(6):1387–1403, 2000.

[66] CX Zhao, C Kwakernaak, Y Pan, IM Richardson, Z Saldi, S Kenjeres, and CR Kleijn. The effect of oxygen on transitional marangoni flow in laser spot welding. *Acta Mater.*, **58**(19): 6345–6357, 2010.

[67] QZ Zhang, L Peng, F Wang, and J Liu. Thermocapillary convection with bidirectional temperature gradients in a shallow annular pool of silicon melt: Effects of ambient temperature and pool rotation. *Int. J. Heat Mass Transfer*, **101**:354–364, 2016.

[68] W Liu, PG Chen, J Ouazzani, and Q Liu. Thermocapillary flow transition in an evaporating liquid layer in a heated cylindrical cell. *Int. J. Heat Mass Transfer*, **153**:119587, 2020.

[69] T Tsukada, M Hozawa, and N Imaishi. Global analysis of heat transfer in cz crystal growth of oxide. *J. Chem. Eng. Jpn.*, **27**(1):25–31, 1994.

[70] YR Li, N Imaishi, T Azami, and T Hibiya. Three-dimensional oscillatory flow in a thin annular pool of silicon melt. *J. Cryst. Growth*, **260**(1-2):28–42, 2004.

[71] L Zhang, YR Li, CM Wu, and QS Liu. Flow pattern transition and destabilization mechanism of thermocapillary convection for low Prandtl number fluid in a deep annular pool with surface heat dissipation. *Int. J. Heat Mass Transfer*, **126**:118–127, 2018.

[72] Z Alloui, R Ouzani, and P Vasseur. Thermocapillary-buoyancy convection of a power-law fluid layer heated from below. *J. Non-Newtonian Fluid Mech.*, **282**:104332, 2020.

[73] CJ Jing, N Imaishi, S Yasuhiro, and Y Miyazawa. Three-dimensional numerical simulation of spoke pattern in oxide melt. *J. Cryst. Growth*, **200**(1-2):204–212, 1999.

[74] CJ Jing, N Imaishi, T Sato, and Y Miyazawa. Three-dimensional numerical simulation of oxide melt flow in Czochralski configuration. *J. Cryst. Growth*, **216**(1-4):372–388, 2000.

[75] NA Vinnichenko, AV Pushtaev, YY Plaksina, YK Rudenko, and AV Uvarov. Horizontal convection driven by nonuniform radiative heating in liquids with different surface behavior. *Int. J. Heat Mass Transfer*, **126**:400–410, 2018.

[76] AY Gelfgat, A Rubinov, PZ Bar-Yoseph, and A Solan. On the three-dimensional instability of thermocapillary convection in arbitrarily heated floating zones in microgravity environment. *Fluid Dyn. Mater. Process*, **1**(1):21–32, 2005.

[77] Y Kamotani, L Wang, S Hatta, A Wang, and S Yoda. Free surface heat loss effect on oscillatory thermocapillary flow in liquid bridges of high Prandtl number fluids. *Int. J. Heat Mass Transfer*, **46**(17):3211–3220, 2003.

[78] A Wang, Y Kamotani, and S Yoda. Oscillatory thermocapillary flow in liquid bridges of high Prandtl number fluid with free surface heat gain. *Int. J. Heat Mass Transfer*, **50**(21-22):4195–4205, 2007.

[79] CH Jin, Y Okano, H Minakuchi, and S Dost. Numerical simulation of thermo-solutal Marangoni convection in a full floating zone with radiative heat transfer under zero gravity. *J. Cryst. Growth*, **570**:126204, 2021.

[80] T Yano, M Hirotani, and K Nishino. Effect of interfacial heat transfer on basic flow and instability in a high-Prandtl-number thermocapillary liquid bridge. *Int. J. Heat Mass Transfer*, **125**:1121–1130, 2018.

[81] N Shitomi, T Yano, and K Nishino. Effect of radiative heat transfer on thermocapillary convection in long liquid bridges of high-Prandtl-number fluids in microgravity. *Int. J. Heat Mass Transfer*, **133**:405–415, 2019.

[82] T Yano and K Nishino. Numerical study on the effects of convective and radiative heat transfer on thermocapillary convection in a high-Prandtl-number liquid bridge in weightlessness. *Adv. Space Res.*, **66**(8):2047–2061, 2020.

[83] H Minakuchi, Y Takagi, Y Okano, K Mizoguchi, S Gima, and S Dost. A grid refinement study of half-zone configuration of the Floating Zone growth system. *J. Adv. Res. Phys.*, **3**(1):011201, 2012.

[84] CH Jin, A Sekimoto, Y Okano, H Minakuchi, and S Dost. Characterization of the thermal and solutal Marangoni flows of opposite directions developing in a cylindrical liquid bridge under zero gravity. *Phys. Fluids*, **32**(3):034104, 2020.

[85] H Minakuchi, Y Takagi, Y Okano, T Nosoko, S Gima, and S Dost. Three-dimensional numerical simulation of thermal and solutal marangoni convection in a liquid bridge under zero-gravity field. *Trans. JSASS Aerosp. Technol. Jpn.*, **10**:Ph_15–Ph_20, 2012.

[86] JF Mercier and C Normand. Influence of the Prandtl number on the location of recirculation eddies in thermocapillary flows. *Int. J. Heat Mass Transfer*, **45**(4):793–801, 2002.

[87] RL Agampodi Mendis, A Sekimoto, Y Okano, H Minakuchi, and S Dost. Global linear stability analysis of thermo-solutal Marangoni convection in a liquid bridge under zero gravity. *Microgravity Sci. Technol.*, **32**:729–735, 2020.

[88] N Imaishi, MK Ermakov, and WY Shi. Effects of Pr and pool curvature on thermocapillary flow instabilities in annular pool. *Int. J. Heat Mass Transfer*, **149**:119103, 2020.

[89] HM Li, WY Shi, and MK Ermakov. Thermocapillary flow instabilities of medium prandtl number liquid in rotating annular pools. *Int. J. Therm. Sci.*, **120**:233–243, 2017.

[90] H Liu, Z Zeng, L Yin, L Qiao, and LQ Zhang. Instability mechanisms for thermocapillary flow in an annular pool heated from inner wall. *Int. J. Heat Mass Transfer*, **127**:996–1003, 2018.

[91] CM Wu, YR Li, and RJ Liao. Rotating and thermocapillary-buoyancy-driven flow in a cylindrical enclosure with a partly free surface. *Phys. Fluids*, **26**(10):104105, 2014.

[92] CZ Zhu, L Peng, JJ Yu, and YR Li. A numerical study on the thermal capillary-buoyancy convection of a binary mixture driven by rotation and surface-tension gradient in a shallow annular pool. *Int. J. Heat Mass Transfer*, **171**:121035, 2021.

[93] JG Zhang, A Sekimoto, Y Okano, and S Dost. Numerical simulation of thermal-solutal Marangoni convection in a shallow rectangular cavity with mutually perpendicular temperature and concentration gradients. *Phys. Fluids*, **32**(10):102108, 2020.

[94] T Watanabe, Y Kowata, and I Ueno. Flow transition and hydrothermal wave instability of thermocapillary-driven flow in a free rectangular liquid film. *Int. J. Heat Mass Transfer*, **116**:635–641, 2018.

[95] L Zhang, JQ Luo, CM Wu, JJ Yu, and YR Li. Thermocapillary convection in a binary mixture with moderate Prandtl number in a shallow annular pool. *Microgravity Sci. Technol.*, **30**(1):33–42, 2018.

[96] M Stojanovic and HC Kuhlmann. Stability of thermocapillary flow in high-prandtl-number liquid bridges exposed to a coaxial gas stream. *Microgravity Sci. Technol.*, **32**(5):953–959, 2020.

[97] I Ueno, S Tanaka, and H Kawamura. Various flow patterns in thermocapillary convection in half-zone liquid bridge of high Prandtl number fluid. *Adv. in Space Res.*, **32**(2):143–148, 2003.

[98] F Wang, L Peng, QZ Zhang, and J Liu. Effect of the vertical heat transfer on the thermocapillary convection in a shallow annular pool. *Microgravity Sci. Technol.*, **27**(2):107–114, 2015.

[99] JJ Yu, CY Tang, YR Li, and T Qin. Numerical simulation study on the pure solutocapillary flow of a binary mixture with various solutal coefficients of surface tension in an annular pool. *Int. Commun. Heat Mass Transfer*, **108**:104342, 2019.

[100] Y Fukuda, T Ogasawara, S Fujimoto, T Eguchi, K Motegi, and I Ueno. Thermal-flow patterns of m= 1 in thermocapillary liquid bridges of high aspect ratio with free-surface heat transfer. *Int. J. Heat Mass Transfer*, **173**:121196, 2021.

[101] SMANR Abadi, Y Mi, F Sikström, A Ancona, and I Choquet. Effect of shaped laser beam profiles on melt flow dynamics in conduction mode welding. *Int. J. Therm. Sci.*, **166**:106957, 2021.

[102] L Zhang, YR Li, CM Wu, and L Zhang. Effect of surface heat dissipation on thermocapillary convection of moderate Prandtl number fluid in a shallow annular pool. *J. Cryst. Growth*, **514**:21–28, 2019.

[103] S Benz, P Hintz, RJ Riley, and GP Neitzel. Instability of thermocapillary–buoyancy convection in shallow layers. part 2. suppression of hydrothermal waves. *J. Fluid Mech.*, **359**: 165–180, 1998.

[104] AB Ezersky, A Garcimartin, HL Mancini, and C Perez-Garcia. Spatiotemporal structure of hydrothermal waves in marangoni convection. *Phys. Rev. E*, **48**(6):4414, 1993.

[105] H Kawamura, E Tagaya, and Y Hoshino. A consideration on the relation between the oscillatory thermocapillary flow in a liquid bridge and the hydrothermal wave in a thin liquid layer. *Int. J. Heat Mass Transfer*, **50**(7-8):1263–1268, 2007.

[106] N Mukolobwiez, A Chiffaudel, and F Daviaud. Supercritical eckhaus instability for surface-tension-driven hydrothermal waves. *Phys. Rev. Lett.*, **80**(21):4661, 1998.

LIST OF SYMBOLS

Nomenclature

$\boldsymbol{A}$ . . . . . a linear mapping matrix

$\tilde{\boldsymbol{A}}$ . . . . . similarity transformation from $\boldsymbol{A}$

A_{C} . . . . . concentration oscillation amplitude, m

A_{T} . . . . . temperature oscillation amplitude, m

C . . . . . mass fraction of solutal

D . . . . . diffusion coefficient, m^2/s

$\boldsymbol{e}$ . . . . . unit vector

F . . . . . dimensionless frequency

grad . . . . . gradient

k . . . . . thermal conductivity, W/(m·K)

L . . . . . characteristic length scale

$\boldsymbol{M}$ . . . . . a temporal sequence of data snapshots

$\boldsymbol{m}_i$ . . . . . i-th flow field

Ma . . . . . Marangoni number

Ma_σ . . . . . Marangoni ratio

N . . . . . mesh number

Nu . . . . . Nusselt number

P . . . . . dimensionless pressure

Pr . . . . . Prandtl number

Q_{r} . . . . . dimensionless heat flux

$\boldsymbol{r}$ . . . . . residual vector

R_{ad} . . . . . radiation number

Sc . . . . . Schimidt number

Sh . . . . . Sherwood number

T . . . . . temperature, K

$\boldsymbol{U}$ . . . . . right singular vector

V . . . . . dimensionless velocity

$\boldsymbol{V}$ . . . . . dimensionless velocity vector

W . . . . . temperature or concentration

$\boldsymbol{W}$ . . . . . unitary matrix

X . . . . . X coordinate, m

Y . . . . . Y coordinate, m

$\boldsymbol{y}_i$ . . . . . i-th eigenvector

Z . . . . . Z coordinate, m

Greek letters

α . . . . . thermal diffusivity, m^2/s

δ . . . . . fluctuation of temperature or concentration

ε . . . . . emissivity, m^2/s

Θ . . . . . dimensionless temperature

κ_i . . . . . dynamic modes

λ . . . . . eigenvalue

λ_i . . . . . growth/decay rate

λ_r . . . . . frequency by DMD

μ . . . . . dynamic viscosity, kg/(m·s)

μ_i . . . . . i-th eigenvalue

ν . . . . . kinematic viscosity, m^2/s

σ . . . . . surface tension, N/m

$\mathbf{\Sigma}$ . . . . . diagonal matrix

σ_{C} . . . . . solutal coefficient of surface tension, N/m

σ_{SB} . . . . . Stefan-Boltzmann constant, $W/(m^2 \cdot K^4)$

σ_{T} . . . . . temperature coefficient of surface tension, N/(m·K)

τ . . . . . dimensionless time

τ_{p} . . . . . dimensionless time of period

φ . . . . . propagation angle of wave pattern, deg

Φ . . . . . dimensionless concentration

Φ_{Mean} . . . . . dimensionless concentration of time-averaged

Superscripts

H . . . . . conjugate transpose of a matrix

N . . . . . N temporal flow fields

T . . . . . transpose of a matrix

Subscripts

a . . . . . ambient

cri . . . . . critical

C . . . . . solutal

h . . . . . high

l . . . . . low

mag . . . . . magnitude

T . . . . . thermal

x . . . . . dimensionless x coordinate

y . . . . . dimensionless y coordinate

z . . . . . dimensionless z coordinate

ACKNOWLEDGMENTS

My study at the Okano Laboratory will soon come to an end, at the completion of my graduation thesis; I wish to express my sincere appreciation to all those who have offered me invaluable help at Osaka University.

First of all, I would like to express my heartfelt gratitude to my supervisor, Prof. Yasunori Okano, who has offered me numerous valuable comments and suggestions with incomparable patience and encouraged me profoundly throughout my PhD study. Without his painstaking teaching and insightful advice, the completion of this thesis would have been impossible.

I need to acknowledge Prof. Sadik Dost at University of Victoria for his careful revision of my manuscripts, which immensely improved my academic writing skills.

I would like to express my gratitude to all colleagues and friends in Japan, Dr. Atsushi Sekimoto, Dr. Lei Wang, Dr. Radeesha Laknath Agampodi Mendis, Daniel Cardoso Cordeiro, Chihao Jin, Yuto Takehara, Taichi Yoshimura, Lukman Islam Hassan Islam, Jingyuan Dong, Haotian Hu, and other members of Okano Laboratory.

I am deeply indebted to my family and uncle. Only with their selfless support, concern, and love, can I overcome those difficulties and pursue my study till now. Many thanks to my lover, Dr. Liya Wang, who have accompanied me and shared our worries, frustrations, and happiness. Her smile and loving are the sources of my strength.

This work was partially supported by JSPS KAKENHI, Grant No. JP19K22015, supported by JST SPRING, Grant Number JPMJSP2138, and also supported by ”Joint Usage/Research Center for Interdisciplinary Large-scale Information Infrastructures” in Japan (Project ID: EX21601). The computational resources were provided by the Research Institute for Information Technology, Kyushu University, and Collaborative Research Program for Young Women Scientists provided by Academic Center for Computing and Media Studies, Kyoto University, and Initiative on Promotion of Supercomputing for Young or Women Researchers provided by Information Technology Center, Tokyo University.

LIST OF PUBLICATIONS

[Papers]

- Jiangao Zhang, Atsushi Sekimoto, Yasunori Okano, Sadik Dost; "Numerical simulation of thermal-solutal Marangoni convection in a shallow rectangular cavity with mutually perpendicular temperature and concentration gradients", Physics of Fluids, **32**, 102108 (2020).

- Jiangao Zhang, Yasunori Okano, Sadik Dost; "Numerical simulation of Marangoni convection in a shallow rectangular cavity with a linear solutal boundary condition", International Journal of Heat and Mass Transfer, **178**, 121578 (2021).

- Jiangao Zhang, Yasunori Okano, Sadik Dost; "Effect of radiative heat transfer on thermal-solutal Marangoni convection in a shallow rectangular cavity with mutually perpendicular temperature and concentration gradients", International Journal of Heat and Mass Transfer, **183**, 1221024 (2022).

[Conferences]

- Jiangao Zhang, Atsushi Sekimoto, Yasunori Okano, and Sadik Dost, "Numerical simulation of the transport phenomena occurring in the Bottom Seeded Solution Growth (BSSG) process of SiC", 18th Asian Pacific Confederation of Chemical Engineering Congress (APCChE2019), September 23-27 (2019), Sapporo, Japan.

- Jiangao Zhang, Yasunori Okano, and Sadik Dost, "Effect of ambient temperature on thermal-solutal Marangoni convection in a shallow rectangular cavity with mutually perpendicular temperature and concentration gradients", The 8th Asian Symposium on Computational Heat Transfer and Fluid Flow (ASCHT2021), September 23-26 (2021), Qingdao, China.

- Jiangao Zhang, Yasunori Okano, and Sadik Dost, "Instabilities and pattern evolutions of thermal-solutal Marangoni flow in a rectangular cavity under the effect of radiative heat

transfer", The 32nd International Symposium on Transport Phenomena (ISTP32), March 19-21 (2022), Tianjin, China.

- Jiangao Zhang, Atsushi Sekimoto, and Yasunori Okano, "Numerical simulation of thermal-solutal Marangoni convection in a shallow rectangular cavity with mutually perpendicular temperature and concentration gradients", The 32st Annual Meeting of The Japan Society of Microgravity Application (JAMSAC-32), October 4-7 (2020), Online, Japan.

- Jiangao Zhang, and Yasunori Okano, "Numerical simulation of thermal-solutal Marangoni convection in a shallow rectangular cavity with the effect of radiative heat transfer under zero gravity", The 33st Annual Meeting of The Japan Society of Microgravity Application (JAMSAC-33), October 13-15 (2021), Online, Japan.